รายงานวิจัยฉบับสมบูรณ์

โครงการ
การจำลองเชิงตัวเลขของการไหลน้ำตื้นที่มีพจน์
แรงต้านและความชันจากท้องน้ำ

โดย มนตรี มาลีวงศ์

มิถุนายน 2559

สัญญาเลขที่ RSA5680038

รายงานวิจัยฉบับสมบูรณ์

โครงการ
การจำลองเชิงตัวเลขของการไหลน้ำตื้นที่มีพจน์
แรงต้านและความชันจากท้องน้ำ

ผู้วิจัย มนตรี มาลีวงศ์

ภาควิชาคณิตศาสตร์
คณะวิทยาศาสตร์
มหาวิทยาลัยเกษตรศาสตร์

สนับสนุนโดยสำนักงานกองทุนสนับสนุนการวิจัย
และมหาวิทยาลัยเกษตรศาสตร์

Acknowledgement

This research project was supported by the Thailand Research Fund (TRF) and the Kasetsart University Research and Development Institute (KURDI) under the grant no. RSA5680038 during June 17, 2013 - June 16 2016.

Abstract

Project code: RSA5680038
Project title: Numerical simulation of shallow water flows with source terms
Investigator: Montri Maleewong, Department of Mathematics, Faculty of Science, Kasetsart University
Email address: montri.m@ku.ac.th, maleewong@gmail.com
Project period: 3 years, June 17, 2013 - June 16, 2016

Shallow water model is the set of hyperbolic partial differential equations that has very widely applications, for instance, tsunami wave propagation, flooding in both wet and dry area, open channel flow, or etc. The objectives of this research project are two folds: numerical method development, and the applications of this model to real life problem as well as in water wave theory.

To develop accurate and efficient numerical method, we study in both one and two dimensional problems. For problem in one dimension, we develop the method based on discontinuous Galerkin approach. We try to improve the consistency and accuracy of the numerical method by applying weighted average flux (WAF). Various test cases and applications have been shown in chapter 1. The results from one dimensional problem then become the solid background to extend our study in two dimensions. Details of these studies are shown in chapter 2 where we have develop an accurate and efficient finite volume method for solving the shallow water equations in two dimensions including bottom slope and frictions. The outcome is a computer program enabling us to apply the developed method to solve real life problem. We have tested our numerical scheme to solve great flood in 2011 of Chaopraya river basin, Thailand. The prediction and sattlelite image are in good agreement. This shows the accuracy and robustness of our scheme that can be applied to other problems, and we hope this would be some important basic knowledges in this research field that should save the budget to buy expensive software to do shallow water simulations in Thailand.

After we obtain the computer program of shallow water simulations, we apply the method to study in deep of shallow water flows over two obstacles. Main objective is to develop water wave theories for shock-shock interactions between the first and the second obstacle. We have found a new feature of contact discontinuities over the first obstacle, and the second obstacle always control flow criticality when the obstacle heights are equal. Full details are given in chapter 3, or published paper in 2015 of Journal of Fluid Mechanics.

The results of shallow water flows over two obstacles motivate us to study

further. One point of view is to study the same problem but different water wave model. So, we try to study by applying the force Korteweg de Vries (fKdV) model to investigate the interaction between weakly nonlinear dispersive and nonlinear terms over two obstacles. The flow is restricted only transcritical flows. Full details are given in chapter 4. It have shown the agreement and difference between the shallow water and the fKdV model. This study provides a big picture and theoretical results for connecting among water water theories.

Keywords: shallow water; open channel; flow; flood

บทคัดย่อ

รหัสโครงการ RSA5680038

ชื่อโครงการ การจำลองเชิงตัวเลขของการไหลน้ำตื้นที่มีพจน์แรงต้านและความชันจากท้องน้ำ

นักวิจัย มนตรี มาลีวงศ์ ภาควิชาคณิตศาสตร์ คณะวิทยาศาสตร์ มหาวิทยาลัยเกษตรศาสตร์
Email address: montri.m@ku.ac.th, maleewong@gmail.com

ระยะเวลาโครงการ 3 ปี 17 มิ.ย. 56 ถึง 16 มิ.ย. 59

แบบจำลองการไหลของน้ำตื้นอยู่ในรูปของสมการเชิงอนุพันธ์ย่อยแบบไฮเพอร์บอลิกซึ่งมีบทประยุกต์มากมายหลายรูปแบบ เช่น ใช้ในการศึกษาการเคลื่อนที่ของคลื่นสึนามิ การจำลองปัญหาการไหลในสภาพน้ำท่วมบนพื้นที่ที่มีน้ำและพื้นที่แห้ง หรืออาจใช้อธิบายปัญหาการไหลในช่องทางน้ำเปิดได้ เป็นต้น วัตถุประสงค์ของงานวิจัยนี้มีสองส่วนหลักๆ คือ การพัฒนาระเบียบวิธีเชิงตัวเลขของสมการการไหลน้ำตื้นและการนำแบบจำลองเชิงตัวเลขที่ได้ไปประยุกต์ใช้อธิบายปัญหาจริง รวมถึงการนำไปใช้ในการศึกษาทางด้านทฤษฎีคลื่นน้ำเพื่อหาผลเชิงวิเคราะห์ใหม่

ในการที่จะพัฒนาระเบียบวิธีเชิงตัวเลขให้มีความถูกต้องและมีประสิทธิภาพนั้น เราจะศึกษาและพัฒนากับปัญหาทั้งในหนึ่งและสองมิติ โดยที่ในปัญหาแบบหนึ่งมิติเราจะพัฒนาระเบียบวิธีที่อยู่บนพื้นฐานของวิธีกาเลอร์คินแบบไม่ต่อเนื่อง เราจะปรับปรุงความสอดคล้องและความถูกต้องโดยใช้ระเบียบวิธีค่าเฉลี่ยน้ำหนักของฟลักซ์ร่วมด้วย จากนั้นจะนำระเบียบวิธีเชิงตัวเลขที่ได้พัฒนาขึ้นไปทดสอบกับปัญหาการไหลต่างๆ รายละเอียดและผลที่ได้จากส่วนนี้จะแสดงไว้ในบทที่หนึ่ง จากนั้นเราจะขยายผลการศึกษานี้ไปยังปัญหาการไหลในสองมิติซึ่งจะรวมปัจจัยของความชัน และความเสียดทานที่ท้องน้ำไว้ด้วยซึ่งจะมีรายละเอียดแสดงไว้ในบทที่สอง ผลที่ได้จากการศึกษาในส่วนนี้จะทำให้เราได้โปรแกรมคอมพิวเตอร์สำหรับใช้ในการศึกษาปัญหาจริงได้และเราได้ทดสอบโปรแกรมที่ได้กับการจำลองปัญหาน้ำท่วมใหญ่ในลุ่มแม่น้ำเจ้าพระยาที่เกิดขึ้นในปี 2554 พบว่าผลที่ได้จากการทำนายมีความใกล้เคียงกับภาพถ่ายดาวเทียมในขณะนั้น ซึ่งสะท้อนให้เห็นถึงความถูกต้องและการนำไปใช้ได้จริงของระเบียบวิธีและโปรแกรมที่ได้พัฒนาขึ้น โดยหวังว่าผลที่ได้จากงานวิจัยนี้จะก่อให้เกิดองค์ความรู้พื้นฐานที่จำเป็นต่องานวิจัยในด้านนี้ และอาจจะช่วยลดการพึ่งพาโปรแกรมสำเร็จรูปราคาแพงที่จะใช้ในการศึกษาและจำลองการไหลน้ำตื้นในพื้นที่อื่นๆ ในประเทศไทย

หลังจากที่เราได้โปรแกรมคอมพิวเตอร์ของการจำลองการไหลน้ำตื้นแล้ว เราได้นำระเบียบวิธีที่ได้ไปใช้ศึกษาปัญหาการไหลทางทฤษฎีคลื่นน้ำ โดยได้ศึกษาปัญหาการไหลน้ำตื้นที่ผ่านสิ่งกีดขวางสองสิ่งที่ท้องน้ำ วัตถุประสงค์หลักคือเพื่อพัฒนาผลเชิงวิเคราะห์ที่ได้ในทางทฤษฎีคลื่นน้ำของการชนกันระหว่างคลื่นกระแทกที่เกิดขึ้นจากสิ่งกีดขวางแรกและสิ่งกีดขวางที่สอง ผลที่ได้คือเราทราบถึงองค์ความรู้ใหม่ของการเชื่อมต่อที่ไม่ต่อเนื่องของคำตอบบนสิ่งกีดขวางแรก และยังพบอีกว่าสิ่งกีดขวางที่สองจะเป็นตัวควบคุมการไหลในสภาพวิกฤตอยู่เสมอเมื่อความสูงของสิ่งกีดขวางทั้งสองมีค่าเท่ากัน รายละเอียดของการศึกษาในส่วนนี้จะอยู่ในบทที่สาม และผลที่ได้ได้ถูกตีพิมพ์ในวารสารวิชาการในปี 2015

ผลที่ได้จากการศึกษาปัญหาการไหลน้ำตื้นผ่านสิ่งกีดขวางสองสิ่งได้กระตุ้นให้เกิดการศึกษาต่อโดยประเด็นที่ได้ศึกษาคือ เป็นปัญหาการไหลผ่านสิ่งกีดขวางเดิม แต่เปลี่ยนแบบจำลองที่ใช้อธิบาย โดยที่เราจะใช้แบบจำลองของเอฟเคดีวีเพื่อศึกษาปฏิสัมพันธ์ระหว่างการแพร่กระจายแบบไม่เชิงเส้นอย่างอ่อนกับความไม่เชิงเส้นที่เกิดขึ้นบนสิ่งกีดขวางทั้งสอง รายละเอียดของการศึกษาในส่วนนี้ได้แสดงไว้ในบทที่สี่ ซึ่งได้แสดงผลของทั้งความสอดคล้องและความแตกต่างระหว่างผลที่ได้จากแบบจำลองการไหลน้ำตื้นและแบบจำลองของเอฟเคดีวี ผลการศึกษาทั้งสองส่วนนี้ช่วยให้เราเห็นภาพของการสร้างทฤษฎี เข้าใจพฤติกรรมการไหลและเชื่อมโยงผลที่ได้ศึกษาต่างๆ ทางด้านทฤษฎีคลื่นน้ำ ได้ดียิ่งขึ้น

คำหลัก การไหล น้ำตื้น ระเบียบวิธีเชิงตัวเลข ช่องทางน้ำเปิด

Executive Summary

Shallow water model is one of the famous model that has extensively applications, for instance, tsunami wave prediction, flooding over wet/dry area, or water flow in river. The objectives of this research project are two folds: numerical method development for solving shallow water model, and the applications of this model to real life problems as well as in water wave theory. We have developed accurate and efficient numerical methods for solving shallow water model. The outcome is a computer program that can be applied in real life problems. We have used it to simulate the great flood in Chaopraya river basin, 2011. The study area is Singburi province. Our prediction and real data in the form of sattlelite image during some periods are in good agreement. This shows the accuracy and robustness of our developed scheme. We hope that this study will be some important basic knowledges in this research field. Since, this is the core knowledge, if it is interested, the government agency would save some budgets to buy expensive computer program for simulating open channel flows in the future.

After we obtain the computer program of shallow water simulations, we apply the method to study in deep details of shallow water flows over two obstacles. Main objective is to develop water wave theories for shock-shock interactions. We can find new features and analytical results that provide a big picture and connections in the theory of water wave. All results have been published in the top world class journal, Journal of Fluid Mechanics, in 2015.

The study of shallow water flows over obstacles has motivated us to study further, but using different framework. Next, we study the same problem but under the force Korteweg de Vries (fKdV) model. We have found the agreement and the difference between the shallow water and the fKdV model. This study provides us more theoretical results for connecting results among water water theories. This work has been finished, and in process of submitting to very high standard journal.

Content

Chapter 1

Consistent Weighted Average Flux of TVD-RK discontinuous Galerkin Method

1.1 Introduction

Hyperbolic balanced law for one-dimensional problem is

$$U_t + F_x(U) = G(U), \tag{1.1}$$

where U, F, and G represent solution vector, flux function, and source terms, respectively.

In this work, the hyperbolic equation is the shallow water equations which can be expressed by

$$h_t + q_x = 0, \tag{1.2}$$

$$q_t + \left(\frac{q^2}{h} + \frac{gh^2}{2}\right)_x = -ghb_x, \tag{1.3}$$

where h is the water depth, $q = uh$ is the discharge, u is the flow velocity in the x-direction, g is the acceleration due to gravity, and b is the bottom function. Equations (1.2) and (1.3) can be rewritten by setting

$$U = \begin{pmatrix} h \\ q \end{pmatrix}, \quad F(U) = \begin{pmatrix} q \\ \frac{q^2}{h} + \frac{gh^2}{2} \end{pmatrix}, \tag{1.4}$$

and,

$$G(U) = \begin{pmatrix} 0 \\ -ghb_x \end{pmatrix}. \tag{1.5}$$

The total variation diminishing Runge-Kutta Discontinuous Galerkin (TVD-RK DG) method can be applied to solve the shallow water equations, see [3, 7, 15, 18, 25].

By the concept of discontinuous Galerkin method, numerical solutions need not to be continuous at cell interface. So, we require an efficient flux approximation. Generally, there are several types of approximations. The most famous one is the Harten-Lax-van Leer flux (HLL), while the higher order approximation is the weighted average flux (WAF), see [10, 11, 12, 17]. This approach approximates the flux functions by averaging flux in each direction along the wave solutions at the half-time step. Its origin from random flux scheme, which was shown to be second-order accuracy in space and time in statistical sense by Toro and Roe, [10]. From previous work, the weighted average flux has been successfully applied to solve various types of problems, especially in the finite volume method, [11, 13, 22]. It improves the accuracy of the finite volume method to be second order without reconstruction process.

1.2 Numerical scheme without source term

1.2.1 TVD-RK discontinuous Galerkin method

Consider the one-dimensional hyperbolic conservation law,

$$U_t + F_x(U) \;=\; 0\,. \tag{1.6}$$

The computational domain, $(0, L)$, is divided into K cells. We denote the j-th cell by $I_j = \left[x_{j-1/2}, x_{j+1/2}\right]$, for $j = 1, \ldots K$, with uniform cell size $\Delta_j = x_{j+\frac{1}{2}} - x_{j-\frac{1}{2}}$. The cell center is that $x_j = \left(x_{j+\frac{1}{2}} + x_{j-\frac{1}{2}}\right)/2$, where $x_{j+\frac{1}{2}}$ and $x_{j-\frac{1}{2}}$ are the left and the right of cell boundaries, respectively.

Approximate solution is denoted by $U_h = \begin{pmatrix} h_h \\ q_h \end{pmatrix}$.

Multiplying (1.6) by a test function, $v_h(x) \in P^N(I_j)$ where $P^N(I_j)$ is the polynomial space degree N on the interval I_j, and replacing U by U_h, then taking the integration by parts over I_j, we obtain a weak form of numerical scheme as,

$$\int_{I_j} \left(\partial_t U_h\right) v_h dx - \int_{I_j} F\left(U_h\right) \partial_x v_h dx + \hat{F}_{j+\frac{1}{2}} v_h \left(x^-_{j+\frac{1}{2}}\right) - \hat{F}_{j-\frac{1}{2}} v_h \left(x^+_{j-\frac{1}{2}}\right) = 0\,, \tag{1.7}$$

where the flux function F at the cell interfaces is approximated by $\hat{F}$, which is the function of U_h^+, and U_h^- at $x_{j\pm\frac{1}{2}}$ as,

$$\hat{F}_{j\pm\frac{1}{2}} = \hat{F}\left(\left(U_h\right)^-_{j\pm\frac{1}{2}}, \left(U_h\right)^+_{j\pm\frac{1}{2}}\right)\,. \tag{1.8}$$

Here $U_h|^-_{j\pm\frac{1}{2}}$ and $U_h|^+_{j\pm\frac{1}{2}}$ denote the approximate solutions at the left and the right of cell boundaries, respectively. If we apply the Legendre polynomials to be a local basis function, the approximate solution U_h can be written by

$$U_h\left(x,t\right) = \sum_{m=0}^{N} U_j^m\left(t\right)\varphi_m\left(x\right)\,, \tag{1.9}$$

where $U_j^m\left(t\right)$ is called the temporal coefficient. Now, the basis function $\varphi_m\left(x\right)$ is defined by the Legendre polynomial $P_m(x)$ of degree m over $[-1,1]$,

The test function $v_h\left(x\right)$ is typically chosen to be the basis function, i.e., $v_h\left(x\right) = \left\{\varphi_l\left(x\right)\right\}_{l=0}^{N}$. So, after applying the Legendre's properties, equation (1.7) is simplified to

$$\frac{dU_j^l\left(t\right)}{dt} = \frac{2l+1}{\Delta_j}\int_{I_j} F\left(U_h\right)\partial_x\varphi_l\left(x\right)dx + \frac{2l+1}{\Delta_j}\left\{\left(-1\right)^l \hat{F}_{j-\frac{1}{2}} - \hat{F}_{j+\frac{1}{2}}\right\}\,, \tag{1.10}$$

for $j = 1,\ldots,K$, and $l = 0,\ldots,N$.

The time derivative term in (1.10) can be approximated by applying the high-order TVD Runge Kutta (TVD-RK) method, see [3, 6, 15].

In this work, we apply the Monotonic Upstream-Centered Scheme for Conservation Laws (MUSCL) limiter (see [3, 10, 15, 19]) in the TVD-RK DG method.

1.2.2 Weighted average flux (WAF)

The weighted average flux, $\widehat{F}^{WAF}$ at the interface, $x_{j+1/2}$, is defined by the integral average of a flux function $F(U)$ at the half-time step,

$$\widehat{F}^{WAF}_{j+1/2} = \frac{1}{\Delta x}\int_{-\frac{\Delta x}{2}}^{\frac{\Delta x}{2}} F\left(U_{j+1/2}\left(x, \frac{\Delta t}{2}\right)\right) dx. \tag{1.11}$$

It can be written in the wave structure form as,

$$\widehat{F}^{WAF}_{j+1/2} = \sum_{k=1}^{N_c+1} \omega_k F^{(k)}_{j+\frac{1}{2}}, \tag{1.12}$$

where N_c is the number of wave solutions in the Riemann problem, and $F^{(k)}_{j+\frac{1}{2}}$ is the k^{th} flux of the Riemann problem. For one-dimensional shallow water flows, we have $N_c = 2$, where $F^{(1)}_{j+\frac{1}{2}} = F\left(U^-_{j+\frac{1}{2}}\right)$, and $F^{(3)}_{j+\frac{1}{2}} = F\left(U^+_{j+\frac{1}{2}}\right)$. Flux component $F^{(2)}_{j+\frac{1}{2}}$ can be obtained from the HLL approach, [10]. Weighted values, ω_k, are defined by $\omega_k = \frac{1}{2}\left(c_k - c_{k-1}\right)$, where $c_k = S_k\Delta t/\Delta x$ is the Courant number of wave k, $c_0 = -1$, $c_{N_c+1} = 1$, and S_k is the speed of wave k.

To avoid spurious oscillations near a shock front, the WAF method will be modified by enforcing a total variation diminishing (TVD) scheme, [9, 10, 11, 17, 22].

$$\widehat{F}^{WAF-TVD}_{j+1/2} = \frac{1}{2}\left(F\left(U^-_{j+\frac{1}{2}}\right) + F\left(U^+_{j+\frac{1}{2}}\right)\right) - \frac{1}{2}\sum_{k=1}^{N_c} \text{sgn}\left(c_k\right)\phi^{(k)}_{j+\frac{1}{2}}\Delta F^{(k)}_{j+\frac{1}{2}}, \tag{1.13}$$

where

$$\Delta F^{(k)}_{j+\frac{1}{2}} = F^{(k+1)}_{j+\frac{1}{2}} - F^{(k)}_{j+\frac{1}{2}}. \tag{1.14}$$

Here $\phi^{(k)}_{j+\frac{1}{2}}$ is a WAF limiter function. There are various choices, see more details in [9, 10, 11, 17, 22]. In this work, we choose the basic one of minmod type.

1.3 Numerical Results

In this section, various test cases have been investigated to demonstrate the accuracy of the present scheme, not only steady, but also unsteady flows.

1.3.1 Dam break flow

The accuracy of numerical solutions is shown, and compared with the standard TVD-RK DG when using the HLL method.

The computational domain is that $-5 \leq x \leq 5$. The initial water depth is given by,

$$h(x,t) = \begin{cases} 1, & \text{if } x \leq 0, \\ 0.6, & \text{if } x > 0. \end{cases} \tag{1.15}$$

The initial velocity is assumed to be zero. The boundary conditions are transmissive boundaries. We perform 50, 100, and 200 cells in the numerical experiments. Polynomial degree zero, one and two are applied as a local basis in the TVD-RK DG method. Simulation time is $t = 2$, with $\Delta t = 0.005$. The root mean squared errors (RMS) are shown in Table 1.1.

N	Numerical Flux	$K = 50$	$K = 100$	$K = 200$
$N = 0$	HLL	0.0280	0.0215	0.0165
	WAF	0.0182	0.0127	0.0094
$N = 1$	HLL	0.0130	0.0102	0.0072
	WAF	0.0107	0.0093	0.0067
$N = 2$	HLL	0.0103	0.0079	0.0053
	WAF	0.0100	0.0076	0.0052

Table 1.1: RMS errors when $N = 0$, $N = 1$ and $N = 2$.

The water depth profiles using the HLL and the WAF methods at $t = 2$ when $N = 1$, and $K = 100$ are shown in figure 1.1 and figure 1.2, respectively. The front of moving shock can be captured correctly by the HLL and the WAF methods. But, the scheme using the WAF can capture shock and rarefraction wave more precisely than those using the HLL method.

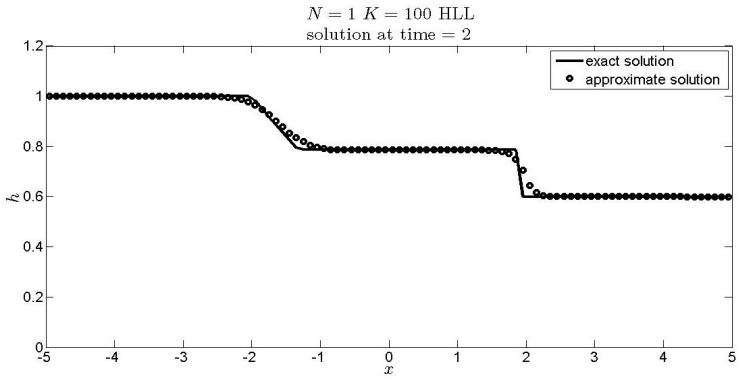

Figure 1.1: Exact solution and water depth profile obtained by the TVD-RK DG HLL method.

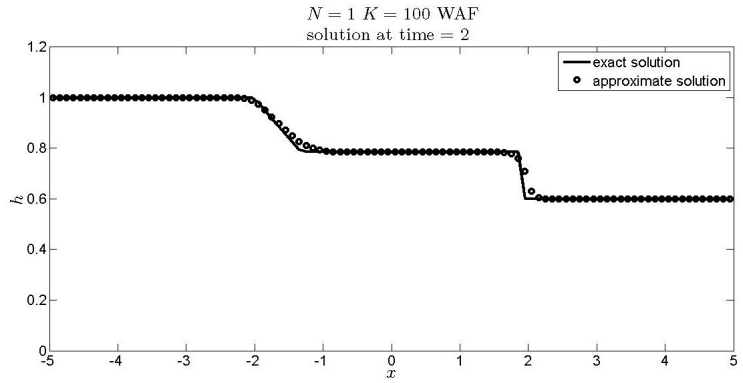

Figure 1.2: Exact solution and water depth profile obtained by the TVD-RK DG WAF method.

1.3.2 Flow over irregular bed

The uniform channel is length of 1500 m. The bottom elevation is irregular that is shown in figure 1.3. This problem is proposed by [25] for testing the accuracy of numerical scheme at stationary state. The boundary conditions are transmissive. The initial water depth is that $h + b = 16$, with zero initial velocity. We set $\Delta t = 0.01$, and run simulation until $t = 100$.

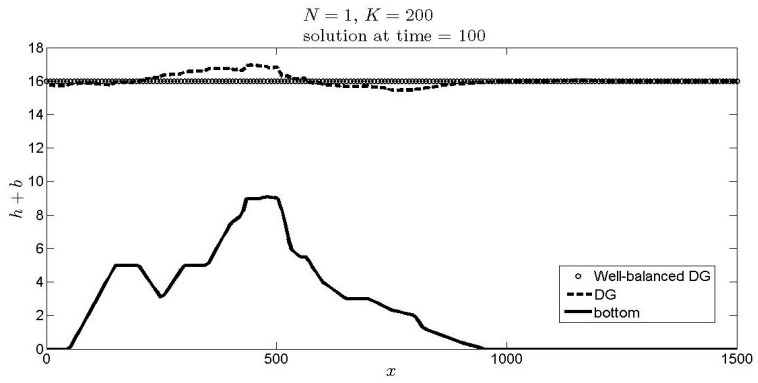

Figure 1.3: Stationary flow over irregular bed by well-balanced and non well-balanced TVD-RK DG with WAF method.

It can be seen from figure 1.3 that the well-balanced scheme (dot) gives exactly the stationary solution while the non well-balanced scheme (dash line) gives solution error especially in the high gradient area of bottom elevation.

Transcritical flow with shock over a bump

The upstream boundary is given by $q = 0.18$ m^2/s, while the downstream boundary is set by $h = 0.33$ m. The initial condition is that $h + b = 0.33$ m. The comparison of water surfaces is shown in figure 1.4. The numerical result is in good agreement with the analytical result. This shows the accuracy of the well-balanced scheme that can capture the shock front without any oscillations. It is also found that the well-balanced scheme converges to the steady solution faster than the non well-balanced scheme.

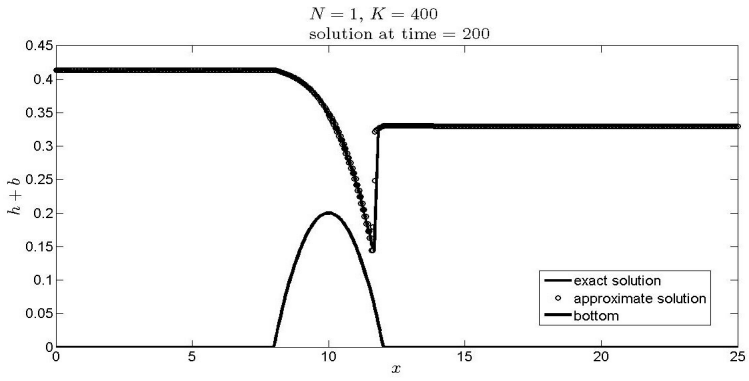

Figure 1.4: Transcritical flow with shock over a bump

Transcritical flow without shock over a bump

The upstream boundary is prescribed by $q = 1.53$ m^2/s, while the downstream boundary is not specified. The initial conditions is that $h + b = 0.4$ m with zero initial velocity.

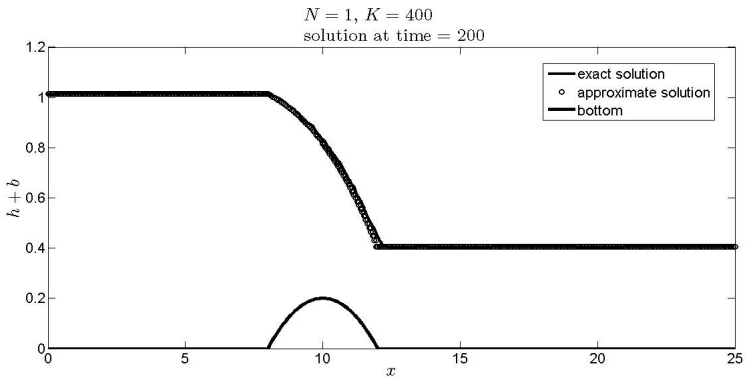

Figure 1.5: Transcritical flow without shock over a bump

The water depth profiles are shown in figure 1.5 . The numerical result agrees well with the analytical solution. These results show the accuracy of the well-balanced scheme for solving transcritical flow problem.

1.3.3 Small perturbation of steady state water

This problem is first proposed by [19, 20, 21]. It can be used to study the capability of numerical scheme for solving small perturbation in shallow water flow. The

bottom topography is defined by

$$b(x) = \begin{cases} 0.25\left(\cos\left(10\pi\left(x-1.5\right)\right)+1\right), & \text{if } 1.4 < x < 1.6, \\ 0. & \text{otherwise.} \end{cases} \tag{1.16}$$

The initial conditions are specified by

$$q(x,0) = 0\,, \quad \text{and} \quad h(x,0) = \begin{cases} 1 - b(x) + \epsilon, & \text{if } 1.1 < x < 1.2, \\ 1 - b(x), & \text{otherwise,} \end{cases} \tag{1.17}$$

where ϵ is a non-zero perturbation constant. The boundary conditions are transmissive boundaries. In this work, we consider the cases of $\epsilon = 0.2$, and 0.01. The disturbance of initial water depth from small ϵ should split the initial wave into two waves. They propagate to the left and the right with characteristic speed $\pm\sqrt{gh}$ at the early stage. A standard scheme which is not well-balanced usually faces with some difficulties to capture correctly the wave speed.

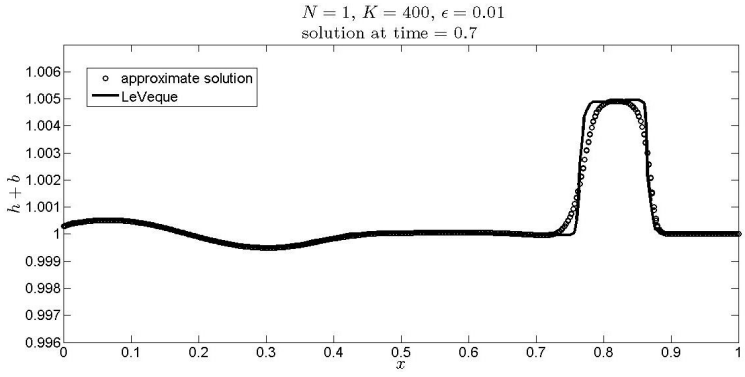

Figure 1.6: Quasi-stationary flow when $\epsilon = 0.01$

In our simulation, we use 400 uniform grid cells and polynomial degree one in the TVD-RK DG with the WAF method. The simulation time is that $t = 0.7$.

The comparison of water depths between our results and the Leveque 's solutions is shown in figures 1.6 and 1.7 for $\epsilon = 0.01$ and 0.2, respectively. They are in good agreement for both amplitude and wave speed. These test cases show the ability of our numerical scheme for solving the quasi-stationary flow with initial disturbance.

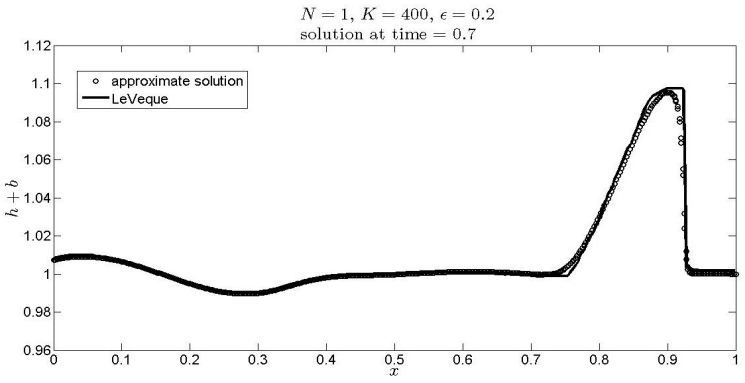

Figure 1.7: Quasi-stationary flow when $\epsilon = 0.2$

1.4 Conclusions

In this work, we present the TVD-RK discontinuous Galerkin method (TVD-RK DG) for solving nonlinear shallow water equations. Most of the TVD-RK DG methods in the literatures usually approximate intercell flux by applying the HLL method. But, here we apply another approach called the weighted average flux (WAF) in the TVD-RK DG. The present method can be used to simulate not only steady flows, but also unsteady flows. The accuray of modified numerical scheme is demonstrated by various test cases; flow over irregular bed, quasi-stationary, and flow over non-horizontal bed. The well-balanced TVD-RK DG with the WAF method can be used to solve all the kinds of these problems. Moreover, if we restrict at steady state, the scheme using the WAF method converges to the steady solution faster than the scheme using the HLL method.

Bibliography

[1] A. Bermudez and M. E. Vazquez, Upwind methods for hyperbolic conservation laws with source terms, *Comput. Fluids.* 23, 1994, pp. 1049–1071.

[2] A. Harten and H. Tal-Ezer, On a fourth order accurate implicit finite difference scheme for hyperbolic conservation laws.II five-point scheme, *J. Comput. Phys.* 41, 1981, pp. 329–356.

[3] B. Cockburn, C. W. Shu, C. Johnson and E. Tadmor, Advanced numerical approximation of nonlinear hyperbolic equations in *Lectures given at the 2nd session of the Centro Internazionale Matematico Estivo (C.I.M.E.) held in Cetraro, Italy* , June 23-28, 1997, Springer –Verlag, Telos, 1998.

[4] B. van Leer, Toward the ultimate conservation difference scheme ii., *J. Comput. Phys.* 14, 1974, pp. 361–376.

[5] B. van Leer, Toward the ultimate conservation difference scheme v., *J. Comput. Phys.* 32, 1979, pp. 1–136.

[6] C. W. Shu, TVD time discretizations, *SIAM J. Sci. Stat. Comput.* 9, 1988, pp. 1073–1084.

[7] D. Schwanenberg, R. Kiem, and J. Kongeter, A discontinuous Galerkin method for the shallow-water equations with source terms. Discontinuous Galerkin Methods: Theory, Computations and Applications, B. Cockburn, G. E. Karniadaki, and C.-W. Chu, Eds. in *Lecture Notes in Computational Science and Engineering*, Springer, 2000, pp. 1419–424.

[8] E. Audusse, F. Bouchut, M. O. Bristeau, R. Klein and B. Perthame, A fast and stable well-balanced scheme with hydrostatic reconstruction for shallow water flows, *SIAM J. Sci. Comput.* 25, 2004, pp. 2050–2065.

[9] E.D. FernÃąndez-Nieto and G. Narbona-Reina, Extension of WAF Type Methods to Non-Homogeneous ShallowWater Equations with Pollutant, *J. Sci. Comput.* 36, 2008, pp. 193–127.

[10] E. F. Toro, *Riemann Solvers and Numerical Methods for Fluid Dynamics: A Practical Introduction*, Springer, 1999.

[11] E. F. Toro, *Shock-Capturing Methods for Free-Surface Shallow Flows*, John Willy and sons LTD, 2001.

[12] E. F. Toro, Riemann problems and the WAF method for solving the two-dimensional shallow water equations, *J. Philos. Trans. R. Soc. London Ser.* 338, 1992, pp. 43–68.

[13] E. F. Toro and P. L. Roe, A hybridised high-order random choice method for quasi-linear hyperbolic systems, in *Proc. 16th Intern Symp. on Shock Tubes and Waves, Aachen, Germany, July 1987*, edited by Gronig, p. 701.

[14] G. Kesserwani and Q. Liang, Well-balanced RKDG2 solutions to the shallow water equations over irregular domains with wetting and drying, *J. Comput. Fluids.* 39, 2010, pp. 2040–2050.

[15] J. S. Hesthaven and T. Warburton, *Nodal Discontinuous Galerkin Methods: Algorithms, Analysis, and Applications*, Springer, 2008.

[16] O. Delestre, C. Lucas, P-A. Ksinant, F. Darboux, C. Laguerre, T.-N.-Tuoi Vo, F. James and S. Cordier, SWASHES: a compilation of shallow water analytic solutions for hydraulic and environmental studies, *Int. J. Numer. Meth. Fluids.* 2012, pp. 346–365.

[17] M. Maleewong, Modified predictor-corrector WAF method for the shallow water equations with source terms, *Math. Prob. Eng.* 2011

[18] P. A. Tassi and C.-A. Vionnet, Discontinuous Galerkin method for the one dimensional simulation of shallow water flows, *Mecànica Computational Vol. XXII, Bahía Blanca*, 22, 2003, pp. 2403–2428.

[19] R. J. Leveque, *Finite Volume Method for Hyperbolic Problem* Cambridge University Press, 2005.

[20] R. J. Leveque, *Numerical Methods for Conservation Laws*, Birkhäuser Verlag Press, 1992.

[21] R. J. Leveque, Balancing source terms and flux gradients in high-resolution Godunov methods: The quasi-steady wave-propagation algorithm, *J. Comput. Phys.* 146, 1998, pp. 346–365.

[22] S. J. Billett and E. F. Toro, On WAF-Type Schemes for Multidimensional Hyperbolic Conservation Laws, *J. COMPUT. PHYS.* 130, 1997, pp. 1–24.

[23] S. Noelle, N. Pankratz, G. Puppo and J. R. Natvig, Well-balanced finite volume schemes of arbitrary order of accuracy for shallow water flows, *J. Comput. Phys.* 213, 2006, pp. 474–499.

[24] T. Pongsanguansin, K. Mekchay and M. Maleewong, Adaptive TVD-RK discontinuous Galerkin algorithms for shallow water equations, *J. Math Compute. Simulat.* 2, 6, 2012, pp. 257–273.

[25] W. Lai and A. A. Bouchut, Discontinuous Galerkin method for 1D shallow water flow with water surface slope Limiter, *Int. J. Civil and Env. Eng.* 3, 2011, pp. 167–176.

[26] Y. Xing and C. W. Shu, High order well-balanced finite volume WENO schemes and discontinuous Galerkin methods for a class of hyperbolic systems with source terms, *J. Comput. Phys.* 214, 2006, pp. 567–598.

Chapter 2

Two-dimentional shallow-water simulations by a well-balanced WAF finite volume method

2.1 Introduction

To simulate shallow water flows and flooding, finite volume methods have been developed extensively in the last two decades, see details and reviews in [19, 20]. There are various numerical fluxes used to approximate flux at cell interface in the shallow water equations. One extensively used scheme is Harten-Lax-van Leer (HLL), see details in [5, 6, 16]. The modified version of this scheme for two-dimensional problems is HLLC, [18]. To obtain a more accurate approximation, the weighted average flux (WAF) has been introduced, see [6, 7, 8, 14, 18, 21, 24]. It is second-order accurate in both space and time, see [5]. The WAF approximation is widely applied in the finite volume method. It can solve various types of problems, see for instance, [4, 7, 14, 18, 24].

In this work, we study the finite volume method with WAF approximation. The motivation for using WAF is its greater accuracy than the HLLC flux and some other numerical flux as shown in [18].To obtain accurate results at steady state, we have modified the WAF approximation with well-balancing property which was first introduced by Audess [3]. Recently, a similar scheme for unstructured mesh was proposed by Ata et al. [18]. To ensure second-order accuracy in time integration, we apply the second-order Runge-Kutta (RK2) method. For real applications, that usually deal with strong friction, the splitting implicit method

proposed by Kesserwani and Liang in [9, 10] is also applied during the time integration in our proposed scheme. By combining all of these techniques, the present scheme is accurate and efficient as it will be shown by our numerical experiments.

In order to check the accuracy and efficiency of the present scheme, numerical experiments are performed using benchmark problems with previously known results from literature. For real application usages, the present scheme is applied to simulate the great flood occurring in Thailand during October 13-17, 2011, in Chao Phraya river basin from Chai Nat to Sing Buri provinces. The result is compared to the satellite images obtained from [26, 27, 28].

2.2 Numerical method for shallow water equations

2.2.1 Finite volume method

The two-dimensional shallow water equations are expressed by

$$h_t + (hu)_x + (hv)_y = 0, \tag{2.1}$$

$$(hu)_t + \left(hu^2 + \frac{1}{2}gh^2\right)_x + (huv)_y = -ghz_x + ghS_{fx}, \tag{2.2}$$

$$(hv)_t + (huv)_x + \left(hv^2 + \frac{1}{2}gh^2\right)_y = -ghz_y + ghS_{fy}, \tag{2.3}$$

where h is the water depth, u and v are the flow velocities in the x and y directions, respectively, g is the acceleration due to gravity, and z is the bottom elevation. $S_{fx} = -Cu\sqrt{u^2+v^2}$, and $S_{fy} = -Cv\sqrt{u^2+v^2}$ are the friction terms in the in x and y directions, respectively, where $C = gn^2/h^{1/3}$ with n denoting the Manning's Roughness coefficient.

The conservative form of equations (2.1)-(2.3) is

$$U_t + F(U)_x + G(U)_y = S(U), \tag{2.4}$$

where $U = (h, hu, hv)^T$, $F = \left(hu, hu^2 + \frac{1}{2}gh^2, huv\right)^T$, $G = \left(hv, huv, hv^2 + \frac{1}{2}gh^2\right)^T$, and $S = S_b + S_f = (0, -ghz_x, -ghz_y)^T + (0, ghS_{fx}, ghS_{fy})^T$.

A discretized form of (2.4) is

$$\frac{dU_{ij}(t)}{dt} + \frac{\widehat{F}_{i+1/2,j} - \widehat{F}_{i-1/2,j}}{\Delta x} + \frac{\widehat{G}_{i,j+1/2} - \widehat{G}_{i,j-1/2}}{\Delta y} = S_{ij}, \tag{2.5}$$

where U_{ij} is the approximation of U, defined as the the unknown average over cell $I_{ij} = \left(x_{i-1/2}, x_{i+1/2}\right) \times \left(y_{j-1/2}, y_{j+1/2}\right)$, namely,

$$U_{ij} = \frac{1}{\Delta x \Delta y} \int_{I_{ij}} U\left(x, y\right) dxdy, \tag{2.6}$$

with $\Delta x = x_{i+1/2} - x_{i-1/2}$ and $\Delta y = y_{j+1/2} - y_{j-1/2}$. Here, S_{ij} is the approximation of the source term at cell I_{ij}, and $\widehat{F}$ and $\widehat{G}$ are numerical fluxes in the x and y directions, respectively.

To ensure second-order accuracy in time, the second-order Runge-Kutta (RK2) method is applied in our work. It is found in our simulations that this method allows us to use time step sizes larger than if using the first-order method.

2.2.2 Weighted average flux (WAF)

Let's first consider the approximation of numerical flux in the x direction. The intercell flux with WAF at interface $(x_{i+1/2}, y_j)$ is denoted by $\widehat{F}^{WAF}_{i+1/2,j}$, which is defined as an integral average of $F(U)$ at the half-time step, namely,

$$\widehat{F}^{WAF}_{i+1/2,j} = \frac{1}{\Delta x} \int_0^{\Delta y} \int_{-\frac{\Delta x}{2}}^{\frac{\Delta x}{2}} F\left(U_{i+1/2,j}\left(x, y, \frac{\Delta t}{2}\right)\right) dxdy. \tag{2.7}$$

The details of derivations of WAF can be found in [5, 6, 8]. Moreover, the wave structure form of WAF can be written as

$$\widehat{F}^{WAF}_{i+1/2,j} = \sum_{k=1}^{N_c+1} \omega_k F^{(k)}_{i+\frac{1}{2},j}, \tag{2.8}$$

where N_c is the wave number and $F^{(k)}_{i+\frac{1}{2},j}$ is the value of flux in the region k of the solution of the Riemann problem.

The weighted average flux with Harten-Lax-van Leer-Contact (HLLC) version in two dimensions is proposed by [18, 24]. There are three flux components where the first two components are estimated by the weighted average values from the HLLC Riemann solver as,

$$\left(\widehat{F}^{WAF}_{i+1/2,j}\right)_p = \sum_{k=1}^{3} \omega_k \left(F^{(k)}_{i+\frac{1}{2},j}\right)_p, \quad (p = 1, 2), \tag{2.9}$$

while the third component is the weighted average value of WAF as,

$$\left(\widehat{F}^{WAF}_{i+1/2,j}\right)_3 = \left(\omega_{1_*} v^-_{i+1/2,j} + \omega_{2_*} v^+_{i+1/2,j}\right)\left(\widehat{F}^{WAF}_{i+1/2,j}\right)_1, \tag{2.10}$$

where $\left(F^{(1)}_{i+\frac{1}{2},j}\right)_p = \left(F\left(U^-_{i+\frac{1}{2},j}\right)\right)_p$, $\left(F^{(3)}_{i+\frac{1}{2},j}\right)_p = \left(F\left(U^+_{i+\frac{1}{2},j}\right)\right)_p$, and $U^-_{i+\frac{1}{2},j}$ and $U^+_{i+\frac{1}{2},j}$ are the solutions from the left and the right limits at the interface $i+\frac{1}{2}$. The flux in intermediate region $\left(F^{(2)}_{i+\frac{1}{2},j}\right)_p$ is approximated by the Harten-Lax-Van Leer (HLL) approach as [24]. The weighted values are $\omega_1 = \frac{1}{2}(1+c_1)$, $\omega_2 = \frac{1}{2}(c_2 - c_1)$, $\omega_3 = \frac{1}{2}(1-c_2)$, $\omega_{1_*} = \frac{1}{2}(1+c^*)$, and $\omega_{2_*} = \frac{1}{2}(1-c^*)$, where $c_1 = S_L \Delta t/\Delta x$, $c_2 = S_R \Delta t/\Delta x$, and $c^* = S^* \Delta t/\Delta x$. Here S_L, S_R, and S^* are wave speeds in the left, the right, and the intermediate regions, respectively.

To avoid spurious oscillations near a shock front, the WAF method is modified by enforcing the total variation diminishing (TVD) conditions [5, 6], which can be written as

$$\left(\widehat{F}^{WAF-TVD}_{i+1/2,j}\right)_p = \sum_{k=1}^{N_c+1} \bar{\omega}_k \left(F^{(k)}_{i+\frac{1}{2},j}\right)_p, \quad (p=1,2), \tag{2.11}$$

and

$$\left(\widehat{F}^{WAF-TVD}_{i+1/2,j}\right)_3 = \left(\bar{\omega}_{1_*} v^-_{i+1/2,j} + \bar{\omega}_{2_*} v^+_{i+1/2,j}\right)\left(\widehat{F}^{WAF-TVD}_{i+1/2,j}\right)_1, \tag{2.12}$$

where the new weights are

$\bar{\omega}_1 = \frac{1}{2}\left(1 + \text{sgn}\left(c_1\right)\phi^{(1)}_{i+\frac{1}{2},j}\right)$, $\bar{\omega}_2 = \frac{1}{2}\left(\text{sgn}\left(c_2\right)\phi^{(2)}_{i+\frac{1}{2},j} - \text{sgn}\left(c_1\right)\phi^{(1)}_{i+\frac{1}{2},j}\right)$,
$\bar{\omega}_3 = \frac{1}{2}\left(1 - \text{sgn}\left(c_2\right)\phi^{(2)}_{i+\frac{1}{2},j}\right)$, $\bar{\omega}_{1_*} = \frac{1}{2}\left(1 + \text{sgn}\left(c^*\right)\phi^{(*)}_{i+\frac{1}{2},j}\right)$, and
$\bar{\omega}_{2_*} = \frac{1}{2}\left(1 - \text{sgn}\left(c^*\right)\phi^{(*)}_{i+\frac{1}{2},j}\right)$.
Here $\phi^{(l)}_{i+\frac{1}{2},j}$ are the WAF limiters, where the minmod function is employed in this work, namely,

$$\phi^{(l)}_{i+\frac{1}{2},j} = \begin{cases} 1, & r^{(l)} \le 0, \\ 1 - (1 - |c_l|)\, r^{(l)}, & 0 \le r^{(l)} \le 1, \\ |c_l|, & r^{(l)} \ge 1, \end{cases} \tag{2.13}$$

where $r^{(l)}$ is defined by

$$r^{(l)} = \begin{cases} \dfrac{\Delta h^{(l)}_{i-\frac{1}{2},j}}{\Delta h^{(l)}_{i+\frac{1}{2},j}}, & \text{if } c_l \geq 0, \\ \dfrac{\Delta h^{(l)}_{i+\frac{3}{2},j}}{\Delta h^{(l)}_{i+\frac{1}{2},j}}, & \text{if } c_l < 0\,, \end{cases} \tag{2.14}$$

with $\Delta h^{(l)}_{i-\frac{1}{2},j}$, $\Delta h^{(l)}_{i+\frac{1}{2},j}$, and $\Delta h^{(l)}_{i+\frac{3}{2},j}$ being the jumps of h across the wave l in the solutions $U_{i-\frac{1}{2},j}$, $U_{i+\frac{1}{2},j}$, and $U_{i+\frac{3}{2},j}$ of the Riemann problem, respectively. Similarly, the numerical flux in the y direction, $\hat{G}_{i,j+1/2}$, is obtained via equations (2.11)-(2.12).

2.2.3 Linear reconstruction

Since approximating the solution by the cell average only gives first-order accuracy, second-order accuracy can be obtained by linear reconstruction. For example, in the x-direction, the unknown variables are reconstructed as

$$U^{+}_{i-1/2,j} = U_{ij} - \sigma_{ij}\Delta x, \tag{2.15}$$

$$U^{-}_{i+1/2,j} = U_{ij} + \sigma_{ij}\Delta x, \tag{2.16}$$

where σ_{ij} is a slope limiter. In this work, we applied the minmod slope limiter,

$$\sigma_{ij} = \text{minmod}\left(\frac{U_{i-1,j} - U_{i,j}}{\Delta x}, \frac{U_{i,j} - U_{i+1,j}}{\Delta x}\right), \tag{2.17}$$

where

$$\text{minmod}\,(a,b) = \begin{cases} a, & \text{if } |a| \leq |b| \text{ and } ab > 0, \\ b, & \text{if } |b| \leq |a| \text{ and } ab > 0, \\ 0, & \text{if } ab \leq 0\,. \end{cases} \tag{2.18}$$

Similarly, the linear reconstruction in the y-direction can be obtained as in equations (2.15)-(2.16).

2.3 Friction term approximations

To obtain a stable finite volume method when dealing with a strong nonlinear friction term, we use an implicit scheme to approximate the friction. Following the splitting implicit technique presented in [9, 10], we solve the shallow water system by considering the ordinary differential equation

$$\frac{dU_{ij}}{dt} = (S_f)_{ij}^{n+1}. \tag{2.19}$$

In the x-direction, we have

$$\frac{d\,(hu)_{ij}}{dt} = (S_f)_{ij}^{n+1}, \tag{2.20}$$

written in semi-implicit form as

$$(hu)_{ij}^{n+1} = (hu)_{ij}^{n} + \Delta t \frac{(S_{fx})_{ij}^{n}}{(D_x)_{ij}^{n}}, \tag{2.21}$$

where

$$(D_x)_{ij}^{n} = 1 + \Delta t C_{ij}^{n} \frac{\left((hu)_{ij}^{n}\right)^2 + \left((hv)_{ij}^{n}\right)^2}{\left(h_{ij}^{n}\right)^2 \sqrt{\left((hu)_{ij}^{n}\right)^2 + \left((hv)_{ij}^{n}\right)^2}}. \tag{2.22}$$

The updated solutions are calculated twice for each step of the Runge-Kutta method. These calculations are also similar when considered in the y direction. Since the well-balanced scheme that we apply here has preserved the non-negativity of water depth, see [3], it implies that our numerical scheme with this friction term approximation also preserves the non-negativity of water depth. The reason is that this technique preserves automatically the non-negativity of water depth when the RHS in the conservation of mass equation is zero.

2.4 Numerical results

In this section, we describe numerical experiments for various test cases used to check the accuracy of our scheme. For practical purposes, the developed numerical scheme is applied to simulate the great flood in Thailand 2011.

2.4.1 Partial dam-break

This experiment is considered on a 200 m$\times$ 200 m rectangular domain. The initial water level is set at 10 m on the upstream side and zero on the downstream side. The bottom is assumed to be flat and frictionless. The partial dam-break is set at middle of the domain, as shown in Figure 2.1.

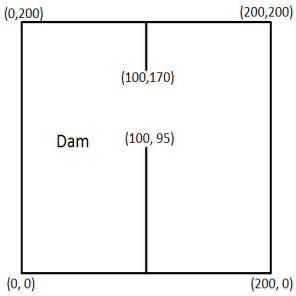

Figure 2.1: Domain of the partial dam break problem.

The simulation is performed on 85×85 uniform grid cells and with final time 7.2. The surface profile and its contour plot at $t = 7.2s$ are shown in Figure 2.2. The obtained simulation results agree closely with results in [11, 13].

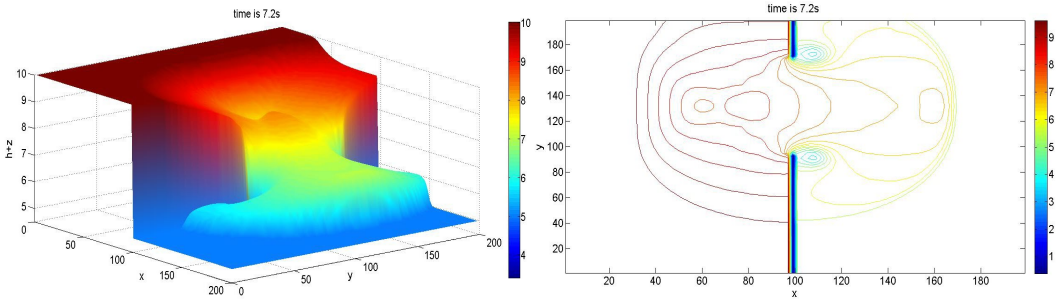

Figure 2.2: Water surface plot (left) and contour plot (right) of the partial dam-break problem.

2.4.2 Well-balanced test in two dimensions

This experiment is performed to check the exact C-property of the present scheme. To satisfy the exact C-property, the numerical solution should approach the still

water stationary solution at steady state, [22], i.e., having zero errors. In this experiment we consider a rectangular domain $[0,1] \times [0,1]$ with the bottom function defined by

$$z(x,y) = 0.8e^{-50\left((x-0.5)^2+(y-0.5)^2\right)}. \tag{2.23}$$

The initial water height is $h(x,y) = 1 - z(x,y)$ with zero initial discharges, $hu(x,y) = 0$ and $hv(x,y) = 0$.

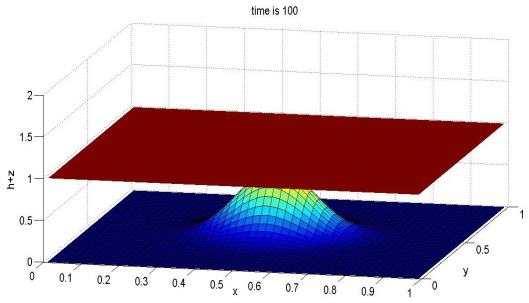

Figure 2.3: Water surface profile for very large time.

The simulation is run on 50×50 uniform cells for very large final time, in this case we use $t = 100s$. The RMS errors for h, hu, and hv are 2.0974×10^{-16}, 7.7270×10^{-14}, and 8.5070×10^{-14}, respectively. The observed errors are approximately the round-off errors of the machine, which implies that the obtained numerical solution is exact. This shows that the developed scheme satisfies the exact C-property. Figure 2.3 shows the water profile of the still water at $t = 100s$.

2.4.3 Dam-break flows over three humps

In this experiment we consider the dam-break flows over three humps defined by

$$\begin{aligned} z(x,y) = \quad & \max\Big\{0, 1 - \tfrac{1}{8}\sqrt{(x-30)^2 + (y-6)^2}, \\ & 1 - \tfrac{1}{8}\sqrt{(x-30)^2 + (y-24)^2}, \\ & 3 - \tfrac{3}{10}\sqrt{(x-47.5)^2 + (y-15)^2}\Big\}, \end{aligned} \tag{2.24}$$

on 75 m x 30 m rectangular domain. The dam is located at 16 m from the upstream boundary with initial water depth $h + z$ = 1.875 m and with zero depth on

downstream boundary. The simulation is performed on 85×85 uniform grid cells with the Manning coefficient 0.018. The water depth profile and its contour plot at $t = 12s$ are shown in Figure 2.4. The obtained result agree closely with the previous results presented by [10, 17]. This experiment has illustrated the ability of the developed scheme for solving flows over dry bed with friction. As shown in the Figure 2.4, the strong shock front that attacks the largest hump is detected correctly. This demonstrates that the developed scheme is capable of simulating flows that have both wet and dry beds, as well as the effect from a large bottom slope. We have also found that the splitting implicit scheme enables us to use larger time step size when comparing with direct calculation.

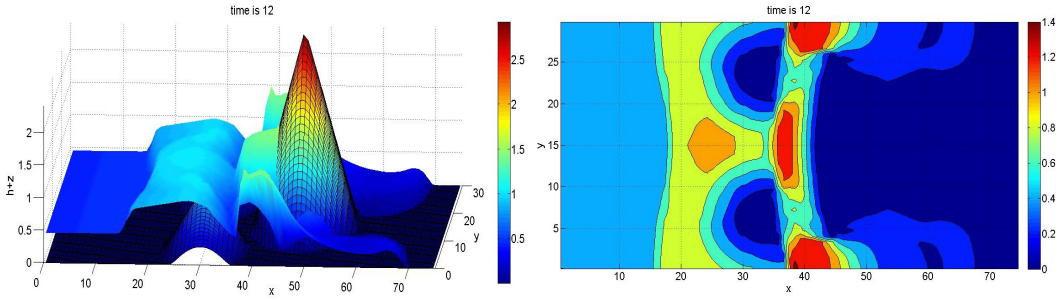

Figure 2.4: The water surface profile (left) and contour plot (right) of a dam-break flows over three humps at t = 12s.

When simulating wet/dry flow interactions, numerical schemes can result in non-conserved water mass. We have checked this by setting an initial mass in our simulation as 893.3824. After running to 100 simulation time, the water mass is remains as 893.3824. This demonstration is numerical evidence that our scheme can preserve mass during time integration. The result is shown in Figure 2.5.

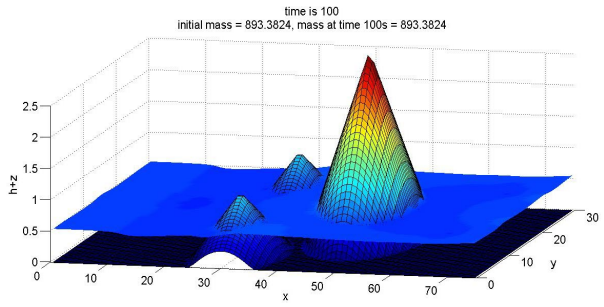

Figure 2.5: Water surface profile of a dam-break flows over three humps at t = $100s$.

2.4.4 Flood simulation in Thailand, 2011.

Chao Phraya river basin consist of Ping basin, Wang basin, Yom basin, Nan basin, Sakae Krang Basin, Pa Sak Basin, Tha Chin Basin and finally the Chao Phraya Basin itself. This basin is the most important one. The major cities are located along the river and are a large source of community and economic hub of the country. In this experiment, we check the performance of the developed numerical scheme by simulating a real flood flow, the great flood flow near the Chao Phraya river basin in Thailand, 2011. The great flood in 2011 is caused by many factor such as the rain that fall than the usual, the volume of water accumulated from January to October, the restrictions on drainage etc. The studied area is from the latitude $15.000000°$N to $15.190800°$N, and from the longitude $100.165800°$E to $100.340800°$E , known as the Chao Phraya river basin, from Chai Nat to Sing Buri provinces (see Figure 2.6), with the gauging stations located at c13 in Chai Nat province and c44 in Sing Buri province. The topography in this area is generally low land next to the Chao Phraya river. The bottom elevation is obtained from the SRTM in DEM format with resolution 90×90 m, [28], while the Manning coefficient is assumed to be 0.03. In this simulation we have adjusted DEM in the Chao Phraya river to be lower approximately 10 meters from the original SRTM format, [28]. This error can be measured from the measurement of water depth at c13 and c44 stations, [27] while the DEM on the land area remains unchanged.

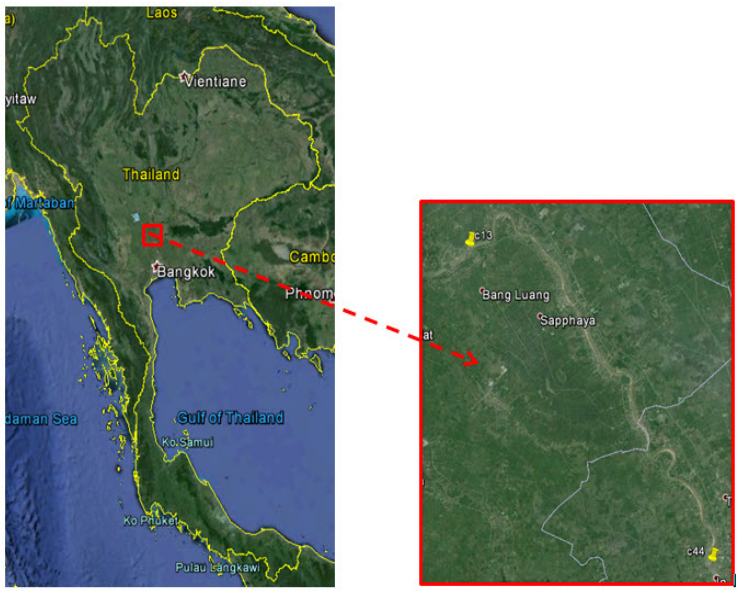

Figure 2.6: The studied area, the Chao Phraya river at Chai Nat to Sing Buri province, Thailand.

The initial water depth is set to be dry for the whole domain. Water is released from a source along the river where the water depth and its discharge are set to be the same values as the data obtained from the c13 station on October 13-17, 2011, [27]. Details are shown in table (see Table 2.1). Then we consider five days simulation on October 13-17. We compare the discrepancy on the last day where the water distribution from the sattlelite image on October 17 is shown in Figure 2.7(a). The simulation result on the same day is shown in Figure 2.7(b). The difference between real and simulation results on the lower part of the river is shown in Figure 2.7(c). The comparison is only made on the left of the river as specified by the pink-shaded area of Figure 2.7(c). The flood simulation in this case is due to the massive source of water from the river that flows over to the lower land area. The agreement between real and simulation results is shown. It should be noted that the flooded area on the right or on the top of the river appears. This situation is from the other sources of water over the land that are not included initially in our simulations. So, we can see the flooded area only on the lower part of the river.

We have also imposed an additional source of water along the top boundary based on the water depth over the river at c13 station exceeding the maximum

water capacity by approximately 1 meter. The comparisons are shown in Figure 2.8. The difference is shown in the pink-shaded area. It is found that numerical solutions agree well with the real data.

	13 Oct 2011	14 Oct 2011	15 Oct 2011	16 Oct 2011	17 Oct 2011
water height (m)	17.59	17.57	17.56	17.55	17.55
discharge (m^3/s)	3534.2	3522.6	3516.8	3511	3511

Table 2.1: The measurement data of water heights and discharges at c13 station on October 13-17, 2011.

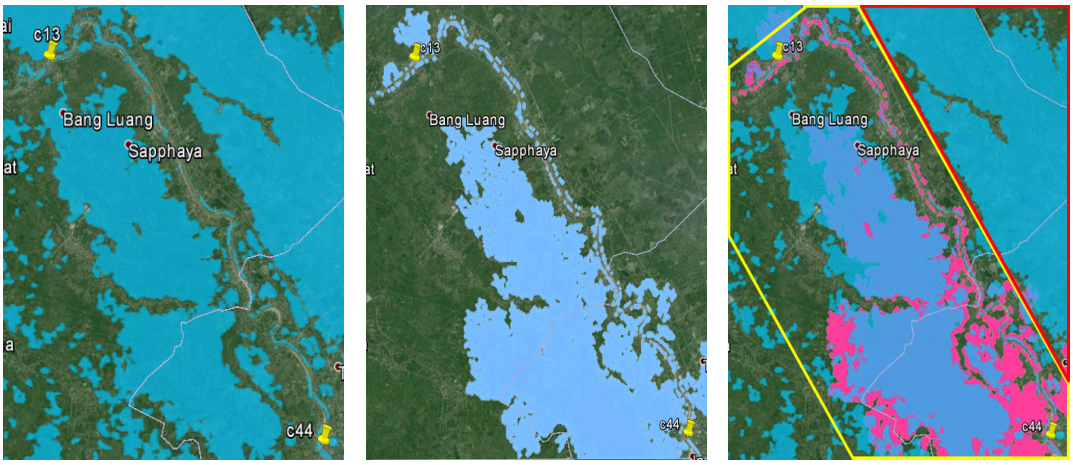

(a) The real data from satellite image on October 17, 2011.

(b) The simulation results on October 17, 2011. Initially assumed dry for the whole domain.

(c) The difference (pinkshed area) between the real data and the simulation result on October 17, 2011. The comparison is only made on the lower part of the river (inside yellow box).

Figure 2.7: The results on October 17, 2011 for the case of initially dry on the whole domain.

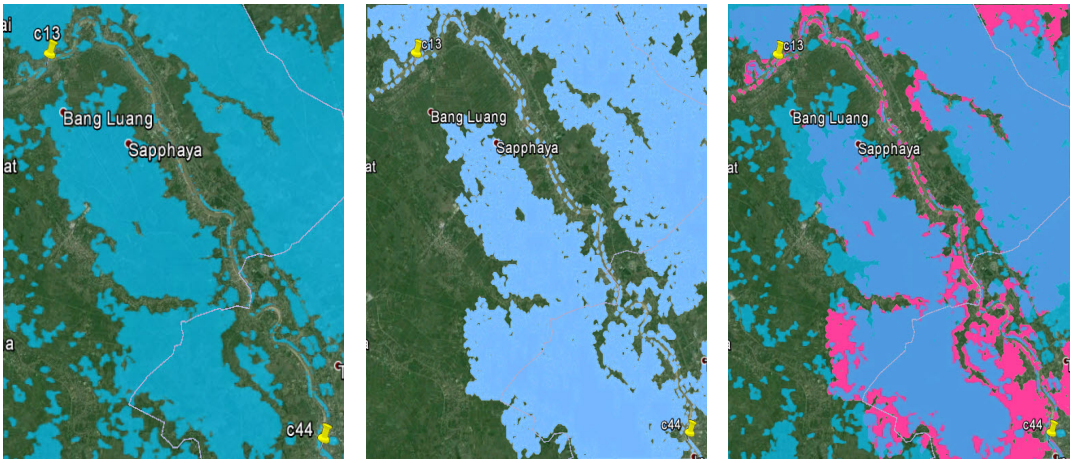

(a) The real data from satellite image on October 17.

(b) The simulation result on October 17, initially assumed dry for the whole domain, and specify source of water along the top boundary

(c) The difference (pinkshed area) between real data from the satellite image and the simulation result

Figure 2.8: The results on October 17, 2011 for the case of initially dry on the whole domain and specify water flow on the top boundary.

2.5 Conclusions

A well-balanced finite volume method with the weighted average flux (WAF) is developed in this work to simulate water flows such as dam-break and flood. Combining with semi-implicit scheme for estimating friction source terms yields an efficient numerical method for simulating shallow water flows for both wet and dry beds. The accuracy of our numerical scheme is investigated by various numerical experiments including one and two dimensional problems. Moreover, the validity and accuracy of the scheme is illustrated in the experiments by comparison to other results in literature. For real applications, the developed scheme is applied to simulate the great flood which occurred in Thailand, 2011. The numerical simulations show results that agree with the existing data obtained from satellite images. All of these experiments have demonstrated that the presented scheme is capable of accurate and efficient simulation of various kinds of shallow-water problems.

Bibliography

[1] A. Bermudez and M. E. Vazquez, Upwind methods for hyperbolic conservation laws with source terms, *Comput. Fluids.* 23, 1994, pp. 1049–1071.

[2] B. F. Sanders, Integration of a shallow water model with a local time step, *J. Hydraul. Res.* 46, 4, 2008, pp. 466–475.

[3] E. Audusse, F. Bouchut, M. O. Bristeau, R. Klein and B. Perthame, A fast and stable well-balanced scheme with hydrostatic reconstruction for shallow water flows, *SIAM J. Sci. Comput.* 25, 2004, pp. 2050–2065.

[4] E.D. FernÃąndez-Nieto and G. Narbona-Reina, Extension of WAF Type Methods to Non-Homogeneous ShallowWater Equations with Pollutant, *J. Sci. Comput.* 36, 2008, pp. 193–127.

[5] E. F. Toro, *Riemann Solvers and Numerical Methods for Fluid Dynamics: A Practical Introduction*, Springer, 1999.

[6] E. F. Toro, *Shock-Capturing Methods for Free-Surface Shallow Flows*, John Willy and sons LTD, 2001.

[7] E. F. Toro, Riemann problems and the WAF method for solving the two-dimensional shallow water equations, *J. Philos. Trans. R. Soc. London Ser.* 338, 1992, pp. 43–68.

[8] E. F. Toro and P. L. Roe, A hybridised high-order random choice method for quasi-linear hyperbolic systems, in *Proc. 16th Intern Symp. on Shock Tubes and Waves, Aachen, Germany, July 1987*, edited by Gronig, p. 701.

[9] G. Kesserwani and Q. Liang, Well-balanced RKDG2 solutions to the shallow water equations over irregular domains with wetting and drying, *Comput. Fluids* 39, 2010, pp. 2040–2050.

[10] G. Kesserwani and Q. Liang, A discontinuous Galerkin algorithm for the two-dimensional shallow water equations, *Comput. Methods Appl. Mech. Engrg* 199, 2010, pp. 3356–3368.

[11] H-R. Vosoughifar, A. Dolatshah, and S-K.S. Shokouhi , Discretization of multidimensional mathematical equations of dam break phenomena using a novel approach of finite volume method, *J. Appl. Math.*, 2013.

[12] H. Ozmen-Cagataya and S. Kocamanb, Dam-Break Flow in the Presence of Obstacle: Experiment and CFD Simulation, *Eng. Appl. Comp. Fluid.* 5, 4, 2011, pp. 541–552.

[13] K. Anastasiou and C. T. Chan, Solution of the 2D shallow water equations using the finite volume method on unstructured triangular meshs, *Int. J. Numer. Meth. Fluids.* 24, 1997, pp. 1225–1245.

[14] M. Maleewong, Modified predictor-corrector WAF method for the shallow water equations with source terms, *Math. Prob. Eng.* 2011

[15] O. Delestre, C. Lucas, P-A. Ksinant, F. Darboux, C. Laguerre, T.-N.-Tuoi Vo, F. James and S. Cordier, SWASHES: a compilation of shallow water analytic solutions for hydraulic and environmental studies, *Int. J. Numer. Meth. Fluids.* 2012, pp. 346–365.

[16] P. A. Tassi and C.-A. Vionnet, Discontinuous Galerkin method for the one dimensional simulation of shallow water flows, *Mecànica Computational Vol. XXII, Bahía Blanca*, 22, 2003, pp. 2403–2428.

[17] Q. Liang and A. G.L. Borthwick, Adaptive quadtree simulation of shallow flows with wet-dry fronts over complex topography, *Comput. Methods Appl. Mech. Engrg* 38, 2009, pp. 221–234.

[18] R. Ata, S. Pavan, S. Khelladi and E. F. Toro, A Weighted Average Flux (WAF) scheme applied to shallow water equations for real-life applications, *Adv. Water Resour.*, 62, 2013, pp. 155–172.

[19] R. J. Leveque, *Finite Volume Method for Hyperbolic Problem* Cambridge University Press, 2005.

[20] R. J. Leveque, *Numerical Methods for Conservation Laws*, Birkhäuser Verlag Press, 1992.

[21] S. J. Billett and E. F. Toro, On WAF-Type Schemes for Multidimensional Hyperbolic Conservation Laws, *J. COMPUT. PHYS.* 130, 1997, pp. 1–24.

[22] S. Noelle, N. Pankratz, G. Puppo and J. R. Natvig, Well-balanced finite volume schemes of arbitrary order of accuracy for shallow water flows, *J. Comput. Phys.* 213, 2006, pp. 474–499.

[23] W. Lai and A. A. Bouchut, Discontinuous Galerkin method for 1D shallow water flow with water surface slope Limiter, *Int. J. Civil and Env. Eng.* 3, 2011, pp. 167–176.

[24] Y. Loukili and A. W. Soulaïmani, Numerical tracking of shallow water waves by the unstructured finite volume WAF approximation, *Int. J. Comput. Methods Eng. Sci. Mech.* 8, 2007, pp. 75–88.

[25] Y. Xing and C. W. Shu, High order well-balanced finite volume WENO schemes and discontinuous Galerkin methods for a class of hyperbolic systems with source terms, *J. Comput. Phys.* 214, 2006, pp. 567–598.

[26] http://www.gistda.or.th

[27] http://www.hydro-5.com

[28] http://srtm.csi.cgiar.org

Chapter 3

Critical control in transcritical shallow-water flow over two obstacles

3.1 Introduction

3.1.1 Background

Shallow water flow of a homogeneous fluid over bottom topography is a fundamental problem in fluid mechanics and has been heavily studied from various points of view. A widely used approach when the topography is a single localised obstacle is the application of hydraulic concepts which lead to the classification of the flow in terms of the value of the upstream Froude number, defined as the ratio of the uniform upstream flow to the linear long wave speed. The flow is then described as supercritical, subrcritical or transcritical depending on whether the upstream Froude number is greater than unity, less than unity, or close to unity respectively, see for instance the monograph by Baines (1995) for a comprehensive account of hydraulic theory and the issues involved. In the supercritical case waves generated by the flow interaction with the obstacle propagate downstream away from the obstacle, and the flow at the obstacle location is a locally steady elevation. In the subcritical case, waves propagate upstream and downstream away from the obstacle, and the flow at the obstacle location is a locally steady depression. When wave dispersion is considered, steady lee waves are also formed downstream of the obstacle. Both these cases can be well understood, at least

qualitatively, using linearised theory.

However, linearized theory fails in the transcritical regime, which is the main interest here, and then a nonlinear theory is needed to describe the locally steady hydraulic flow over the obstacle, which has an upstream elevation and a downstream depression, each terminated by upstream and downstream propagating undular bores. A popular model here in the weakly nonlinear regime when the obstacle has a small amplitude is the forced Korteweg-de Vries (KdV) equation, see Akylas (1984), Cole (1985), Grimshaw and Smyth (1986), Lee et al. (1989), Binder et al. (2006), Grimshaw et al. (2007) and the recent review by Grimshaw (2010). Various aspects of the extension to finite amplitudes in the long wave regime can be found in El et al. (2006), El et al. (2008), and El et al. (2009).

Thus transcritical shallow water flow is quite well understood for a single localised obstacle, but there have been comparatively very few studies of the analogous case when the there are two widely separated localised obstacles. In the context of this article the most relevant is the article by Pratt (1984) where a combination of steady hydraulic theory, numerical simulations using the nonlinear shallow water equations and laboratory experiments are used to infer that the formation of dispersive waves between the obstacles is needed to obtain a stable solution. More recently Dias and Vanden-Broeck (2004) Ee et al. (2010, 2011) have examined the possible presence of such waves for steady flows, while Grimshaw et al. (2009) considered the related problem of unsteady flow over a wide hole. Thus a new feature of interest when considering two obstacles is that the waves generated by each obstacle may interact in the region between the two obstacles, and then the question is how this interaction might affect the long-time outcome. In this paper we examine this scenario using the nonlinear shallow water equations, so that although finite-amplitude effects are included, wave dispersion is neglected and the generated waves are represented as shock waves. Our emphasis is on the transcritical regime for two widely-spaced localised obstacles. The nonlinear shallow water equations are solved numerically using a well-balanced finite volume method, and the results are shown in section 3. The simulations are supplemented by a combination of fully nonlinear hydraulic theory with classical shock closure conditions, and a reduced model used in the weakly nonlinear regime, presented in section 2. We conclude in section 4.

3.1.2 Formulation

The basic model is one-dimensional shallow-water flow past topography, in which the flow is described by the total local depth H and the depth-averaged horizontal

velocity U. The forcing is due to a localised topographic obstacle $f(x)$ so that the bottom is at $z = -h + f(x)$ where h is the undisturbed depth at infinity. In non-dimensional coordinates, based on a length scale h, a velocity scale $\sqrt{gh}$ and a time-scale of $\sqrt{h/g}$, the equation system is

$$\zeta_t + (HU)_x = 0, \quad H = 1 + \zeta - f\,, \tag{3.1}$$

$$U_t + UU_x + \zeta_x = 0\,. \tag{3.2}$$

The upstream flow is a constant horizontal velocity $V > 0$ in dimensional coordinates, which becomes $F = V/\sqrt{gh}$, the Froude number, in the non-dimensional coordinate system. Here the topography $f(x)$ consists of two obstacles, each symmetrical, and placed a distance L apart, with respective maximum heights (or depths) of $\epsilon_{1,2}$. Our interest here is when $\epsilon_{1,2} > 0$, and the situation when either or both $\epsilon_{1,2} < 0$ will be considered elsewhere. We assume that the separation distance L is much greater than the width of the obstacles. Then the main parameters are the Froude number F, and the maximum heights $\epsilon_{1,2}$. This system is to be solved with the initial conditions

$$H = 1\,,\ U = F\,, \quad \text{at} \quad t = 0\,. \tag{3.3}$$

This is equivalent to introducing the obstacles instantaneously at $t = 0$ into a constant flow. The solution will initially develop smoothly, but being a nonlinear hyperbolic system, we can expect the development of discontinuities in the derivatives of ζ, U. The classical procedure is then to introduce shocks, given by

$$-S[\zeta] + [HU] = 0\,, \quad -S[HU] + [HU^2 + \frac{1}{2}H^2] = 0\,. \tag{3.4}$$

Here S is the shock speed, and $[\cdots]$ denotes the jump across the shock. In the absence of the bumps ($f(x) = 0$), these classical shocks conserve mass and momentum.

In the transcritical regime when $F \approx 1$, it will be useful also to consider a weakly nonlinear model for small-amplitude topography, given by

$$-\zeta_t - \Delta\zeta_x + \frac{3}{2}\zeta\zeta_x + \frac{f_x}{2} = 0\,, \quad \Delta = F - 1\,. \tag{3.5}$$

Here $U = F + u$ and $u \approx -\zeta$. The reduced model (3.5) can be seen as a dispersionless forced KdV equation, see the afore-mentioned references. For convenience we present an alternative derivation in the Appendix. The initial condition (3.3) is replaced by

$$\zeta = 0\,, \quad \text{at} \quad t = 0\,. \tag{3.6}$$

In this weakly nonlinear limit, the shock conditions (3.4) reduce to

$$(S-\Delta)[\zeta]+\frac{3}{4}[\zeta^2]=0\,. \tag{3.7}$$

This can also of course be directly deduced from (3.5).

3.2 Hydraulic flow

3.2.1 Steady solutions

Here we consider the hydraulic theory, and to begin with we review the well-known theory (see Baines (1995) for instance) for flow over a single obstacle obstacle. Then we will show how this can be extended to obtain analogous solutions for flow over two obstacles. Thus we seek steady solutions, so that on omitting the time derivatives, equations (3.1, 3.2) integrate to

$$HU=(1+\zeta-f)U=Q\,,\quad \zeta+\frac{U^2}{2}=B\,, \tag{3.8}$$

Here Q, B are positive integration constants, representing mass flux and energy flux respectively (strictly Q is volume flux, but we are assuming that the fluid density has been scaled to unity, and B is the Bernoulli constant, while BQ is the energy flux). Eliminating H or U gives

$$\frac{G^{4/3}}{2}+\frac{1}{G^{2/3}}=\frac{B+1-f}{Q^{2/3}}\,,\quad G=\frac{U}{H^{1/2}}=\frac{U^{3/2}}{Q^{1/2}}=\frac{Q}{H^{3/2}}\,. \tag{3.9}$$

which determines the local Froude number G as a function of the obstacle height f.

For noncritical flow, this solution must connect smoothly to $U=F, \zeta=0$, that is $G=F$, at infinity, and so $Q=F, B=F^2/2$. Noting that then the right-hand side of the first expression in (3.9) has a minimum value of $3/2-\epsilon_m$ when $F=1$, it can be established that

$$0<\epsilon_m<1+\frac{F^2}{2}-\frac{3F^{2/3}}{2}\,. \tag{3.10}$$

Here ϵ_m is the maximum obstacle height. This expression is plotted in figure 3.1 at equality (note that this is the curve BAE in figure 2.11 in Baines (1995)). It defines

the subcritical regime $F < F_b < 1$ where $F < G < 1$, and the supercritical regime $1 < F_p < F$ where $1 < G < F$ and a smooth steady hydraulic solution exists. In the subcritical regime a localised depression forms over the obstacle, and in the supercritical regime a localised elevation forms over the obstacle. For small $(\epsilon_m)^{1/2} << 1$, recalling that $\Delta = F - 1$, we find that

$$\Delta_{p,b} = \pm\frac{(6\epsilon_m)^{1/2}}{2} + \frac{\epsilon_m}{4} + O(\epsilon_m^{3/2})\,. \tag{3.11}$$

In the transcritical regime $F_b < F < F_p$ (3.10) does not hold and is replaced by

$$\epsilon_m > 1 + \frac{F^2}{2} - \frac{3F^{2/3}}{2}\,. \tag{3.12}$$

Instead we seek a solution which has upstream and downstream shocks propagating away form the obstacle, and which satisfies the critical flow condition at the top of the obstacle, that is, when $f = \epsilon_m$, $G_x \neq 0$. This condition implies that

$$G = 1\,, \quad \frac{3Q^{2/3}}{2} = B + 1 - \epsilon_m \quad \text{at} \quad f = \epsilon_m\,. \tag{3.13}$$

For a given ϵ_m, this relation defines B in terms of Q. At this critical location $U = U_m = Q^{1/3}$ and $1 + \zeta_m - \epsilon_m = Q^{2/3}$. The local Froude number varies over the range $G_- < G < G_+$ where $\pm$ denote the downstream and upstream values, It transpires that in order tor the shocks to propagate away from the obstacle the flow is subcritical upstream where $G_- < G < 1$, $\zeta_- > \zeta > \zeta_m$, $U_- < U < U_m$, and supercritical downstream $1 < G < G_+$, $\zeta_+ < \zeta < \zeta_m$, $U_+ > U > U_m$.

Before proceeding we note that the expressions (3.9) hold both upstream and downstream, yielding the relationships

$$U_\pm(1 + \zeta_\pm)^{1/2} = Q\,, \quad \frac{U_\pm^2}{2} + \zeta_\pm = B\,, \tag{3.14}$$

$$\text{and so} \quad \frac{U_\pm^2}{2} + \frac{Q}{U_\pm} = \frac{Q^2}{2(1+\zeta_\pm)^2} + \zeta_\pm + 1 = B + 1\,, \tag{3.15}$$

$$\text{while} \quad \frac{G_\pm^{4/3}}{2} + \frac{1}{G_\pm^{2/3}} = \frac{B+1}{Q^{2/3}}\,. \tag{3.16}$$

For given Q, B, these relations fix $U_\pm, \zeta_\pm$ completely. But we have one relationship (3.13) connecting B, Q, and so there is just a single constant to determine. This is found using the classical shock closure described in the next subsection.

3.2.2 Classical shock closure

Outside the obstacle $U = U_{\pm}, \zeta = \zeta_{\pm}$ are constants, downstream and upstream respectively, and are connected to the undisturbed values $U = F, \zeta = 0$ far downstream and upstream. using classical shock closure based on the shock conditions (3.4), see figure 3.2. Since the steady hydraulic flow over the obstacle conserves mass and energy, rather than mass and momentum, these are nontrivial conditions to apply. Further, it transpires that we cannot simultaneously impose upstream and downstream jumps which connect directly to the uniform flow. Instead, we first impose an upstream jump as specified by Baines (1995), see also El et al. (2009). There is then a downstream jump which connects to a rarefaction wave, see figure 3.2.

First we consider the upstream jump, which connects ζ_-, U_- to $0, F$ with $S_- < 0$. The first relation in (3.4) gives

$$\zeta_-(S_- - U_-) = U_- - F\,, \quad \text{or} \quad S_-\zeta_- = Q - F\,, \tag{3.17}$$

and the second relation in (3.4) gives

$$(1+\zeta_-)(U_- - F)(S_- - U_-) = \zeta_-(1 + \frac{\zeta_-}{2})\,. \tag{3.18}$$

Eliminating S_-, or $U_- - F$ yield the following expressions

$$(1+\zeta_-)(U_- - F)^2 = \zeta_-^2(1 + \frac{\zeta_-}{2})\,, \tag{3.19}$$

$$S_- = F - [(1+\zeta_-)(1 + \frac{\zeta_-}{2})]^{1/2}\,. \tag{3.20}$$

$$\text{and} \quad (1+\zeta_-)F - \zeta_-[(1+\zeta_-)(1 + \frac{\zeta_-}{2})]^{1/2} = Q\,. \tag{3.21}$$

Since we need $S_- < 0$ it follows that we must have $\zeta_- > 0$ and $U_- < Q < F$. The system of equations is now closed, as the combination of (3.15) and (3.21) determines ζ_- in terms of B, so that finally all unknowns are obtained in terms of ϵ_m from (3.13). Further, the condition $\zeta_- > 0$ serve to define the transcritical regime (3.12) in terms of the Froude number F and ϵ_m.

Downstream, this procedure also determines $U_+ > F, \zeta_+ < 0$, but in general, this cannot be resolved by a jump directly to the state $F, 0$. Instead we must insert a right-propagating rarefaction wave, see figure 3.2. The rarefaction wave

propagates downstream into the undisturbed state $0, F$, and so is defined by the values U_r, ζ_r where

$$U_r - 2(1+\zeta_r)^{1/2} = F - 2\,. \tag{3.22}$$

It is then connected to the hydraulic downstream state U_+, ζ_+ by a shock, using the jump conditions (3.4) to connect the two states through a shock with speed $S_+ > 0$. There are then three equations for the three unknowns ζ_r, U_r, S_+ and the system is closed.

In the weakly nonlinear regime, when the forcing is sufficiently small (the appropriate small parameter is $\alpha \sim \sqrt{\epsilon_m}$), the rarefaction wave contribution can be neglected as it has the amplitude of order α^3 while the shock intensity is $O(\alpha)$. In this limit we can solve the system of equations by an expansion in α and find that

$$3\zeta_\pm = 2\Delta \mp (6\epsilon_m + \beta_\pm)^{1/2} + O(\alpha^3)\,, \quad \beta_\pm = 3\zeta_\pm^3 - 2\zeta_\pm\Delta^2 + \frac{4\Delta^3}{9}\,, \tag{3.23}$$

$$S_\pm = \Delta - \frac{3\zeta_\pm}{4} + \frac{\zeta_\pm^2}{32} + O(\alpha^3)\,, \quad G_\pm = 1 + \Delta - \frac{3\zeta_\pm}{2} + \gamma_\pm + O(\alpha^3)\,, \quad \gamma_\pm = \frac{9\zeta_\pm^2}{8} - \frac{\zeta_\pm\Delta}{2}\,, \tag{3.24}$$

$$Q = 1 + \Delta + \zeta_\pm\Delta - \frac{3\zeta_\pm^2}{4} + O(\alpha^3)\,. \tag{3.25}$$

Here $\beta_\pm = O(\alpha^3)$, $\gamma_\pm = O(\alpha^2)$ are small correction terms, which if needed explicitly can be evaluated to leading order using the leading order solution for $\zeta_\pm$. It is useful to note here that using (3.23) and (3.11), the local Froude numbers

$$G_\pm = 1 \pm \frac{(6\epsilon_m)^{1/2}}{2} + O(\alpha^2) = 1 + \Delta_{p,b} + O(\alpha^2)\,, \tag{3.26}$$

and are independent of Δ at the leading order in α. Also, since the transcritical regime is defined by $\Delta_s < \Delta < \Delta_p$ it follows that at the leading order in α, the local downstream and upstream Froude numbers $G_\pm$ are outside this transcritical regime, and hence the downstream and upstream flows are indeed fully supercritical and subcritical respectively.

3.2.3 Two obstacles

The same procedure can now be followed when there are two widely separated obstacles, placed at $x = \pm L$ say. Based on our numerical simulations reported in section 3, the solution evolves in two stages. In the first stage the theory described

above can be applied to each obstacle separately. Then in the second stage when the downstream propagating waves emitted by the first obstacle interact with the upstream propagating waves waves emitted by the first obstacle, an interaction tales place and there is an adjustment to a new configuration. There are several scenarios depending on the obstacles heights $\epsilon_{1,2}$ and the Froude number F. For instance if both obstacles satisfy the condition (3.10) for subcritical or supercritical flow then the obtained solutions for each obstacle separately will again be obtained. On the other hand if both obstacles satisfy the condition (3.12) for transcritical flow then at the end of the first stage a downstream depression shock preceded by a rarefaction wave emitted by the first obstacle will meet an upstream elevation shock emitted by the second obstacle. Our numerical simulations show that these generate a new shock between the obstacles. The speed S_{int} of this shock can be found from (3.4) where the conservation of mass law implies that

$$S_{int}(\zeta_{2-} - \zeta_{1+}) = (1 + \zeta_{2-})U_{2-} - (1 + \zeta_{1+})U_{1+} + O(\alpha^3) = Q_2 - Q_1 + O(\alpha^3)\,. \tag{3.27}$$

Here the $O(\alpha^3)$ error is due to the presence of the rarefaction wave. Since $\zeta_{2-} > 0 > \zeta_{1+}$ the shock moves in the positive or negative direction depending on whether $Q_2 > (<) Q_1$. Indeed using the expressions (3.24, 3.21)

$$S_{int} = \Delta - \frac{3}{4}(\zeta_{1+} + \zeta_{2-}) + O(\alpha^2) = \frac{1}{4}(\{6\epsilon_1\}^{1/2} - \{6\epsilon_2\}^{1/2}) + O(\alpha^2)\,, \tag{3.28}$$

and is independent of Δ to this order. Thus, this shock will move towards the higher of the two obstacles, that is, S_{int} is positive or negative according as $\epsilon_1 > \epsilon_2$ or $\epsilon_1 < \epsilon_2$ respectively. This is followed by the interaction of this shock with either the second or first obstacle, followed eventually by an adjustment to a final localised steady state encompassing both obstacles; this is the second stage.

The final localised steady hydraulic state can now be determined as before, with the criterion that criticality occurs at the higher obstacle so that the formulae in subsections 2.1, 2.2 apply with $\epsilon_m = \max[\epsilon_1, \epsilon_2]$, the same as if the combination of the two obstacles was a single obstacle. Indeed, the criticality determined at the first stage at the higher obstacle persists into the second stage, while the flow at the lower obstacle adjusts in the second stage to be locally subcritical if the lower obstacle is the first obstacle, or is locally supercritical if the lower obstacle is the second obstacle. Illustrative example taken from the numerical simulations are shown in figures 3.3 and 3.4 respectively. Note that criticality is controlled by the higher obstacle which has the same height in the two cases, and hence the same constant values of Q, B are generated in the region containing both obstacles.

When the obstacles have equal heighta, $\epsilon_1 = \epsilon_2$, then also $Q_1 = Q_2$ and the shock speed $S_{int} = 0(\alpha^3)$, so that the error term in (3.27) is needed to determine the shock speed. This error term is due to the neglected rarefaction wave, and when this has a negative mass flux as sketched in the scenario shown in figure 3.2, $S_{int} < 0$. The numerical solutions show that this is indeed the case. Hence it is then the second obstacle which controls criticality. An example taken from our numerical simulations is shown in figure 3.5. In the region over both obstacles combined there is a steady state with constant values of Q, B satisfying the relation (3.13). The local Froude number $G = 1$ at the crest of the second obstacle, where G passes smoothly from subcritical $G < 1$ to supercritical $G > 1$. The flow is subcritical over the first obstacle, but $G = 1$ at the crest of the first obstacle. At this location there is a discontinuity in the slope of G, and hence also in the slopes of U, H, but all quantities are continuous This can be deduced from (3.9, 3.13) where near the crest of either obstacle

$$(G-1)^2 \approx \frac{3(\epsilon_m - f)}{2Q^{2/3}}\,. \tag{3.29}$$

There are two possible solutions. We consider for simplicity the generic case when $\epsilon_m - f \approx \delta(x \pm L)^2, \delta > 0$. Then at the second obstacle there is a smooth solution for which $G - 1 \approx C(x - L)$, $C = \sqrt{3\delta/2Q^{2/3}}$, but at the first obstacle the solution is $1 - G \approx C|x + L|$, which is continuous but has a discontinuous slope. This can be regarded as a stationary contact discontinuity. This scenario is asymmetrical and so differs from those considered by Pratt (1984) who examined only symmetrical configurations and showed these could not be stable. Further he pointed out that it is not possible to construct a steady stable solution using a stationary shock as this would then dissipate energy (see the last paragraph of his section 1 and footnote on page 1216).

3.2.4 Reduced model

Before presenting the numerical results, it is useful to examine the same scenario presented above in subsections 2.1, 2.2, 2.3 using the reduced model, especially as then the initial value problem can be solved, see Grimshaw and Smyth (1986) and Grimshaw (2010) for instance. With the initial condition that $\zeta = 0$ at $t = 0$, equation (3.5) can be solved using characteristics,

$$\begin{aligned} &\frac{dx}{dt} = \Delta - \frac{3\zeta}{2}\,, \quad \frac{d\zeta}{dt} = \frac{f_x}{2}\,, \\ &x = x_0\,, \quad \zeta = 0\,, \quad \text{at} \quad t = 0\,. \end{aligned} \tag{3.30}$$

The system (3.30) can be integrated to yield

$$\begin{aligned} &\Delta\zeta - \frac{3\zeta^2}{4} = \frac{1}{2}(f(x) - f(x_0))\,, \\ &3\zeta = 2\Delta \mp \Delta\{4\Delta^2 + 6[f(x_0) - f(x)]\}^{1/2}\,. \end{aligned} \tag{3.31}$$

Here the upper sign is chosen until the characteristic reaches a turning point where $2\Delta = 3\zeta$ and then the lower sign is chosen. When $\Delta = 0$ the upper (lower) sign is chosen on the left-hand (right-hand) side of the maximum point where $f = \epsilon_m$. Where characteristics intersect, a shock forms with speed S, given by (3.7) Then when

$$2\Delta^2 < 3\epsilon_{1,2}\,, \tag{3.32}$$

there is a critical x_{0c} for each obstacle such that all characteristics with $x_0 < x_{0c}$ have a turning point, propagate upstream and form an upstream shock. Otherwise all characteristics with $x_0 > x_{0c}$ have no turning points, propagate downstream and form a downstream shock. The critical point is defined by $3f(x_{0c}) = 3\epsilon_{1,2} - 2\Delta^2$. Then, in the first stage, a steady solution will emerge over each obstacle, terminated by upstream and downstream shocks, determined by that characteristic emanating from x_{0c} and the corresponding steady solution is found using (3.31)

$$\begin{aligned} &4\Delta^2 - 12\Delta\zeta + 9\zeta^2 = 6(\epsilon_m - f(x)) \\ &3\zeta = 2\Delta \mp \text{sign}[x \mp L]\{6[\epsilon_m - f(x)]\}^{1/2}\,. \end{aligned} \tag{3.33}$$

The upstream (downstream) shock has a magnitude $\zeta_\mp$ where

$$3\zeta_\mp = 2\Delta \pm \{6\epsilon_m\}^{1/2}\,, \tag{3.34}$$

respectively. Note that $\zeta_+ > 0, \zeta_- < 0$ so that the upstream shock is elevation and the downstream shock is depression. The speeds of these shocks are found from (3.7), that is

$$4S_\mp = 2\Delta \mp \{6\epsilon_m\}^{1/2}\,, \tag{3.35}$$

and $S_- < 0, S_+ > 0$. while the local Froude number is

$$G = 1 + \Delta - 3\zeta/2\,, \quad \text{and so} \quad G_\mp = 1 \mp \frac{\{6\epsilon_m\}^{1/2}}{2}\,. \tag{3.36}$$

In the first stage, this local steady solution holds only for each obstacle separately. When there are two obstacles the upstream elevation shock from the obstacle will

meet the downstream depression shock from the obstacle. This generates a new shock, with speed

$$S_{int} = \Delta - \frac{3}{4}(\zeta_{1+} + \zeta_{2-}) = \frac{1}{4}(\{6\epsilon_1\}^{1/2} - \{6\epsilon_2\}^{1/2}) \,, \tag{3.37}$$

which is independent of Δ, and is positive or negative according as $\epsilon_1 > \epsilon_2$ or $\epsilon_1 < \epsilon_2$ respectively. These results all agree with the small amplitude limits of the corresponding expressions in the preceding subsections..

3.3 Numerical results

3.3.1 Numerical method

The nonlinear shallow water equations (3.1,3.2) can be written as

$$\mathcal{U}_t + \mathcal{F}_x = \mathcal{G} \,, \tag{3.38}$$

where $\mathcal{U}$, $\mathcal{F}$ and $\mathcal{G}$ represent the density vector, flux vector, and source term respectively,

$$\mathcal{U} = \begin{bmatrix} H \\ UH \end{bmatrix} \,, \quad \mathcal{F} = \begin{bmatrix} UH \\ HU^2 + H^2/2 \end{bmatrix} \,, \quad \mathcal{G} = \begin{bmatrix} 0 \\ -Hf_x \end{bmatrix} \,. \tag{3.39}$$

The computational domain, $0 < x < x_L$, is discretised by uniform cell size Δx. The cell center is denoted by x_i where $x_{i-1/2}$ and $x_{i+1/2}$ refer the left and the right cell interface, respectively.

In discretization form, equation (3.38) can be written as

$$\frac{\mathcal{U}_i^{n+1} - \mathcal{U}_i^n}{\Delta t} \; + \; \frac{\mathcal{F}_{i+1/2}^n - \mathcal{F}_{i-1/2}^n}{\Delta x} \; = \; \mathcal{G}_i^n \tag{3.40}$$

Superscript n refers to time step level. The gradient of flux funtion is approximated by the difference of numerical fluxes at the left, $\mathcal{F}_{i-1/2}^n$, and the right, $\mathcal{F}_{i+1/2}^n$, of cell interfaces respectively. At the cell interface $i + 1/2$,

$$\mathcal{F}_{i+1/2}^n \; = \; \mathcal{F}(\mathcal{U}_{i+1/2-}^n, \mathcal{U}_{i+1/2+}^n) \,. \tag{3.41}$$

Numerical flux at the cell interface is a function of unknown variable on the left and the right limits, and

$$\mathcal{U}_{i+1/2-}^n = \begin{bmatrix} H_{i+1/2-}^n \\ H_{i+1/2-}^n U_i^{n^2} \end{bmatrix} \,, \quad \mathcal{U}_{i+1/2+}^n = \begin{bmatrix} H_{i+1/2+}^n \\ H_{i+1/2+}^n U_{i+1}^{n^2} \end{bmatrix} \,.$$

Applying the hydrostatic reconstruction from Audusse et al. (2004),

$$H^n_{i+1/2-} \;=\; \max(0, H_i + f_i - f_{i+1/2})\,, \;\text{ and }\; H^n_{i+1/2+} \;=\; \max(0, H_{i+1} + f_{i+1} - f_{i+1/2})\,.$$

Bottom slope is now included in the reconstruction of water depth. The value of bottom height at the corresponding interface is approximated by upwind evaluation,

$$f_{i+1/2} \;= \max(f_i, f_{i+1})\,.$$

To obtain a well-balanced scheme, the gradient of source term and flux difference must be balanced at steady state, Audusse et al. (2004), so equation (3.40) can be rewritten as,

$$\frac{\mathcal{U}_i^{n+1} - \mathcal{U}_i^n}{\Delta t} \;+\; \frac{\mathcal{F}_l^n(\mathcal{U}_i^n, \mathcal{U}_{i+1}^n, f_i, f_{i+1}) - \mathcal{F}_r^n(\mathcal{U}_{i-1}^n, \mathcal{U}_i^n, f_{i-1}, f_i)}{\Delta x} \;=\; 0\,, \quad (3.42)$$

with modified numerical fluxes,

$$\mathcal{F}_l^n(\mathcal{U}_i^n, \mathcal{U}_{i+1}^n, f_i, f_{i+1}) \;=\; \mathcal{F}(\mathcal{U}^n_{i+1/2-}, \mathcal{U}^n_{i+1/2+}) + \left[0, H_i^{n^2} - H^{n^2}_{i+1/2-}\right]/2\,,$$

$$\mathcal{F}_r^n(\mathcal{U}_i^n, \mathcal{U}_{i+1}^n, f_i, f_{i+1}) \;=\; \mathcal{F}(\mathcal{U}^n_{i+1/2-}, \mathcal{U}^n_{i+1/2+}) + \left[0, H_{i+1}^{n^2} - H^{n^2}_{i+1/2+}\right]/2\,.$$

In this work, we apply weighted average flux (WAF) proposed by Siviglia and Toro (2009); Toro (1992); Toro et al. (1994) to obtain the approximation of $\mathcal{F}(\mathcal{U}^n_{i+1/2-}, \mathcal{U}^n_{i+1/2+})$. We also apply the minmod flux limiter based on the total variation diminishing (TVD) proposed by Toro (1992) in our numerical scheme to remove spurious oscillations when simulating moving shock problem.

In our simulations, we apply transmissive boundaries to allow waves to propagate outwards on both boundaries. The bottom elevation is assumed to be two Gaussian obstacles given by

$$f(x) = \epsilon_1 \exp\left(-(x - x_a)^2/w\right) + \epsilon_2 \exp\left(-(x - x_b)^2/w\right)\,,$$

where ϵ_1 and ϵ_2 are the obstacle heights, x_a and $x_b = x_a + L$ are the center locations of the first and the second obstacle respectively, and the width of each obstacle is $w = 10$.

3.3.2 Equal obstacle heights

$\epsilon_1 = 0.1, \epsilon_2 = 0.1$

Simulations for a subcritical case $F = 0.5$ are shown in figure 3.6. Initially, in the first stage ($t = 50$), steady depression waves are produced over each obstacle, and

small transient elevation waves travel upstream from each obstacle. In the second stage $t = 70$ the transient wave from the second obstacle has passed over the first obstacle and proceeded upstream. In the final stage ($t = 300$) only the steady depression waves over each obstacle are left. In this case, the Froude number is outside the transcritical regime for both obstacles, see (3.10) and figure 3.1,.

Simulations for a transcritical flow case $F = 1$ are shown in figure 3.7. In the first stage ($t = 50$) a transcritical flow is generated over each obstacle separately, consisting of an elevation shock propagating upstream connected by a steady solution to a depression shock propagating downstream. The depression shock from the first obstacle meets the elevation shock from the second obstacle at around $t = 130$ forming a single shock, which then propagates upstream. In the second stage ($t = 400$), there is an adjustment in which a locally steady subcritical depression wave forms over the first obstacle, while a locally steady transcritical flow forms over the second obstacle. At the same time the elevation shock and depression shock outside both obstacles continue to propagate in their separate ways. As time increases ($t = 1000$), the flow over both obstacles reaches a locally steady state with criticality controlled by the second obstacle while the flow is subcritical over the first obstacle, but as mentioned above, reaches criticality ($G = 1$) at the obstacle crest where there is a discontinuity in slope, see also figure 3.5. We note that very high resolution is needed to resolve this discontinuity and coarse resolution runs show a smooth G reaching a value slightly below 1.

Next, we examine a quantitative comparison between the nonlinear shallow water simulations and the theoretical results from the reduced model presented in section 3.2. From the numerical simulations shown in figure 3.7 over the time range $t = 400$ to 1000 we find that the respective shock magnitudes and speeds, $\zeta_+ = -0.2574, \zeta_- = 0.2670, S_+ = 0.1880, S_- = -0.1980$. With $\epsilon_m = 0.1$ the local Froude numbers in equation (3.36) are $G_+ = 1.3873, G_- = 0.6127$, while the shock magnitudes from equation (3.34) are $\zeta_+ = -0.2582, \zeta_- = 0.2582$, and the shock speeds from (3.35) are $S_+ = 0.1937, S_- = -0.1937$. These values are in reasonable agreement with the numerical determined values. Using the more exact formulas (3.23, 3.24) up to the $O(\alpha^2)$ terms leads to $\zeta_+ = -0.2468, \zeta_- = 0.2691$ and $S_+ = 0.1871, S_- = -0.1996$, which is an improvement. Note that the effective small parameter here is $(6\epsilon_m)^{1/2} = 0.7746$ and so is not small enough for the reduced model to be completely accurate.

Simulations for a supercritical flow case $F = 1.5$ are shown in Figure 3.8. Initially, in the first stage ($t = 30$), steady elevation waves are produced over each obstacle, and small transient depression waves travel downstream from each obstacle. At the beginning of the second stage ($t = 70$) the transient wave from

the first obstacle is passing over the second obstacle and proceeded upstream. In the final stage ($t = 400$) only the steady elevation waves over each obstacle are left. In this case, the Froude number is outside the transcritical regime for both obstacles, see (3.10) and figure 3.1,.

It should be noted that in the reduced model the local Froude number (3.36) satisfies $0.6127 < G < 1.3873$ for $\epsilon_m = 0.1$. This prediction is consistent with the nonlinear simulations shown in figure 3.6 for subcritical flow, figure 3.7 for transcritical flow, and figure 3.8 for supercritical flow.

$\epsilon_1 = 0.2, \epsilon_2 = 0.2$

Four simulations for $F = 0.5, 1.0, 1.5, 2.0$ are shown in figures 3.9 - 3.12. When $\epsilon_m = 0.2$ transcritical flow occur in the range of $0.48 < F < 1.56$, see (3.10) and figure 3.1. The reduced model predicts transcritical flow when $0.45 < F < 1.55$, see (3.11). Thus the flow is slightly transcritical for $F = 0.5, 1.5$, respectively nearly subcritical or supercritical, while it is transcritical for $F = 1.0$, and supercritical for $F = 2.0$. In all these cases we expect the reduced model to provide a quite good interpretation.

The nearly subcritical case shown in figure 3.9 can be compared with the subcritical case shown in figure 3.6 for $\epsilon_1 = \epsilon_2 = 0.1$. Although the first stage($t = 30, 60$) is similar there is now visible two small rarefaction waves propagating to the left, and in the second stage ($t = 130, 800$) a pronounced asymmetry develops with a larger depression wave over the second obstacle. This is due to this case being in the transcritical regime, and hence the second obstacle controls criticality.

The transcritical case shown in figure 3.10 is qualitatively similar to that in figure 3.7 for $\epsilon = 0.1, \epsilon = 0.1$. From the numerical simulations shown in figure 3.7 over the time range $t = 40$ to 800 we find that the respective shock magnitudes and speeds, $\zeta_+ = -0.3600, \zeta_- = 0.3810, S_+ = 0.2535, S_- = -0.2814$. With $\epsilon_m = 0.2$ the local Froude numbers in equation (3.36) are $G_+ = 1.5477, G_- = 0.4523$, while the shock magnitudes from equation (3.34) are $\zeta_+ = -0.3651, \zeta_- = 0.3651$, and the shock speeds from (3.35) are $S_+ = 0.2739, S_- = -0.2739$. These values are in reasonable agreement with the numerical determined values. Using the more exact formulas (3.23, 3.24) up to the $O(\alpha^2)$ terms leads to $\zeta_+ = -0.3422, \zeta_- = 0.3867$ and $S_+ = 0.2603, S_- = -0.2853$, which is overall some improvement. But note here that the effective small parameter is $(6\epsilon_m)^{1/2} = 1.0954$ and can hardly be considered small.

The nearly supercritical case shown in figure 3.11 can be compared with the

supercritical case shown in figure 3.8 for $\epsilon_1 = \epsilon_2 = 0.1$. Although the first stage($t = 300$) is rather similar there is already an asymmetry in that the elevation wave other the second obstacle is already slightly smaller than that over the first obstacle, indication that the adjustment process to the second stage is beginning. This adjustment continues at $t = 300$ and the final locally steady state is achieved at $t = 660, 1200$, in which there is criticality controlled by the second obstacle, and a locally subcritical flow over the first obstacle.

The fully supercritical case is shown in figure 3.12 and can also be compared with the supercritical case shown in figure 3.8 for $\epsilon_1 = \epsilon_2 = 0.1$. It is quite similar although the time then to reach the second stage is much shorter.

3.3.3 Unequal obstacle heights

$\epsilon_1 = 0.01, \epsilon_2 = 0.02$**, and** $\epsilon_1 = 0.1, \epsilon_2 = 0.2$

A transcritical case ($F = 1$) when the second obstacle is larger is shown in figure 3.13 for quite small amplitudes. At the first stage ($t = 50$), each obstacle generates elevation and depression shocks that can be described by the single obstacle theory. As time increases ($t = 460$) the depression shock from the first obstacle interacts with the upstream elevation shock generated by the second obstacle. A new shock is formed, called an intermediate shock as described in the analysis of section 2. Since the second obstacle is larger, the intermediate shock travels upstream and pasts over the first obstacle, leaving a locally steady depression wave in a locally subcritical flow ($t = 1000$). The speed of the intermediate shock is greater than the speed of the travelling elevation shock from the first obstacle. These two shocks merge and finally form a new shock moving further upstream ($t = 1800$).

Next, we compare quantitatively these nonlinear simulations with theoretical results of from section 2. For $\epsilon_1 = 0.01$, we find from the nonlinear simulations that the upstream shock magnitude and speed are $\zeta_- = 0.0822$, and $S_- = -0.0615$, while the reduced model predicts that $\zeta_- = 0.0816$ and $S_- = -0.0612$, and using the more exact formulae (3.23, 3.24) leads to $\zeta_- = 0.0828$ and $S_- = -0.0619$. Similarly, for the second obstacle with $\epsilon_2 = 0.02$, the downstream shock magnitude and speed from the simulations are $\zeta_+ = 0.1134$, and $S_+ = 0.0847$ while the reduced model predicts that $\zeta_+ = -0.1155$ and $S_+ = 0.0866$, and using the more exact formulae (3.23, 3.24) leads to $\zeta_+ = 0.1132$, and $S_+ = 0.0853$. These comparisons show very good agreement for these small amplitude obstacles. Further, the intermediate shock speed from the simulation is $S_{int} = -0.0262$,

while the theoretical expression (3.37) yields $S_{int} = -0.0254$. Also, note that for the nonlinear simulations when $t = 1000 - 1800$, the two upstream elevation shocks merge to form a new one with the new speed $S_- = -0.0867$ which is nearly the addition of S_{int} and S_- (for $\epsilon_1 = 0.01$).

A case with higher obstacle amplitudes, $\epsilon_1 = 0.1, \epsilon_2 = 0.2$ is shown in figure 3.14. The long-time outcome for this case is shown in figure 3.3. The flow behaviour is quite similar to the smaller amplitude case. Here the intermediate shock speed from the simulation is $S_{int} = -0.1286$, but from equation (3.37), $S_{int} = -0.0802$. The quite large difference is due to higher order nonlinear effects.

$\epsilon_1 = 0.02, \epsilon_2 = 0.01$**, and** $\epsilon_1 = 0.2, \epsilon_2 = 0.1$

A transcritical case ($F = 1$) when the first obstacle is larger is shown in figure 3.15 for quite small amplitudes. At the first stage ($t = 150$), each obstacle generates elevation and depression shocks that can be described by the single obstacle theory. As time increases ($t = 460$), the downstream depression shock from the first obstacle interacts with the upstream elevation shock generated by the second obstacle, and an intermediate shock is formed. Since the first obstacle is larger, it now controls criticality. The intermediate shock travels downstream and passes over the second obstacle, leaving a locally steady elevation wave ($t = 1400$) in a locally supercritical flow. The speed of the intermediate shock is greater than the speed of the downstream travelling depression shock from the second obstacle. These two shocks merge and form a new shock moving further downstream ($t = 1800$).

Next, we compare quantitatively these nonlinear simulations with the theoretical results. For $\epsilon_1 = 0.02$, we find from the nonlinear simulations that the upstream shock magnitude and speed are $\zeta_- = 0.1170$, and $S_- = -0.0880$, while the reduced model predicts that $\zeta_- = 0.1155$ and $S_- = -0.0866$, and using the more exact formulae (3.23, 3.24) leads to $\zeta_- = 0.1165, S_- = -0.0870$. Similarly, for the second obstacle with $\epsilon_2 = 0.01$, the downstream shock magnitude and speed from the simulations are $\zeta_+ = -0.0811$, and $S_+ = 0.0607$, while the reduced model predicts that $\zeta_+ = -0.0816$, and $S_+ = 0.0612$, and using the more exact formulae (3.23, 3.24) leads to $\zeta_- = 0.0802, S_- = -0.0604$. These comparisons show very good agreement for small amplitude obstacles. Further, the intermediate shock speed from the simulation is $S_{int} = 0.0260$, while the theoretical expression (3.37) yields $S_{int} = 0.0254$. Also, note that for the nonlinear simulations when $t = 1400 - 1800$, the two downstream depression shocks merge

to form a new shock with the new speed $S_+ = 0.0812$, which is nearly the addition of S_{int} and S_+(for $\epsilon = 0.01$).

A case with higher obstacle amplitudes, $\epsilon = 0.2, \epsilon_2 = 0.1$ is shown in figure 3.16. The long-time outcome for this case is shown in figure 3.4. The flow behaviour is similar to the smaller amplitude case. Here the intermediate shock speed from the simulation is $S_{int} = 0.0281$, but from equation (3.37), $S_{int} = 0.0802$. Again, the quite large difference is due to higher order nonlinear effects.

3.4 Summary

Transcritical shallow-water flow over two localised and widely-spaced obstacles has been examined using the fully nonlinear shallow water equations (3.1, 3.2) and interpreted with a combination of numerical simulations and theoretical analysis based on hydraulic flow concepts. For a single obstacle, it is well-known that the solution is a locally steady hydraulic flow over the obstacle contained between an upstream elevation shock and a downstream depression shock. For the case of two obstacles our numerical results and supporting theory show that there two stages. In the first stage, the flow interacts with each obstacle independently, each well described by the single obstacle theory, and in particular the first obstacle generates a downstream propagating depression shock, while the second obstacle generates an upstream propagating elevation shock. Then in the second stage the downstream propagating depression shock from the first obstacle interacts with the upstream propagating elevation shock from the second obstacle to produce an intermediate shock, which propagates towards the larger obstacle, or if the obstacles have equal heights, towards the second obstacle. There is an adjustment to a locally steady flow over both obstacles combined, where the higher obstacle obstacle controls criticality. If the obstacles have equal heights, then the second obstacle controls criticality and the flow is subcritical over the first obstacle, but the local Froude number reaches unity at the crest of the first obstacle, where there is a discontinuity in the solution slope. This outcome agrees with the analytical theory based on hydraulic flow concepts extended here form a single obstacle to two obstacles.

As is known, the case of flow over a single negative obstacle, or hole, is more complicated, as the shock waves are generated at the obstacle location, see Grimshaw and Smyth (1986), Grimshaw et al. (2007) and Grimshaw et al. (2009). Hence we expect the case when either or both of the obstacles are holes could

lead to different and more complicated scenarios, which will be the subject of a future study. Further the present study is restricted to non-dispersive waves and extensions to include even just weak dispersion using the forced KdV equation, or the fully nonlinear Su-Gardner equations, as done by El et al. (2009) for a single obstacle, will certainly lead to rather different behaviour. In that case, the shocks are replaced by undular bores and the shock interactions described here are replaced by the interactions of these nonlinear wave trains. For instance some of the numerical simulations reported by Grimshaw et al. (2009) using just the forced KdV equation indicate that the interaction of these nonlinear wave trains can produce very complicated behaviour, at least during the initial stages of the flow development. This also is a topic needing much further study.

Bibliography

Akylas, T. R. (1984). On the excitation of long nonlinear water waves by moving pressure distribution. *J. Fluid Mech.*, 141:455–466.

Audusse, E., Bouchut, F., Bristeau, M.-O., Klein, R., and Perthame, B. (2004). A fast and stable well-balanced scheme with hydrostatic reconstruction for shallow water flows. *SIAM J. Sci. Com.*, 25:2050Ð2065.

Baines, P. (1995). *Topographic effects in stratified flows*. CUP.

Binder, B., Dias, F., and Vanden-Broeck, J.-M. (2006). Steady free-surface flow past an uneven channel bottom. *Theor. Comp. Fluid Dyn.*, 20:125–144.

Cole, S. L. (1985). Transient waves produced by flow past a bump. *Wave Motion*, 7:579–587.

Dias, F. and Vanden-Broeck, J. M. (2004). Trapped waves between submerged obstacles. *J. Fluid Mech.*, pages 93–102.

Ee, B. K., Grimshaw, R. H. J., Chow, K. W., and Zhang, D.-H. (2011). Steady transcritical flow over a hole: Parametric map of solutions of the forced KortewegÐde Vries equation. *Phys. Fluids*, page 04662.

Ee, B. K., Grimshaw, R. H. J., Zhang, D.-H., and Chow, K. W. (2010). Steady transcritical flow over an obstacle: Parametric map of solutions of the forced extended KortewegÐde Vries equation. *Phys. Fluids*, page 056602.

El, G., Grimshaw, R., and Smyth, N. (2006). Unsteady undular bores in fully nonlinear shallow-water theory. *Phys. Fluids*, 18:027214.

El, G., Grimshaw, R., and Smyth, N. (2008). Asymptotic description of solitary wave trains in fully nonlinear shallow-water theory. *Physica D*, 237:2423–2435.

El, G., Grimshaw, R., and Smyth, N. (2009). Transcritical shallow-water flow past topography: finite-amplitude theory. *J. Fluid Mech.*, 640:187–214.

Grimshaw, R. (2010). Transcritical flow past an obstacle. *ANZIAM J.*, 52:1–25.

Grimshaw, R. and Smyth, N. (1986). Resonant flow of a stratified fluid over topography. *J. Fluid Mech.*, 169:429–464.

Grimshaw, R., Zhang, D., and Chow, K. (2007). Generation of solitary waves by trancritical flow over a step. *J. Fluid Mech.*, 587:235–354.

Grimshaw, R., Zhang, D.-H., and Chow, K. W. (2009). Transcritical flow over a hole. *Stud. Appl. Math.*, 122:235–248.

Lee, S.-J., Yates, G., and Wu, T.-Y. (1989). Experiments and analyses of upstream-advancing solitary waves generated by moving disturbances. *J. Fluid Mech.*, 199:569–593.

Pratt, L. J. (1984). On nonlinear flow with multiple obstructions. *J. Atmos. Sci.*, 41:1214–1225.

Siviglia, A. and Toro, E. (2009). WAF method and splitting procedure for simulating hydro-and thermal-peaking waves in open-channel flows. *J. Hydraul. Eng.*, 135:651–662.

Toro, E. (1992). Riemann problems and the WAF method for solving two-dimensional shallow water equations. *Philos. Trans. R. Soc. London Ser. A*, 338:43–68.

Toro, E., Spruce, M., and Speares, W. (1994). Restoration of the contact surface in the HLL-Riemann solver. *Shock wave*, 4:25–34.

Appendix

The weakly nonlinear model (3.5) for small-amplitude topographic forcing in the transcritical regime can be derived as follows. First, we introduce the Riemann variables

$$R = U + 2C\,, \quad L = U - 2C\,, \quad C = \sqrt{H}\,, \tag{3.43}$$

so that equations (3.1, 3.2) become

$$R_t + (U + C)R_x + f_x = 0\,, \quad L_t + (U - C)L_x + f_x = 0\,. \tag{3.44}$$

Then we assume that $f \sim \alpha^2$ where $\alpha \ll 1$, and that $\zeta \sim \alpha$, $u = U - F \sim \alpha$, and $\Delta = F - 1 \sim \alpha$. Next, noting that $U + C = F + 1 + O(\alpha)$, we can find an approximation the right-going Riemann invariant in the vicinity of the topography,

$$R = F + 2 - \frac{f}{2} + O(\alpha^3)\,, \quad \text{so that} \quad u + \zeta = \frac{\zeta^2}{4} + \frac{f}{2} + O(\alpha^3)\,. \tag{3.45}$$

Here a transient propagating rapidly with a speed $F + 1 + O(\alpha)$ to the right is ignored. Then we find that for the left-going Riemann invariant,

$$\begin{aligned} L &= 2U - (F + 2) + \frac{f}{2} + O(\alpha^3) = F - 2 - 2\zeta + \frac{\zeta^2}{2} + \frac{3f}{2} + O(\alpha^3)\,, \\ U - C &= \frac{3U}{2} - \frac{F + 2}{2} + \frac{f}{4} + O(\alpha^3) = \Delta - \frac{3\zeta}{2} + O(\alpha^2)\,. \end{aligned} \tag{3.46}$$

Thus finally the equation for L in (3.44) reduces to (3.5), with an error of $O(\alpha^3)$. Similarly the mass shock condition in (3.4) reduces to (3.7) with an error of $O(\alpha^3)$, while the momentum shock condition has all terms of $O(\alpha^3)$.

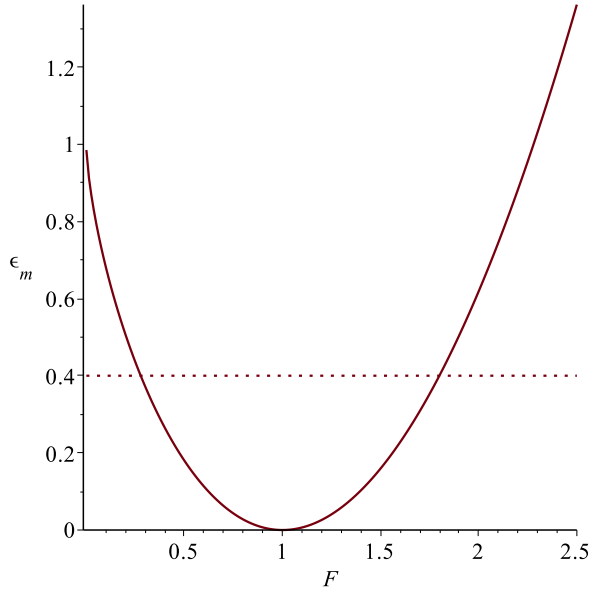

Figure 3.1: Plot of (3.10) at equality. The intersection of the line $\epsilon_m =$ constant with the curve (3.10) defines $F_{b,p}$ respectively. The region below the curve defines the subcritical and supercritical regimes, and the region above the curve is the transcritical regime.

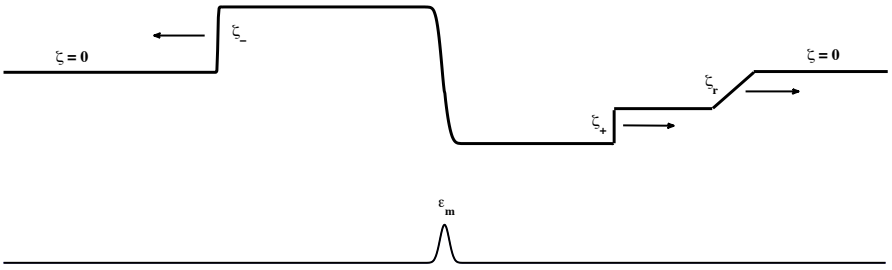

Figure 3.2: Schematic for closure using classical shocks.

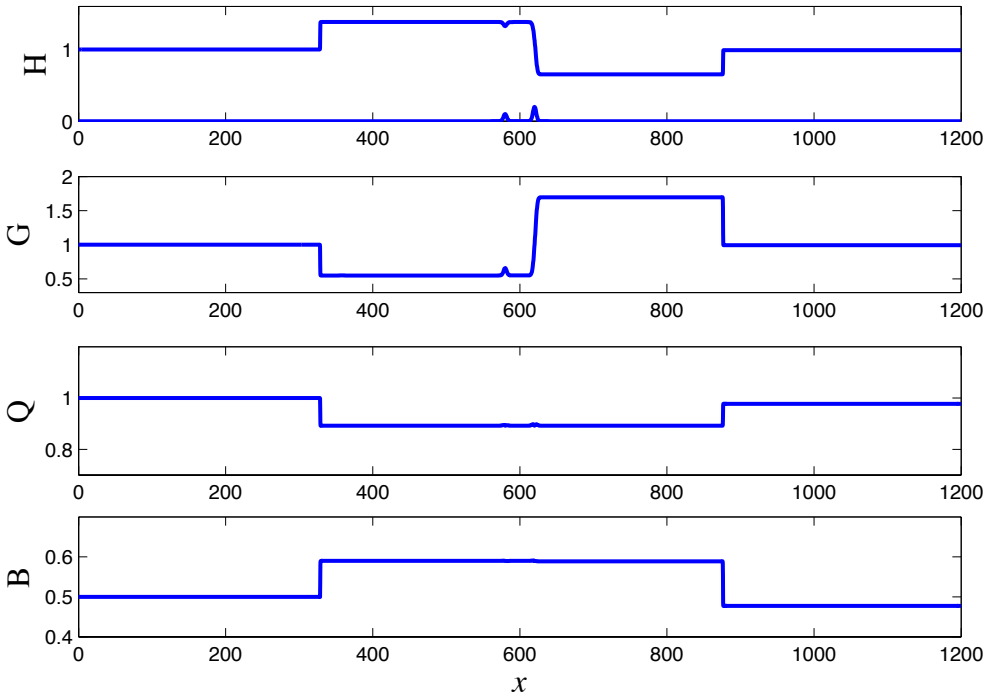

Figure 3.3: Hydraulic solution for the case $F = 1$ and unequal obstacle heights $\epsilon_1 = 0.1, \epsilon_2 = 0.2$. In the steady region over both obstacles $Q = 0.8923$ and $B = 0.5900$, and $G = 0.6584$ at the crest of the first obstacle where the flow is locally subcritical.

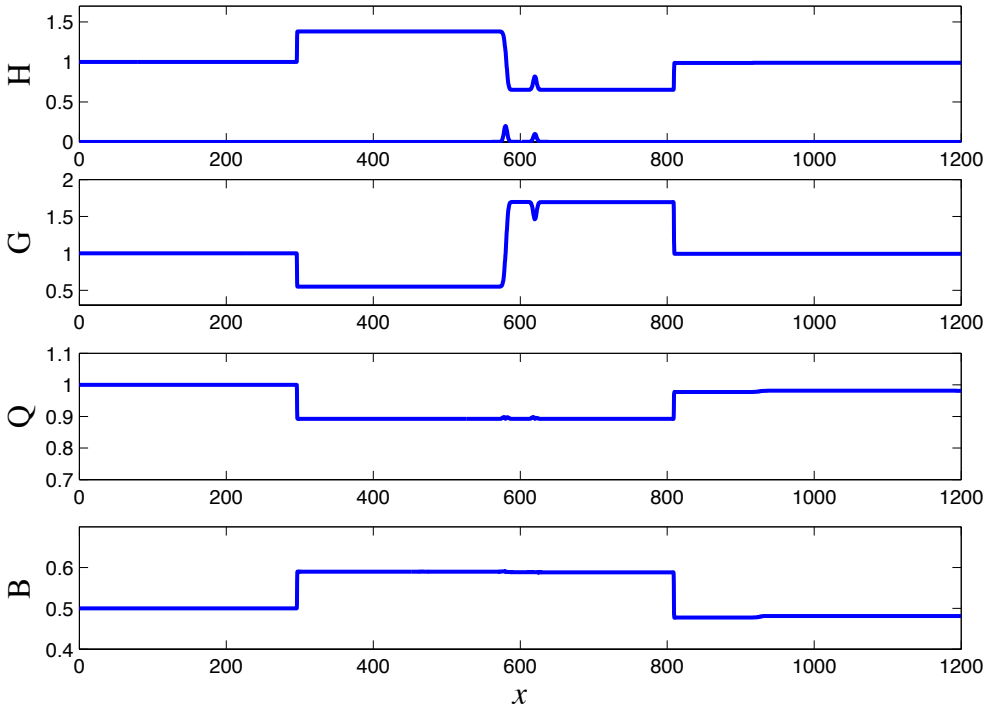

Figure 3.4: Hydraulic solution for the case $F = 1$ and unequal obstacle heights $\epsilon_1 = 0.2, \epsilon_2 = 0.1$. In the steady region over both obstacles $Q = 0.8923$ and $B = 0.5900$, and $G = 1.463$ at the crest of the second obstacle where the flow is locally supercritical.

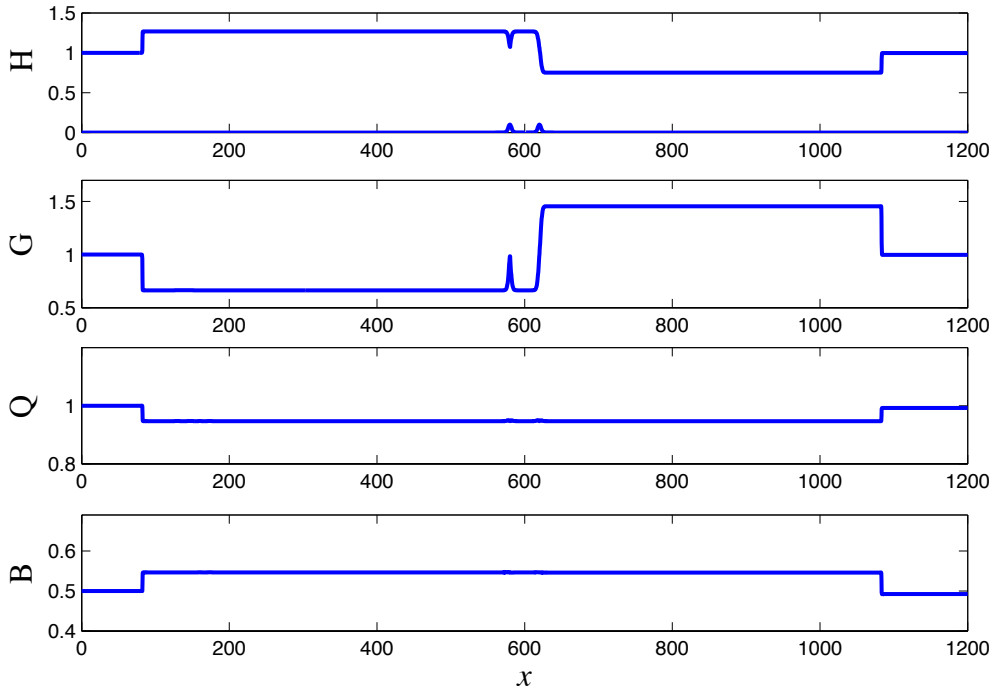

Figure 3.5: Hydraulic solution for the case $F = 1$ and equal obstacle heights $\epsilon_1 = \epsilon_2 = 0.1$ In the steady region over both obstacles $Q = 0.9469$ and $B = 0.5464$, and $G = 1$ at the crest of the first obstacle, but $G < 1$ in the vicinity of the first obstacle where the flow is locally subcritical.

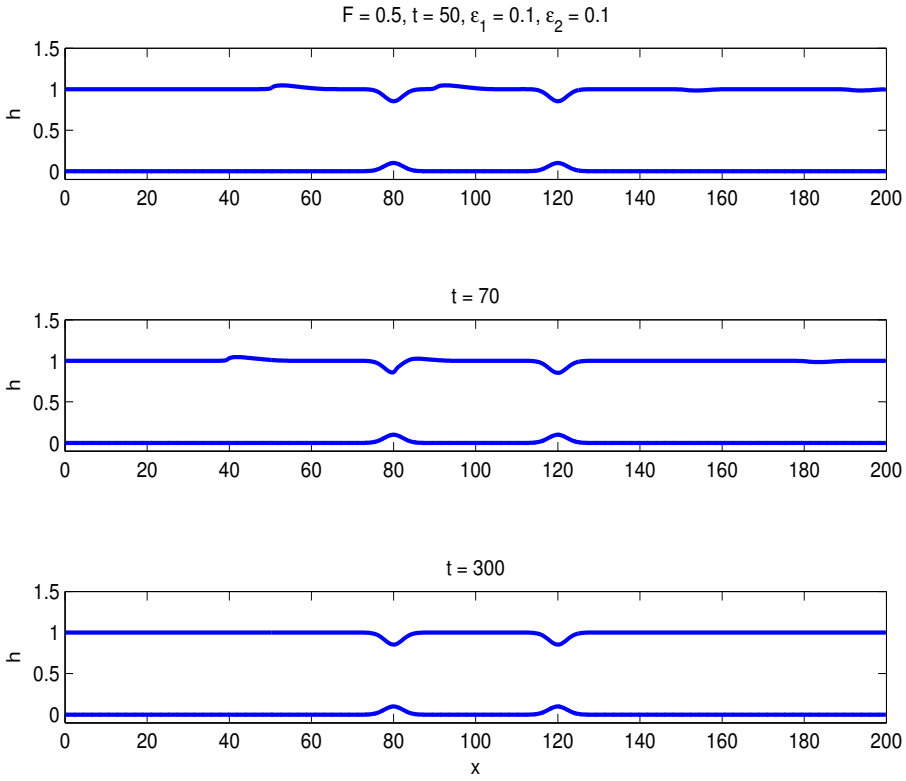

Figure 3.6: Simulations for $F = 0.5, \epsilon_1 = 0.1, \epsilon_2 = 0.1$.

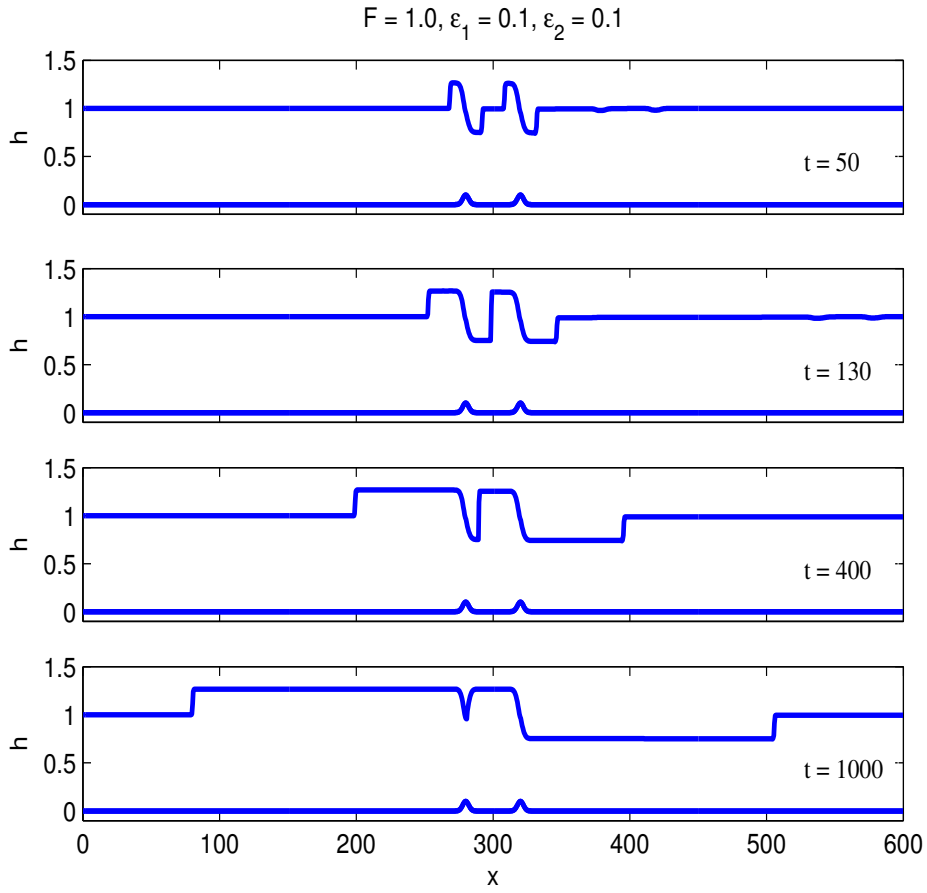

Figure 3.7: Simulations for $F = 1.0, \epsilon_1 = 0.1, \epsilon_2 = 0.1$.

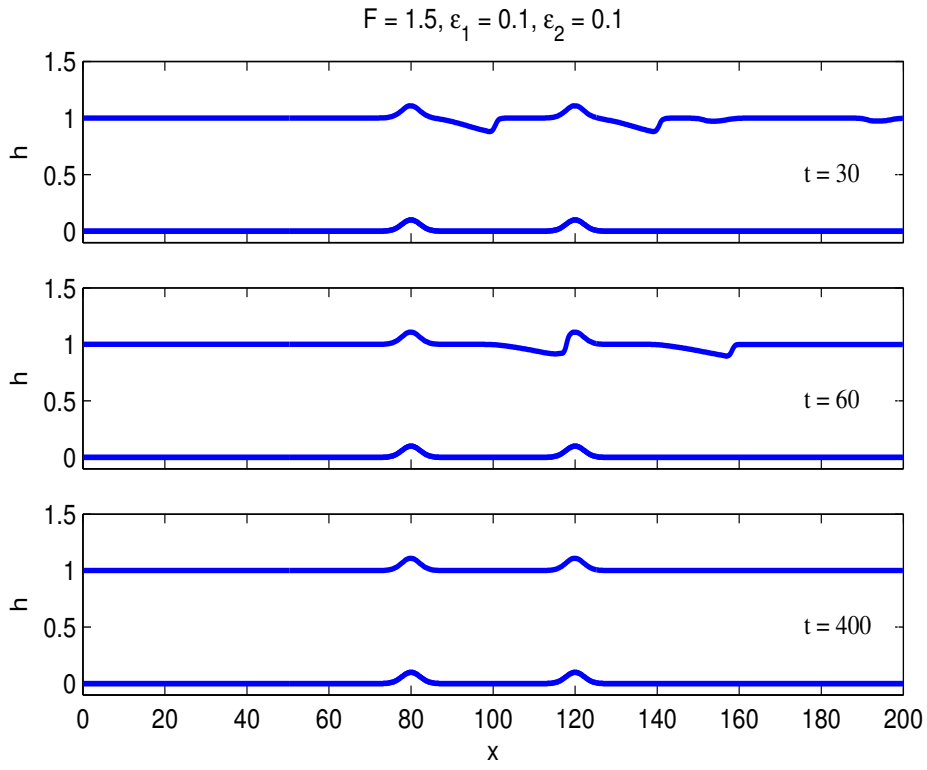

Figure 3.8: Simulations for $F = 1.5, \epsilon_1 = 0.1, \epsilon_2 = 0.1$.

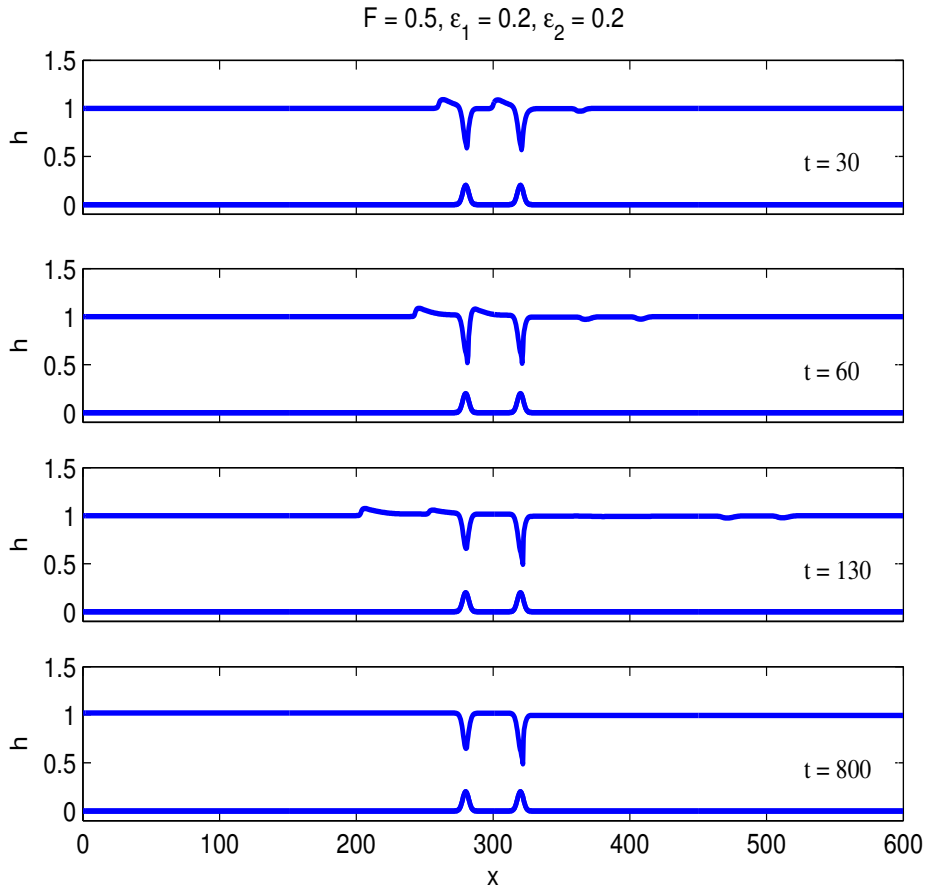

Figure 3.9: Simulations for $F = 0.5, \epsilon_1 = 0.2, \epsilon_2 = 0.2$.

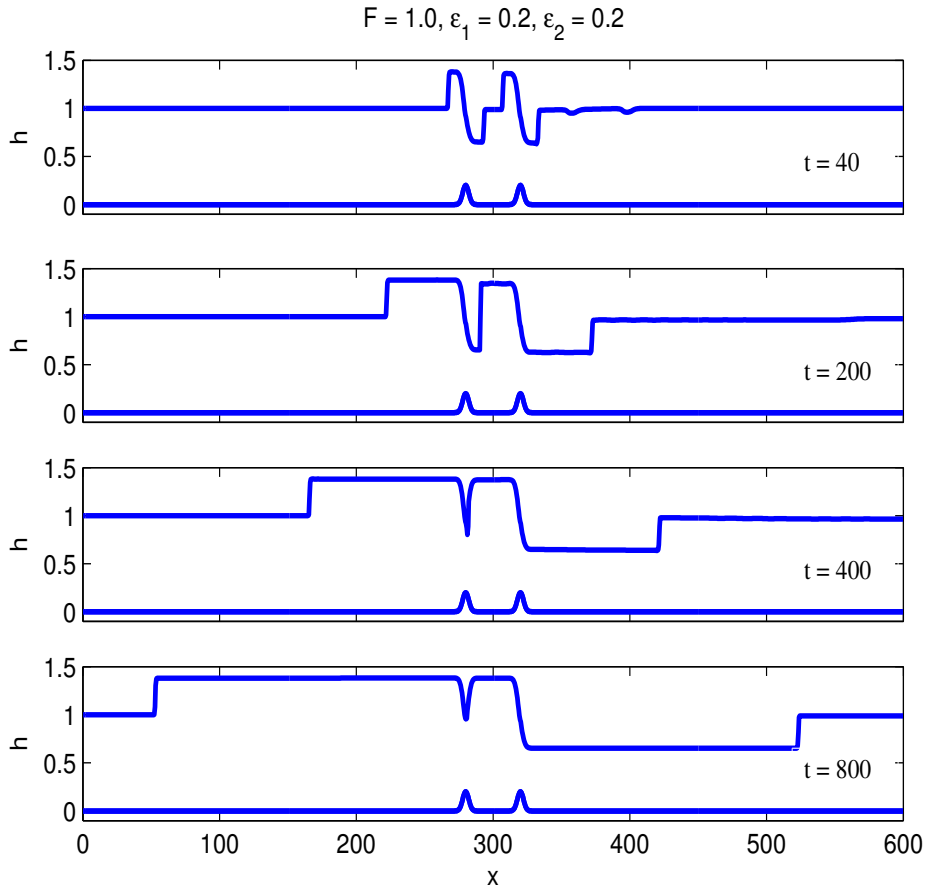

Figure 3.10: Simulations for $F = 1.0, \epsilon_1 = 0.2, \epsilon_2 = 0.2$.

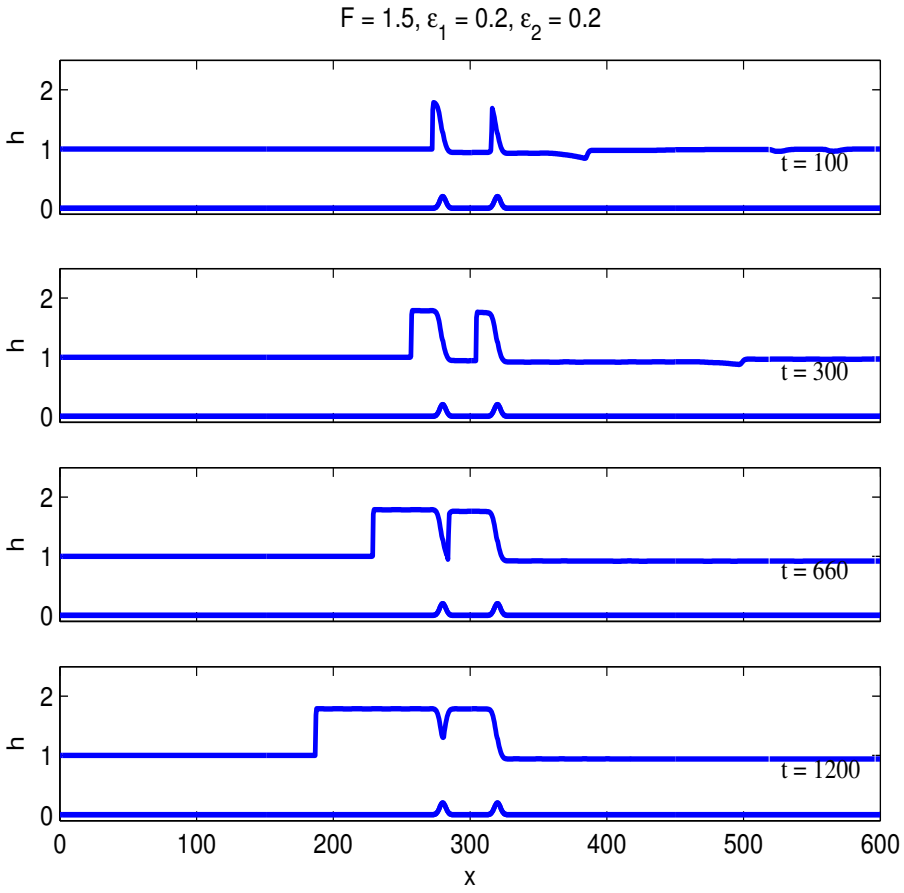

Figure 3.11: Simulations for $F = 1.5, \epsilon_1 = 0.2, \epsilon_2 = 0.2$.

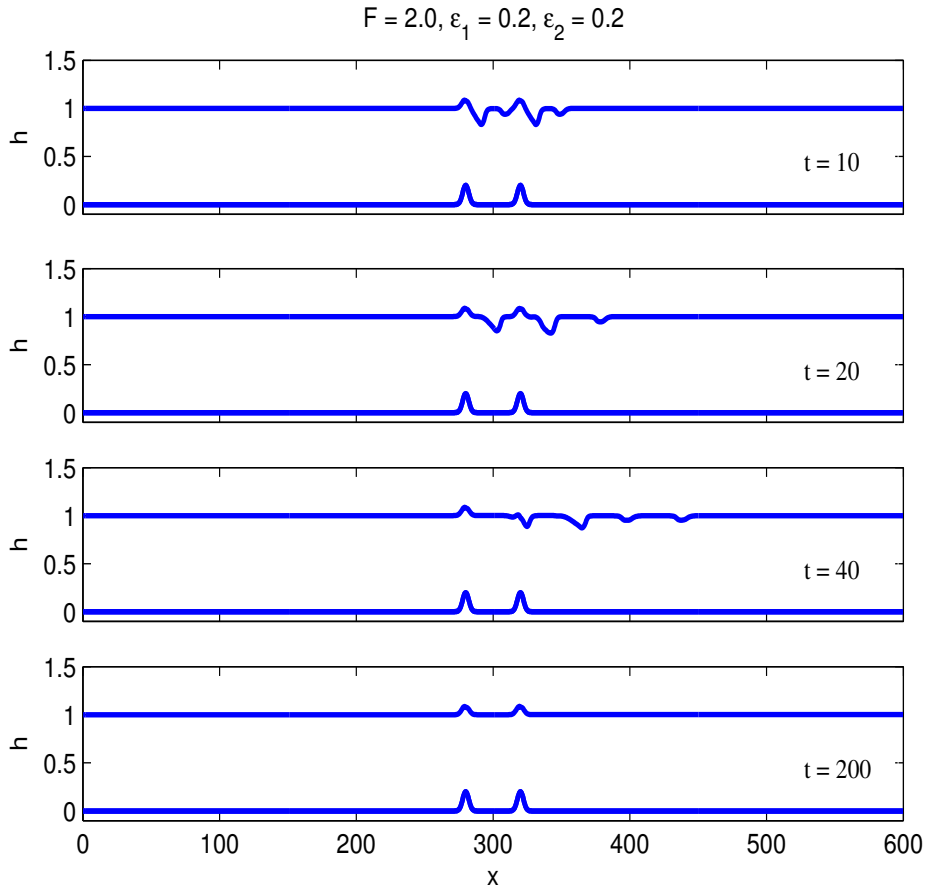

Figure 3.12: Simulations for $F = 2.0, \epsilon_1 = 0.2, \epsilon_2 = 0.2$.

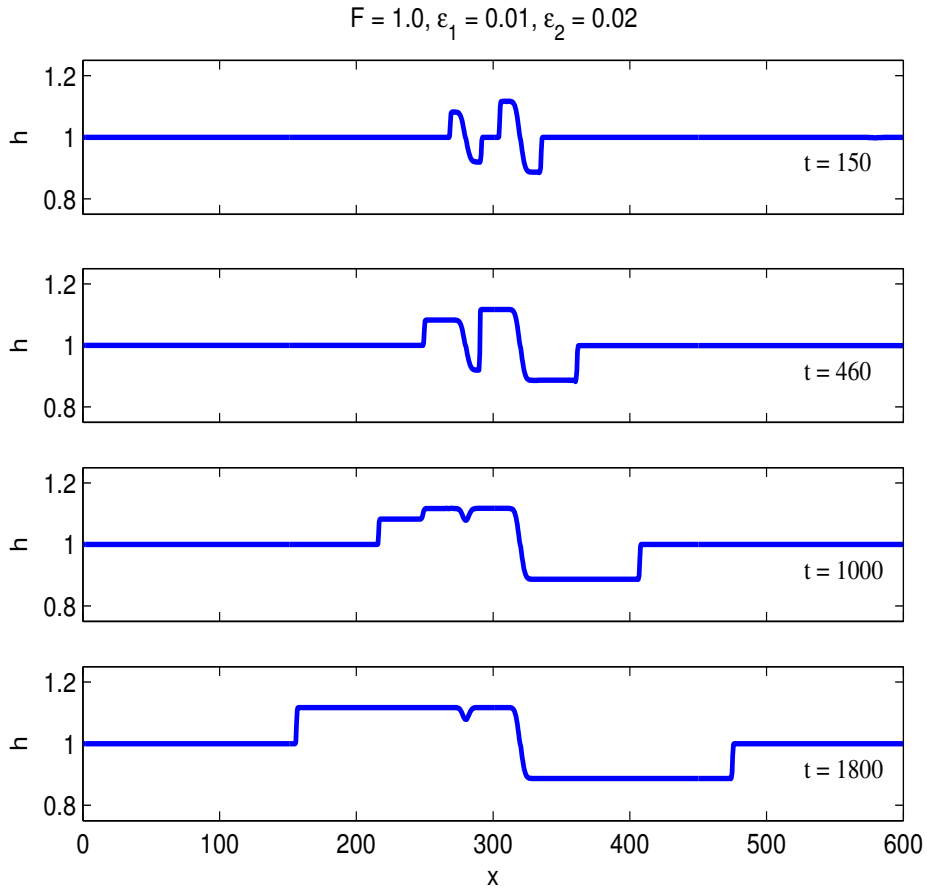

Figure 3.13: Simulations for $F = 1.0, \epsilon_1 = 0.01, \epsilon_2 = 0.02$.

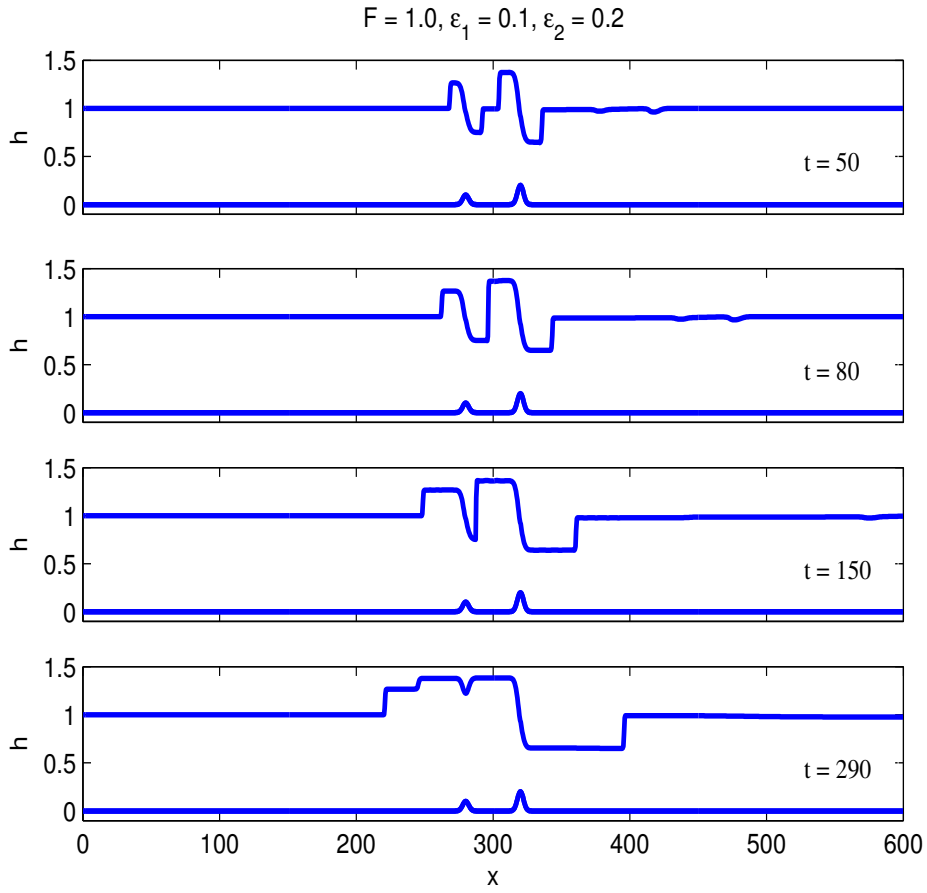

Figure 3.14: Simulations for $F = 1.0, \epsilon_1 = 0.1, \epsilon_2 = 0.2$.

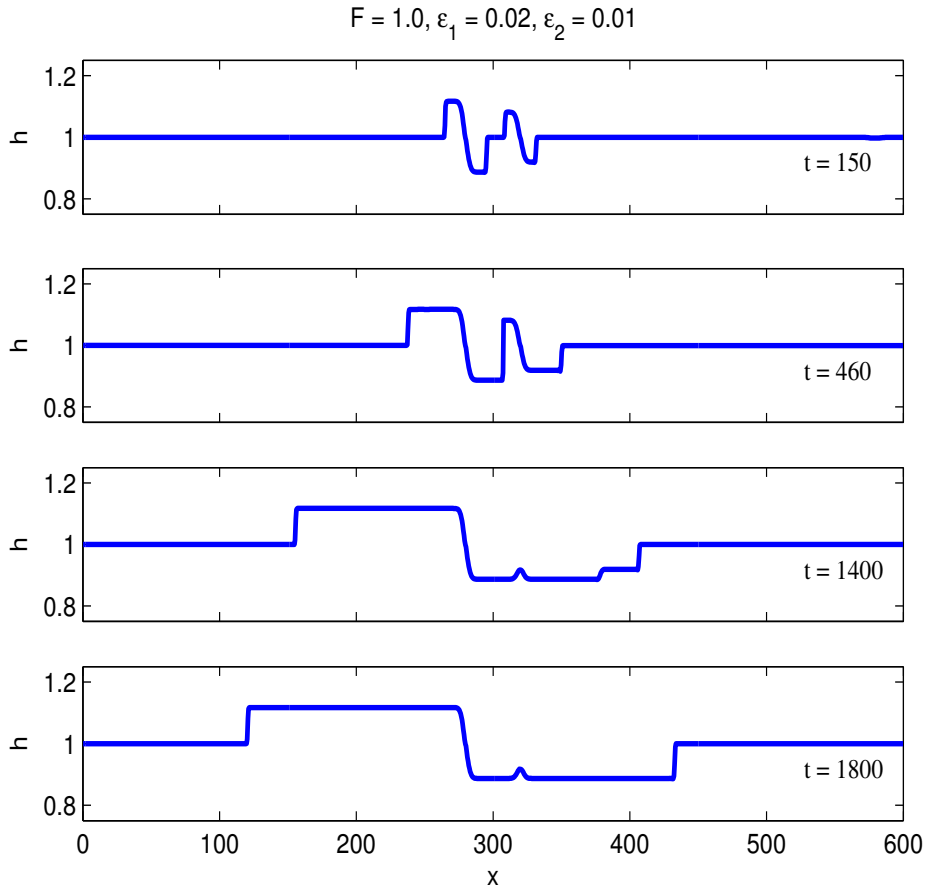

Figure 3.15: Simulations for $F = 1.0, \epsilon_1 = 0.02, \epsilon_2 = 0.01$.

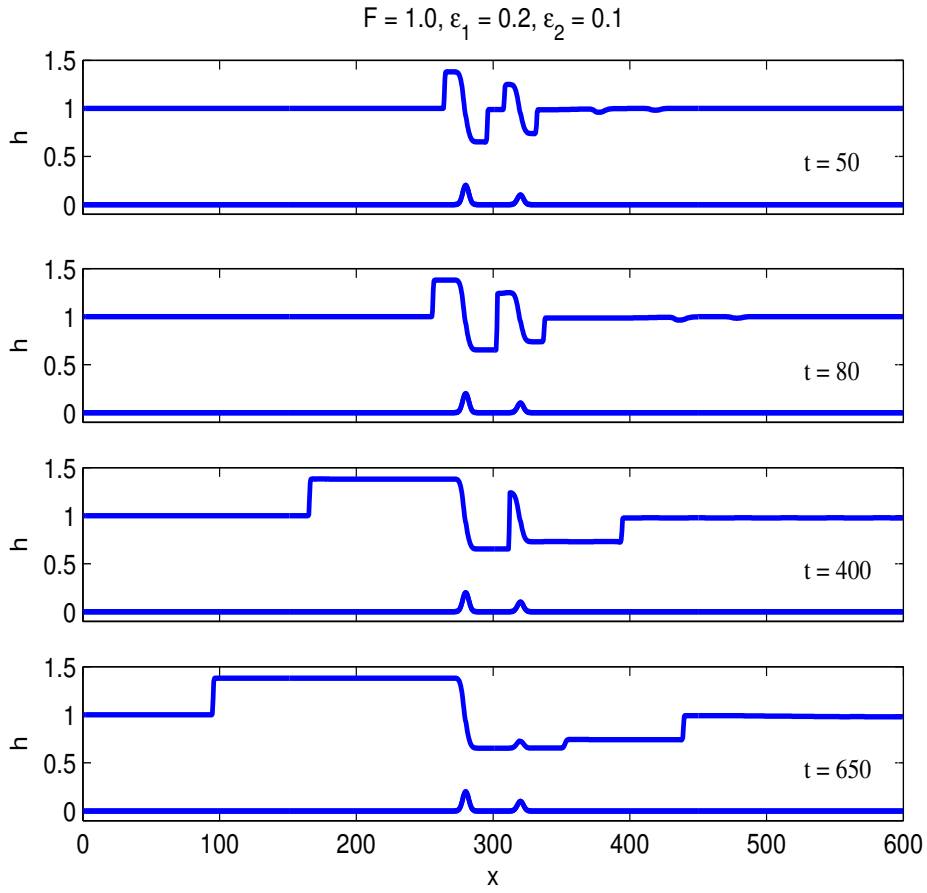

Figure 3.16: Simulations for $F = 1.0, \epsilon_1 = 0.2$, and $\epsilon_2 = 0.1$.

Chapter 4

Transcritical flow over two obstacles: forced Korteweg-de Vries framework

4.1 Introduction

The flow of a homogeneous fluid over an obstacle is a fundamental problem in fluid mechanics and has been heavily studied from many points of view. A widely used approach for shallow fluids is the application of hydraulic concepts when the flow can be classified in terms of the upstream Froude number $F = U/c$, where U is the uniform upstream flow and $c = (gh)^{1/2}$ is the linear long wave speed in water with an undisturbed depth h. The flow is then supercritical, subcritical or transcritical depending on whether $F > 1$, $F < 1$ or $F \approx 1$, see for instance the monograph by Baines (1995). In the supercritical case waves generated by the flow interaction with the obstacle propagate downstream away from the obstacle, and the flow at the obstacle location is a locally steady elevation. In the subcritical case, waves propagate upstream and downstream away from the obstacle, and the flow at the obstacle location is a locally steady depression accompanied by a steady lee waves downstream of the obstacle. Both these cases can be well understood qualitatively using linearised theory.

However, linearized theory fails in the transcritical regime, and then nonlinear shallow water theory leads to the determination of a locally steady hydraulic flow over the obstacle, with an upstream elevation and a down-

stream depression, each terminated by upstream and downstream propagating shocks. In the presence of wave dispersion, these shocks are resolved by undular bores. In the weakly nonlinear long wave regime the forced Korteweg-de Vries (KdV) equation has been invoked to describe this flow, see Akylas (1984), Cole (1985), Grimshaw and Smyth (1986), Lee et al. (1989), Binder et al. (2006), Grimshaw et al. (2007) and the recent review by Grimshaw (2010). Various aspects of the extension to finite amplitudes in the long wave regime can be found in El et al. (2006), El et al. (2008), and El et al. (2009).

Although transcritical shallow water flow is now quite well understood for a single localised obstacle, there have been comparatively very few studies of the analogous case when the there are two widely separated localised obstacles. This motivated us to examine this case in our recent work, Grimshaw and Maleewong (2015), where in the context of the nonlinear shallow water equations, we showed that the flow evolved in two stages. The first stage is the generation of an upstream elevation shock and a downstream depression shock at each obstacle alone, isolated from the other obstacle. The second stage is the interaction of these two shocks between the two obstacles, followed by an adjustment to a hydraulic flow over both obstacles, with criticality being controlled by the higher of the two obstacles, and by the second obstacle when they have equal heights. This hydraulic flow is terminated by an elevation shock propagating upstream of the first obstacle and a depression shock propagating downstream of the second obstacle. That study, although fully nonlinear, was in the context of the nonlinear shallow water equations which contain no wave dispersion.

The primary purpose of this present paper is to remedy that, and so here we examine the flow over two localized obstacles in the context of the forced Korteweg-de Vries equation, which contains a balance between weak nonlinearity, weak dispersion and small-amplitude forcing. The essential new feature is then that the generated shocks are replaced by undular bores, that is nonlinear wavetrains, and then the main question is how the undular bores, generated between the obstacles, interact. Earlier Pratt (1984) used a combination of steady hydraulic theory, numerical simulations of the nonlinear shallow water equations and laboratory experiments to infer that the formation of dispersive waves between the obstacles is needed to obtain a stable solution. More recently Dias and Vanden-Broeck (2004), Ee et al. (2010, 2011) have examined the possible presence of such waves for steady flows, while Grimshaw et al. (2009) considered the related problem of unsteady

flow over a wide hole. Our emphasis is on the transcritical regime for two widely-spaced localised obstacles. The forced Korteweg-de Vries equation is described in section 2 and numerical solutions presented in section 3. We conclude in section 4.

4.2 Forced Korteweg-de Vries equation

The forced Korteweg-de Vries (KdV) equation has been derived for water waves by Akylas (1984), Cole (1985) and Lee et al. (1989), and for internal waves by Grimshaw and Smyth (1986), see also the recent review by Grimshaw (2010). It is technically valid in the transcritical regime when $F \approx 1$, and in non-dimensional units based on a length scale h and a time scale $(h/g)^{1/2}$, it is given by

$$-\zeta_t - \Delta\zeta_x + \frac{3}{2}\zeta\zeta_x + \frac{1}{6}\zeta_{xxx} + \frac{f_x}{2} = 0\,, \quad \Delta = F - 1\,. \tag{4.1}$$

Here ζ is the free surface displacement above the free surface. The initial condition is

$$\zeta = 0\,, \quad \text{at} \quad t = 0\,. \tag{4.2}$$

It is based on the usual KdV balance where $\zeta \sim \alpha^2$, $\partial/\partial x \sim \alpha$, $\partial/\partial t \sim \alpha^3$, $\Delta \sim \alpha^2$ and $f \sim \alpha^4$ where $\alpha \ll 1$ is the governing small parameter.

For a single localized obstacle, that is $f(x)$ has a maximum height $\epsilon_m > 0$ at $x = 0$ say, and has effectively compact support such as a Gaussian, the transcritical problem can be solved asymptotically in two parts, see Grimshaw and Smyth (1986) and the review by Grimshaw (2010). In the first part, the linear dispersive term ζ_{xxx} is omitted, and the resulting forced Hopf equation can be exactly solved using characteristics,

$$\frac{dx}{dt} = \Delta - \frac{3\zeta}{2}\,, \quad \frac{d\zeta}{dt} = \frac{f_x}{2}\,. \tag{4.3}$$

With the initial condition (4.2), this can be readily integrated explicitly. When characteristics intersect, a shock forms and must satisfy the shock condition

$$(S - \Delta)[\zeta] + \frac{3}{4}[\zeta^2] = 0\,, \tag{4.4}$$

where $[\cdot]$ is the jump across the shock and S is the shock speed. Our main interest is in the transcritical regime defined here by

$$2\Delta^2 < 3\epsilon_m\,, \tag{4.5}$$

when such shocks form upstream and downstream of the obstacle. Omitting details the outcome is that a localised steady solution, sometimes called the hydraulic solution, forms over the obstacle, given by

$$4\Delta^2 - 12\Delta\zeta + 9\zeta^2 = \text{constant} - 6f(x)\,, \tag{4.6}$$

$$\text{and so} \qquad 3\zeta = 2\Delta \mp \text{sign}[x]\{6[\epsilon_m - f(x)]\}^{1/2}\,. \tag{4.7}$$

Here equation (4.6) can readily by direct integration of the Hopf equation obtained from the steady version of (4.1) after omitting the linear dispersive term. The constant of integration is determined by the hydraulic condition that $\zeta_x \neq 0$ at the top of the obstacle, where then $\zeta = 2\Delta/3$ and the constant takes the value $6\epsilon_m$. This is terminated by upstream and downstream shocks with magnitude $\zeta_\mp$,

$$3\zeta_\mp = 2\Delta \pm \{6\epsilon_m\}^{1/2}\,. \tag{4.8}$$

Note that $\zeta_+ < 0, \zeta_- > 0$ so that the upstream shock is elevation and the downstream shock is depression. The speeds of these shocks are found from (4.4), that is

$$4S_\mp = 3\zeta_\mp = 2\Delta \mp \{6\epsilon_m\}^{1/2}\,, \tag{4.9}$$

and $S_- < 0, S_+ > 0$. Outside the transcritical regime, when $\Delta > (3\epsilon_m/2)^{1/2}$ the flow is supercritical, and all characteristics propagate downstream, leaving a steady elevation over the obstacle, while when $\Delta < -(3\epsilon_m/2)^{1/2}$ the flow is subcritical, and all characteristics propagate upstream, leaving a steady depression over the obstacle. In this subcritical case, when dispersion is restored, stationary lee waves will form behind the obstacle.

In the second part, the shocks are replaced by undular bores using the Gurevich-Pitaeveskii adaptation, see Gurevich and Pitaevskii (1974), of the Whitham modulation theory, Fornberg and Whitham (1978); Whitham (1965, 1974). A brief summary of that theory is reproduced here in the Appendix, adapted from Grimshaw (2010). The undular bore in $x < 0$ is described by (4.21) to (4.24) with $\zeta_0 = \zeta_-$. Hence it occupies the zone

$$\Delta - \zeta_- < \frac{x}{t} < \max\{0,\ \Delta + \frac{3\zeta_-}{2}\}\,. \tag{4.10}$$

Note that this upstream wavetrain is constrained to lie in $x < 0$, and hence is only fully realised if $\Delta < -3\zeta_-/2$. Combining this criterion with (4.5) and (4.8) defines the regime

$$-(\frac{3\epsilon_m}{2})^{1/2} < \Delta < -\frac{1}{2}(\frac{3\epsilon_m}{2})^{1/2}\,, \tag{4.11}$$

where a fully developed undular bore solution can develop upstream. On the other hand, the regime $\Delta > -3\zeta_-/2$ or

$$-\frac{1}{2}(\frac{3\epsilon_m}{2})^{1/2} < \Delta < (\frac{3\epsilon_m}{2})^{1/2}\,, \tag{4.12}$$

is where the upstream undular bore is only partially formed, and is attached to the obstacle. In this case the modulus m of the Jacobi elliptic function varies from 1 at the leading edge (thus describing solitary waves of amplitude $2\zeta_-$) to a value m_- (< 1) at the obstacle, where m_- can be found by putting $x = 0$ in (4.23).

The undular bore in $x > 0$ can also be described by (4.21) to (4.24) with $\zeta_0 = -A_+$, after using the transformation (4.26). Hence it occupies the zone

$$\max\left\{0,\ \Delta - \frac{\zeta_+}{2}\right\} < \frac{x}{t} < \Delta - 3\zeta_+\,. \tag{4.13}$$

Here, this downstream wavetrain is constrained to lie in $x > 0$, and hence is only fully realised if $\Delta > \zeta_+/2$, and then the leading solitary wave has an amplitude $-2\zeta_+$. Combining this criterion with (4.5) and (4.8) defines the regime (4.12), and so a fully detached downstream undular bore coincides with the case when the upstream undular bore is attached to the obstacle. On the other hand, in the regime (4.11), when the upstream undular bore is detached from the obstacle, the downstream undular bore is attached to the obstacle, with a modulus $m_+(< 1)$ at the obstacle, where m_+ can again be found from the counterpart of (4.23) evaluated at $x = 0$.

When there are two widely placed obstacles with maximum heights $\epsilon_{1,2}$ respectively, there are several regimes to consider depending on Δ and $\epsilon_{1,2}$. The main regime is when the flow is transcritical at each obstacle separately, that is $\Delta^2 < \min[\epsilon_1, \epsilon_2]$. and then the solution evolves in three stages. In the first stage, this local steady solution with upstream and downstream undular bores holds for each obstacle separately. But when there are two obstacles, in the second stage the upstream elevation undular bore from the second obstacle will meet the downstream depression undular bore from the first obstacle. These interact and possibly then also modulate the upstream elevation undular bore from the first obstacle and the downstream depression undular bore from the first obstacle. Our main purpose here is to determine the outcome of that interaction. The third stage is when the solution appears to settle outside each obstacle, but with continuing wave interactions between the obstacles.

We note that in this third stage a localised steady solution can be found given again by (4.7) but with ϵ replaced by $\max[\epsilon_{1,2}]$. That is, a hydraulic solution controlled by the larger of the two obstacles. This was the outcome found by Grimshaw and Maleewong (2015) in the fully nonlinear non-dispersive case. The smaller of the obstacles is then in either a locally supercritcal flow, or a locally subcritical flow, depending on whether it is the second or the first obstacle. This is shown by noting that relative to a level ζ_0, Δ in (4.1) is replaced by $\Delta' = \Delta - 3\zeta_0/2$. Thus if $\epsilon_1 > \epsilon_2$, put $\zeta_0 = \zeta_+$ and then $\Delta' = (3\epsilon_1/2)^{1/2} > (3\epsilon_2/2)^{1/2}$ and so the flow is supercritical at the second obstacle. Alternatively if $\epsilon_2 > \epsilon_1$, put $\zeta_0 = \zeta_-$ and then $\Delta' = -(3\epsilon_2/2)^{1/2} < -(3\epsilon_1/2)^{1/2}$ and so the flow is subcritical at the first obstacle. When the obstacles have equal heights, $\epsilon_1 = \epsilon_2$, Grimshaw and Maleewong (2015) found that this local hydraulic solution could be found with critical control exerted at the second obstacle and a contact discontinuity at the first obstacle. However that conclusion was based on higher order nonlinear effects beyond the regime of the fKdV equation (4.1), and so cannot be assumed to hold here. Instead we find that in this case of obstacles of equal heights, either obstacle can exert critical control depending on the value of Δ. The numerical simulations reported in section 3 suggest that when $-(3\epsilon_1/2)^{1/2}/2 < \Delta < (3\epsilon_1/2)^{1/2}$ so that the upstream undular bore is attached to each obstacle, while the downstream undular bore is detached, then it is the first obstacle which exerts control, since then the downstream undular bore will eventually pass over the second obstacle, leaving a supercritical flow there, although there may still be continuing wave activity between the obstacles. On the other hand when $-(3\epsilon_1/2)^{1/2} < \Delta < -(3\epsilon_1/2)^{1/2}/2$ so that the downstream undular bore is attached to each obstacle, while the upstream undular bore is detached, then it is the second obstacle which exerts control, since then the upstream undular bore will eventually pass over the first obstacle, leaving a subcritical flow there, although again there may still be continuing wave activity between the obstacles.

4.3 Numerical simulations

4.3.1 Pseudospectral method

The forced Korteweg-de Vries (fKdV) in (4.1) with initial condition (4.2) is solved numerically by the pseudo spectral method. The computational

domain is $-L < x < L$, with $L = 8192$. The forcing $f(x)$ is composed of two obstacles given by

$$f(x) = \epsilon_1 \exp\left(-(x - x_a)^2/w\right) + \epsilon_2 \exp\left(-(x - x_b)^2/w\right) , \tag{4.14}$$

where ϵ_1 and ϵ_2 are the obstacle heights, and x_a and x_b are the obstacle locations, respectively. Here we set $x_a = -2050$ and $x_b = -2000$. The obstacle width is $w = 50$.

Since the boundary conditions are periodic, we set a sponge layer in (4.1) by inserting a sponge term, $s(x)$, to absorb small waves approaching the boundaries,

$$-\zeta_t - \Delta\zeta_x + \frac{3}{4}{\zeta_x}^2 + \frac{1}{6}\zeta_{xxx} + \frac{f_x}{2} - s(x)\zeta = 0 \,, \tag{4.15}$$

$$s(x) = \frac{\nu}{2}\Big[\{1 + \tanh(\kappa(x - K/2))\}\{1 - \tanh(\kappa(x + K/2))\}\Big] . \tag{4.16}$$

Here we set $\nu = 5$, $\kappa = 0.002$, and $K = 7750$.

The fKdV equation (4.1) is solved numerically using a combination of a finite different method in time and a Fourier pseudospectral method in space. That is, we write (4.15) as

$$\zeta_{\hat{t}} = M(\zeta) = -\Delta\,\zeta_{\hat{x}} + \frac{3}{4}{\zeta_{\hat{x}}}^2 + \frac{1}{6}\,\zeta_{\hat{x}\hat{x}\hat{x}} + \frac{1}{2}\,f_{\hat{x}} - s(\hat{x})\zeta \,. \tag{4.17}$$

Then we apply the forth-order Runge-Kutta method,

$$\zeta^{n+1} = \zeta^n + \frac{1}{6}\{M_1 + 2M_2 + 2M_3 + M_4\} \,,$$

where

$$M_1 = M(\zeta^n) \,, M_2 = M(\zeta^n + M_1/2) \,, M_3 = M(\zeta^n + M_2/2) \,, \text{and } \; M_4 = M(\zeta^n + M_3) \,.$$

Superscript n refers to the time step. Then the spatial terms are evaluated by a pseudospectral method. We introduce the approximate solution

$$\zeta(\hat{x}, \hat{t}) = \sum_{k=-N}^{N} a_k(\hat{t})\Phi_k(\hat{x}) \,, \tag{4.18}$$

where $\Phi_k(\hat{x}) = \exp(ik\hat{x})$ are the Fourier exponentials, and $a_k(\hat{t})$ are the coefficients to be determined; note that $a_{-k} = \bar{a_k}$ on order to keep ζ real-valued.

Let ζ_j^n denotes the value of ζ at grid point $\hat{x}_j$ and time $\hat{t}^n$. To find ζ_j^{n+1}, we summarize the main steps as follows.

(1) Given $\zeta_j^n = \zeta(\hat{x}_j, \hat{t}_n)$, we evaluate $a_k^n = a_k(\hat{t}_n)$ from (4.18) using a Fast Fourier Transform (FFT) algorithm. The derivatives of the linear terms are calculated in the spectral space.

(2) The nonlinear term is found similarly, that is, we get $\zeta(\hat{x}_j, \hat{t}_n)$ at each grid point $\hat{x}_j$, then find $\zeta(\hat{x}_j, \hat{t}_n)^2$ in the physical space.

(3) Given Δ, and the shape of obstacles $f(\hat{x})$, we can calculate ζ_j^{n+1} from (4.17) at $\hat{x} = \hat{x}_j$ and $\hat{t} = \hat{t}_{n+1}$.

4.3.2 Equal obstacle heights ($\epsilon_1 = 0.1, \epsilon_2 = 0.1$)

In figure 4.1, we show the case at exact crticality when $F = 1, \Delta = 0$. Here the predicted values of $\zeta_\pm = \mp 0.26$, see (4.8) and so the leading solitary waves will have predicted amplitudes of 0.52 As indicated above, the flow development takes place in three stages. In the first stage, in a short time period from the start, undular bores are generated from each obstacle moving upstream and downstream, see the time $t = 60$. The second stage is the the interaction between the downstream undular bore from the first obstacle and the upstream undular bore from the second obstacle, see the time $t = 160$ and the region indicated by a double arrow. Note that the amplitude of these waves between the obstacles is approximately twice the value 0.52 of the largest waves from each separate undular bore. At the same time, the upstream undular bore generated from the first obstacle continues moving upstream, and the downstream undular bore generated from the second obstacle continue moving downstream. As time increases, the downstream undular bore generated by the second obstacle moves far away from the obstacle. Then the downstream flow is supercritical at the second obstacle, see the times $t = 440, 1920$. The simulation is then continued for a very long time to monitor the wave interaction between the two obstacles, see the time $t = 7600$. The amplitudes of the interacting waves between the two obstacles are not diminishing. This is referred to as the third stage. In the whole domain, there are upstream, intermediate, and downstream zones, and overall the flow resembles a transcritical flow generated by the first obstacle where

there is an attached undular bore upstream, a depressed zone downstream connected with undular bore very far downstream, and locally a supercritical flow over the second obstacle. But, importantly there is a wave interaction zone between the obstacles, which appears to remain transient without any diminishing amplitude.

In figure 4.2 we show the case when $F = 1.2, \Delta = 0.2$. The transition boundaries $\pm(3\epsilon_1/2)^{1/2} = \pm 0.39$, and so this flow is transcritical and in the same regime (4.12) as $F = 1, \Delta = 0$. But now $\zeta_\pm = -0.125, 0.39$, see (4.8), and so the leading solitary waves will have predicted amplitudes of $0.25, 0.78$ respectively. Overall the flow develops in a similar manner and the first stage can be seen at $t = 60, 160$, rather longer than for the case $\Delta = 0$. The second has already begun at $t = 160$ and is clearly apparent at $t = 440$, which is also the beginning of the third stage, seen at the times , $t = 1920, 6580$. In this case, the number of waves between the two obstacles is smaller than for the case of $F = 1.0$, but the wave amplitudes are similar, and approximately equal to the sum of the largest waves from each separate undular bore, that is $2(\zeta_- - \zeta_+) = 2\{6\epsilon\}^{1/2}/3 = 1.03$. Also note that the undular bore upstream of the first obstacle is modulated by the large waves between the obstacles, compare the rather uniform structure at $t = 1920$ with those at $t = 440, 6580$.

The case of $F = 1.35, \Delta = 0.35$ shown in figure 4.3 is interesting. This value of the Froude number is almost on the boundary of the transition from transcritical flow to fully supercritical flow which occurs at $\Delta = \{3\epsilon/2\}^{1/2} = 0.39$. Also now $\zeta_\pm = -0.025, 0.49$, see (4.8), and so the leading solitary waves will have predicted amplitudes of $0.05, 0.98$ respectively. Th first stage takes longer to develop and at the first obstacle only becomes fully apparent at $t = 210$. However, it seems that this stage is suppressed at the second obstacle, presumably because the downstream undular bore from the first obstacle, has already passed over the second obstacle, see at $t = 120, 210$. The second stage is not seen, as no waves are discernible between the two obstacles. Instead the third stage emerges at $t = 450, 5010$ and well-separated solitary waves are emitted from the first obstacle, while there is a local supercritical flow over the second obstacle.

The case of $F = 1.4, \Delta = 0.4$ is a supercritical flow and shown in figure 4.4. At the very early stage, downstream waves generated by the first obstacle can flow past the localised elevation wave produced by the second obstacle. Then, as transient waves propagate rapidly downstream, a locally steady supercritical flow forms over each obstacle.

Next we show the case of $F = 0.8, \Delta = -0.2$ in figure 4.5. As before

$(3\epsilon_1/2)^{1/2} = 0.39$, and so this flow is transcritical, but lies in the subcritical regime (4.11), when the upstream undular bore from each obstacle is detached, and the downstream undular bore from each obstacle is attached. Now $\zeta_\pm = -0.39, 0.125$, see (4.8), and so the leading solitary waves will have predicted amplitudes of $0.78, 0.5$ respectively. This is clearly seen in the first stage at $t = 60$. The second stage has begun at $t = 100$ and is clearly seen at $t = 520$. In the third stage, critical control is at the second obstacle, see $t = 1000, 5400$. There is a strong continuing wave interaction between the obstacles while there is a well-developed undular bore, attached to the second obstacle, and a subcritical flow over the first obstacle, where the downstream generated lee waves are interacting with the upstream propagating undular bore.

The case of $F = 0.6, \Delta = -0.4$ is a subcritical flow and is shown in figure 4.6, where $\Delta < -\{3\epsilon/2\}^{1/2} = -0.39$. However, this flow is very close to this regime boundary, and hence there is some similarity with the case $F = 0.8, \Delta = -0.2$, although the wave amplitudes are noticeably smaller. From $t = 40, 80, 180$ we see the development of an upstream transient and lee wave formation downstream. At $t = 600, 6500$ the waves between the obstacles are irregular and largely suppressed, while a stationary lee wave train has formed downstream of the second obstacle.

The case of $F = 0.4, \Delta = -0.6$ is also a subcritical flow, and shown in figure 4.7. Compared to the case when $F = 0.6, \Delta = -0.4$, the lee waves are greatly suppressed, and at the final stage $t = 4600$, there are two depression waves over each obstacle, with no waves visible between the obstacles.

4.3.3 Unequal obstacle heights $(\epsilon_1 = 0.1, \epsilon_2 = 0.2)$

Here we consider the case when $\epsilon_1 = 0.1, \epsilon_2 = 0.2$ so that the second obstacle is larger in amplitude. The case of exact criticality $F = 1.0, \Delta = 0$ in shown in figure 4.8. The outcome is similar to the case of equal obstacle heights at exact criticality, shown in figure 4.1. The flow development takes place in three stages. In the first stage, undular bores are generated from each obstacle moving upstream and downstream, see the time $t = 80$. The second stage is the interaction between the downstream undular bore from the first obstacle and the upstream undular bore from the second obstacle, see the time $t = 180$ and the region indicated by a double arrow. The upstream undular bore generated from the first obstacle continues moving upstream, and the downstream undular bore generated from the second obstacle con-

tinues moving downstream. As time increases, the downstream undular bore generated by the second obstacle moves far away from the obstacle. In the third stage, the downstream flow is supercritical at the second obstacle which has the larger height, see the times $t = 480, 6360$. Upstream of the first obstacle the flow is subcritical with a modulated undular bore attached to this first obstacle. Between the two obstacles there are interacting waves whose amplitudes are not decreasing, and remain unsteady.

In figure 4.9 we show the case when $F = 1.2, \Delta = 0.2$. The transition boundaries for the first obstacle are $\pm(3\epsilon_1/2)^{1/2} = \pm 0.39$ and $\pm(3\epsilon_2/2)^{1/2} = \pm 0.55$ for the second obstacle, and so this flow is transcritical for both obstacles. Overall the flow develops in a similar manner to that described above for $F = 1$ in figure 4.2, and the first stage can be seen at $t = 20, 80$. The second stage has already begun at $t = 160$. The beginning of the third stage can be seen at the times $t = 3000$. For the long run, $t = 5900$, the undular bore upstream of the first obstacle is modulated by the waves between the obstacles.

The case when $F = 1.4, \Delta = 0.4$ is shown in figure 4.10. Now while the first obstacle is locally in a supercritical regime. $\Delta = 0.4 > (3\epsilon_1/2)^{1/2} = 0.39$, the second obstacle is still locally in the transcritical regime, $\Delta = 0.4 < (3\epsilon_2)^{1/2} = 0.55$. This differs from the corresponding case for equal obstacle heights shown in figure 4.4. At the early times $t = 80, 120$ we see a locally steady supercritical flow over the first obstacle, while large-amplitude elevation waves generated by the second obstacle propagate upstream towards the first obstacle, and a weak undular bore propagates downstream. The upstream-propagating elevation waves continually generated at the second obstacle pass over the first obstacle and continue upstream.

The case when $F = 0.8, \Delta = -0.2$ is shown in figure 4.11. This flow is in the transcritical regime for both obstacles. But, the first obstacle is just below the regime boundary where the upstream undular bore is fully detached and the downstream undular bore is attached, that is $-(3\epsilon_1/2)^{1/2} = -0.39 < \Delta = -0.2 < -(3\epsilon_1/2)^{1/2}/2 = -0.19$, while the second obstacle is above this boundary, that is $-(3\epsilon_2/2)^{1/2} = -0.55 < \Delta = -0.2 < (3\epsilon_2/2)^{1/2} = 0.55$ and so the upstream undular bore is attached to the obstacle, while the downstream undular bore is detached. These features are apparent in the first stage, $t = 40$. In the second stage, $t = 60, 160$ there is an interaction between the downstream undular bore from the first obstacle and the upstream undular bore from the second obstacle, similar to the case of equal obstacle heights shown in figure 4.5. However, the third stage, $t = 740, 7400$, is differ-

ent since there is little sign of a depression behind the first obstacle. Critical control is exerted by the second obstacle. There is continuing wave interaction bewteen the obstacles, which modulates the undular bore propagating upstream of the first obstacle.

The case of $F = 0.6, \Delta = -0.4$ is shown in figure 4.12. This flow is subcritical for the first obstacle as $\Delta = -0.4 < -(3\epsilon_1/2)^{1/2} = -0.39$ but is transcritical for the second obstacle in the regime when the upstream undular bore is detached and the downstream undular is detached, $-(3\epsilon_2/2)^{1/2} = -0.55 < \Delta = -0.4 < -(3\epsilon_2)^{1/2}/2 = -0.27$. Overall the stages are similar to the case of equal obstacle heights shown in figure 4.6 except that the amplitude of the downstream undular bore downstream is larger due to the larger obstacle amplitude.

The case of $F = 0.4, \Delta = -0.6$ is shown in figure 4.13. This flow is fully subcritical for both obstacles and is similar to the case of equal obstacle heights shown in figure 4.7.

4.3.4 Unequal obstacle heights ($\epsilon_1 = 0.1, \epsilon_2 = 0.05$)

The case of $\epsilon_1 = 0.1, \epsilon_2 = 0.05$ for $F = 1.0, \Delta = 0$ is shown in figure 4.14, the second obstacle height is now smaller than the first obstacle height. The first two stages are similar to the case of equal obstacle height shown in figure 4.1. However as the third stage is approached , there is only a single wave between the obstacles at $t = 5920$ and this wave then moves downstream over the second obstacle and passes very far downstream. Thus, there are eventually no waves between the obstacles and the flow is supercritical over the second obstacle.

The case of $F = 1.2, \Delta = 0.2$ is shown in figure 4.15. This flow is transcritical for both obstacles, $\Delta = 0.2 < (3\epsilon_2/2)^{1/2} = 0.27 < (3\epsilon_1/2)^{1/2} = 0.39$. This is similar to the case of $F = 1.0$ above in figure 4.14, but evolves faster as the supercritical flow over the second obstacle occurs at time $t = 1360$. Again this third stage differs from that for equal obstacle heights show in figure 4.2.

The case of $F = 1.4, \Delta = 0.4$ is shown in figure 4.16. This flow is supercritical for both obstacles, $\Delta = 0.4 > (3\epsilon_1/2)^{1/2} = 0.39 > (3\epsilon_2/2)^{1/2} = 0.27$. The flow is fully developed supercritical flows over the obstacles, similar to that for equal obstacles shown in figure 4.4.

The case of $F = 0.8, \Delta = -0.2$ is shown in figure 4.17. This flow is transcritical for the both obstacles, and both obstacles are in the regime

when the upstream undular bore is attached and the downstream undular bore is detached, $-(3\epsilon_1/2)^{1/2} = -0.39 < \Delta = -0.2 < (3\epsilon_1/2)^{1/2}/2 = -0.19$ and $-(3\epsilon_2/2)^{1/2} = -0.27 < \Delta = -0.2 < (3\epsilon_1/2)^{1/2}/2 = -0.14$. The first two stages are similar to the case of equal obstacle heights shown in figure 4.5. But the third stage is different as now the waves between the obstacles can eventually disappear, leaving a locally supercritical flow over the first obstacle terminated by an upstream propagating undular bore (see $t = 200$) but is far upstream at $t = 2540, 7780$, and an attached undulat bore downstream of the second obstacle.

The case of $F = 0.6, \Delta = -0.4$ is shown in figure 4.18. This flow is subcritical for both obstacles, $\Delta = -0.4 < -(3\epsilon_1/2)^{1/2} = -0.39 < -(3\epsilon_2/2)^{1/2} = -0.27$. The first two stages are similar to the case of equal obstacles shown in figure 4.6. But at the third stage, steady lee waves form behind both obstacles and a small depression can be seen behind the first obstacle.

The case of $F = 0.4, \Delta = -0.6$ shown in figure 4.19 and is also fully subcritical for both obstacles. This case is similar to that for equal obstacle heights shown in figure 4.7 and the flow develops rapidly into locally steady subcritical flow over both obstacles.

4.4 Summary

Free-surface flows over two obstacles are studied in this work. Our objective is to analyse and simulate free-surface flow in transcritical regime. The flow can be characterised by Δ, $\Delta = F - 1$ where F is the Froude number. Our main concern is $F \approx 1$, so, the forced Korteweg-de Vrise is the main framework in this work. For flow over two compactly support obstacles, flow behaviours can be characterised by Δ, and the maximum heights of obstacles (ϵ_1 and ϵ_2). When the initial condition is flat surface, we assume both obstacles suddenly perturb the free surface. In transcritical regime, undular bores are produced on upstream and downstream of each obstacle. Our interest is to study the interaction of these undular bores between the obstacles. To arrive these, we apply Whitham modulation theory for single obstacle to classify flow fields and behaviours. We then apply the single obstacle results to explain the case of two obstacles. Here we define flow characteristics in three stages for flow over two obstacles. The first stage can be described by single obstacle results with Whitham modulation theory. The second stage is the interaction

between moving waves downstream from the first obstacle and moving waves upstream from the second obstacle. The final stage is the very large time and the question becomes that which the first or the second obstacle has controlled the flow. Our analytical results indicate that the criticality is controlled under the relationships of ϵ_1, ϵ_2 and Δ. For equal obstacle heights, when $-(3\epsilon_1/2)^{1/2}/2 < \Delta < (3\epsilon_1/2)^{1/2}$ the first obstacle controls the flow. On the other hand, when $-(3\epsilon_1/2)^{1/2} < \Delta < -(3\epsilon_1/2)^{1/2}/2$, the second obstacle exerts control. These analytical results are confirmed by various cases using numerical simulations of pseudo spectral method. It is also found that these flow behaviours are differ from our recently work under fully nonlinear non-dispesive wave model such that the criticality is controlled by the second obstacle when $\epsilon_1 = \epsilon_2$, or controlled by the larger obstacle height when $\epsilon_1 \neq \epsilon_2$. But here in this work, we consider under the fKdV that includes dispersive effects. So, to understand or complete basic knowledge of this research topic is remain required much more studies in different water wave models. The extension of this work would be studying under the fully nonlinear model that may yield us some connections among water wave theories and results.

Appendix: Undular bore

We consider the unforced KdV equation where $f(x) = 0$ in (4.1),

$$-\zeta_t - \Delta\zeta_x + \frac{3}{2}\zeta\zeta_x + \frac{1}{6}\zeta_{xxx} = 0\,, \tag{4.19}$$

with the initial jump condition

$$\zeta = \zeta_0 H(x)\,, \quad \zeta_0 > 0\,. \tag{4.20}$$

Here $H(x)$ is the usual Heaviside function. Using the Whitham modulation theory, see Gurevich and Pitaevskii (1974); Fornberg and Whitham (1978); Whitham (1965, 1974). the undular bore is represented by the modulated periodic wavetrain

$$\zeta = a\{b(m) + \mathrm{cn}^2(\kappa(x - Vt); m)\} + d\,, \tag{4.21}$$

$$\text{where} \quad b = \frac{1-m}{m} - \frac{E(m)}{mK(m)}\,, \quad a = \frac{4m\kappa^2}{3}\,,$$

$$\text{and} \quad V = \Delta - \frac{3d}{2} - \frac{a}{2}\left\{\frac{2-m}{m} - \frac{3E(m)}{mK(m)}\right\}. \tag{4.22}$$

Here $\mathrm{cn}(x; m)$ is the Jacobi elliptic function of modulus m and $K(m), E(m)$ are the elliptic integrals of the first and second kind respectively. $(0 < m < 1)$, a is the wave amplitude, d is the mean level, and V is the wave speed. The spatial period is $2K(m)/\kappa$. This family of solutions contains three free parameters, which are chosen from the set $\{a, \kappa, V, d, m\}$. As $m \to 1$, $\mathrm{cn}(x; m) \to \mathrm{sech}(x)$ and then the cnoidal wave (4.21) becomes a solitary wave, riding on a background level d. On the other hand, as $m \to 0$, $\mathrm{cn}(x; m) \to \cos x$ and so the cnoidal wave (4.21) collapses to a linear sinusoidal wave of small amplitue $a \sim m$).

In the aforementioned asymptotic method in the modulated periodic wavetrain, the amplitude a, the mean level d, the speed V and the wavenumber κ are all slowly varying functions of x and t, described by a set of three nonlinear hyperbolic equations for three of the available free parameters, chosen from the set (a, κ, V, d, m). Here the relevant asymptotic solution is constructed in terms of the similarity variable x/t,

$$\Delta - \frac{x}{t} = \frac{\zeta_0}{2}\left\{1 + m - \frac{2m(1-m)K(m)}{E(m) - (1-m)K(m)}\right\}, \quad -\frac{3\zeta_0}{2} < \Delta - \frac{x}{t} < \frac{\zeta_0}{2}\,, \tag{4.23}$$

$$a = 2\zeta_0 m\,, \quad d = \zeta_0\left\{m - 1 + \frac{2E(m)}{K(m)}\right\}. \tag{4.24}$$

Ahead of the wavetrain where $x/t < \Delta - \zeta_0, \zeta = 0$ and at this end, $m \to 1$, $a \to 2\zeta_0$ and $d \to 0$; the leading wave is a solitary wave of amplitude $2\zeta_0$ relative to a mean level of 0. Behind the wavetrain where $x/t > \Delta + 3\zeta_0/2$, $\zeta = \zeta_0$ and at this end $m \to 0$, $a \to 0$, and $d \to \zeta_0$; the wavetrain is now sinusoidal with a wavenumber κ given by $\kappa^2 = 3\zeta_0/2$; indeed this holds throughout the wavetrain, so all waves have the same spatial wavelength.

The corresponding solution when the initial condition is instead

$$\zeta = -\zeta_0 H(-x)\,, \tag{4.25}$$

can be obtained from the above by the transformation

$$\tilde{\zeta} = \zeta + \zeta_0\,, \quad \tilde{x} = x - \frac{3\zeta_0}{2}t\,, \tag{4.26}$$

which transforms the initial-value problem (4.25) for ζ satisfying (4.19) into the initial-value problem (4.20) for $\tilde{\zeta}$ also satisfying (4.19).

Bibliography

Akylas, T. R. (1984). On the excitation of long nonlinear water waves by moving pressure distribution. *J. Fluid Mech.*, 141:455–466.

Baines, P. (1995). *Topographic effects in stratified flows*. CUP.

Binder, B., Dias, F., and Vanden-Broeck, J.-M. (2006). Steady free-surface flow past an uneven channel bottom. *Theor. Comp. Fluid Dyn.*, 20:125–144.

Cole, S. L. (1985). Transient waves produced by flow past a bump. *Wave Motion*, 7:579–587.

Dias, F. and Vanden-Broeck, J. M. (2004). Trapped waves between submerged obstacles. *J. Fluid Mech.*, 509:93–102.

Ee, B. K., Grimshaw, R. H. J., Chow, K. W., and Zhang, D.-H. (2011). Steady transcritical flow over a hole: Parametric map of solutions of the forced extended Korteweg-de Vries equation. *Phys. Fluids*, 23:04662.

Ee, B. K., Grimshaw, R. H. J., Zhang, D.-H., and Chow, K. W. (2010). Steady transcritical flow over an obstacle: Parametric map of solutions of the forced Korteweg-de Vries equation. *Phys. Fluids*, 22:056602.

El, G., Grimshaw, R., and Smyth, N. (2006). Unsteady undular bores in fully nonlinear shallow-water theory. *Phys. Fluids*, 18:027214.

El, G., Grimshaw, R., and Smyth, N. (2008). Asymptotic description of solitary wave trains in fully nonlinear shallow-water theory. *Physica D*, 237:2423–2435.

El, G., Grimshaw, R., and Smyth, N. (2009). Transcritical shallow-water flow past topography: finite-amplitude theory. *J. Fluid Mech.*, 640:187–214.

Fornberg, B. and Whitham, G. B. (1978). A numerical and theoretical study of certain nonlinear wave phenomena. *Phil.Trans. Royal Soc. A*, 289:373–404.

Grimshaw, R. (2010). Transcritical flow past an obstacle. *ANZIAM J.*, 52:1–25.

Grimshaw, R. and Smyth, N. (1986). Resonant flow of a stratified fluid over topography. *J. Fluid Mech.*, 169:429–464.

Grimshaw, R., Zhang, D., and Chow, K. (2007). Generation of solitary waves by trancritical flow over a step. *J. Fluid Mech.*, 587:235–354.

Grimshaw, R., Zhang, D.-H., and Chow, K. W. (2009). Transcritical flow over a hole. *Stud. Appl. Math.*, 122:235–248.

Grimshaw, R. H. J. and Maleewong, M. (2015). Critical controls in transcritical shallow-water flow over obstacles. *J. Fluid Mech.*, 780:480–502.

Gurevich, A. V. and Pitaevskii, L. P. (1974). Nonstationary structure of a collisionless shock wave. *Sov. Phys. JETP*, 38:291–297.

Lee, S.-J., Yates, G., and Wu, T.-Y. (1989). Experiments and analyses of upstream-advancing solitary waves generated by moving disturbances. *J. Fluid Mech.*, 199:569–593.

Pratt, L. J. (1984). On nonlinear flow with multiple obstructions. *J. Atmos. Sci.*, 41:1214–1225.

Whitham, G. B. (1965). Non-linear dispersive waves. *Proc. Roy. Soc. London A*, 283:238–261.

Whitham, G. B. (1974). *Linear and Nonlinear Waves*. J. Wiley and Sons.

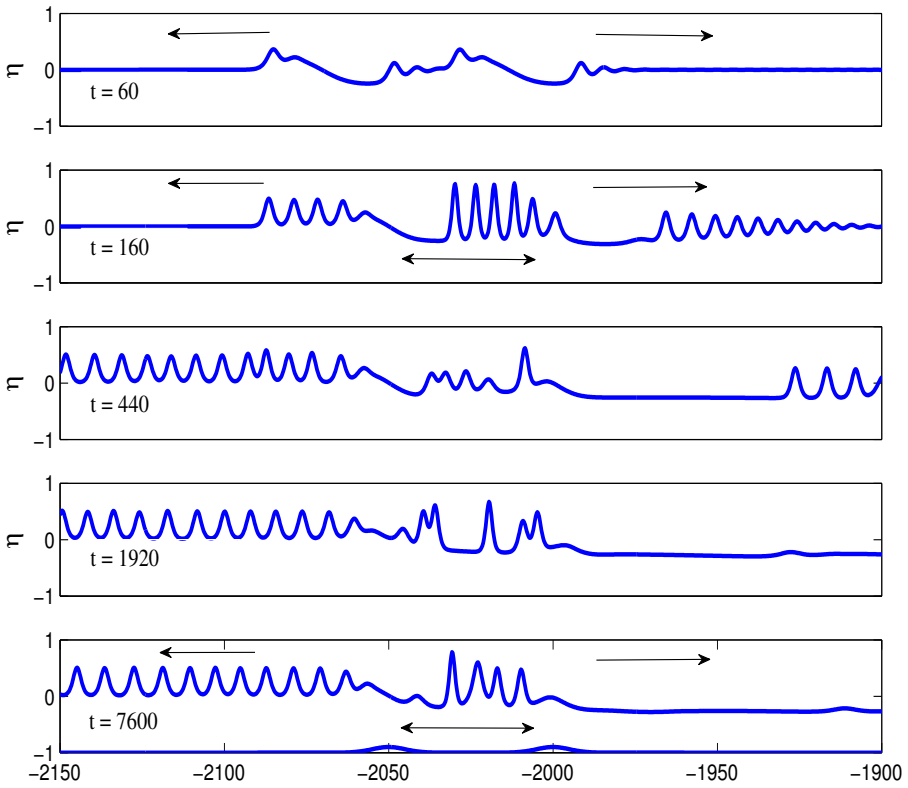

Figure 4.1: Simulations for $F = 1.0, \Delta = 0, \epsilon_1 = \epsilon_2 = 0.1$.

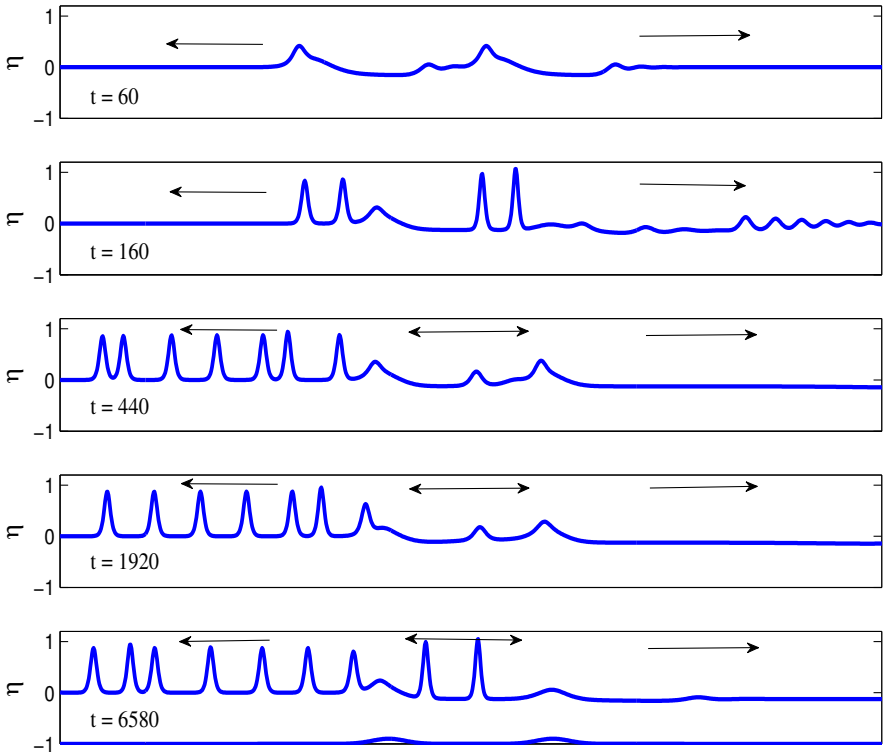

Figure 4.2: Simulations for $F = 1.2, \Delta = 0.2, \epsilon_1 = \epsilon_2 = 0.1$.

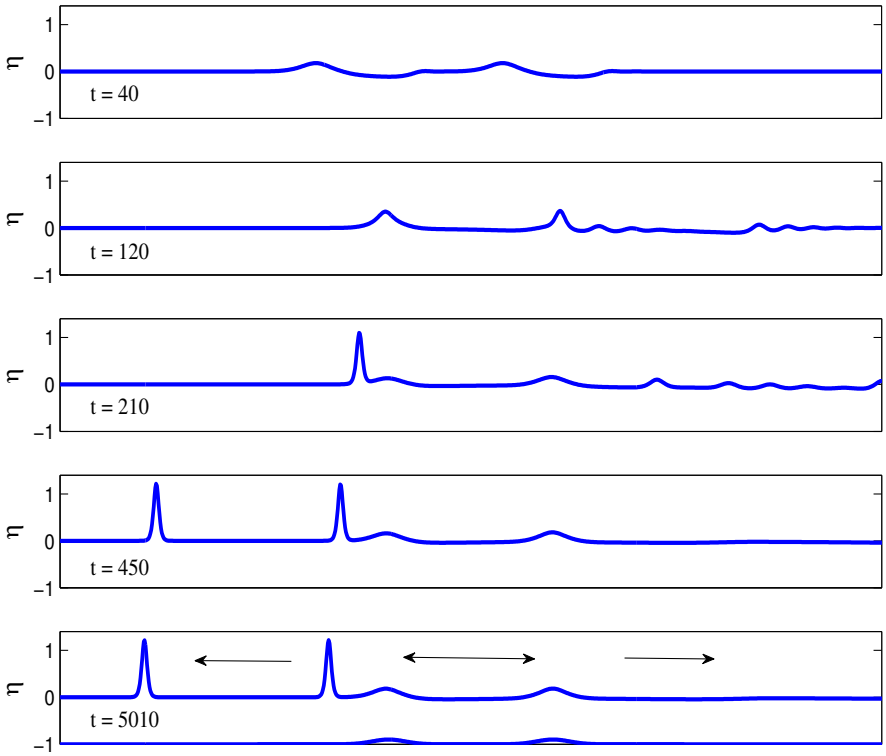

Figure 4.3: Simulations for $F = 1.35, \Delta = 0.35, \epsilon_1 = \epsilon_2 = 0.1$.

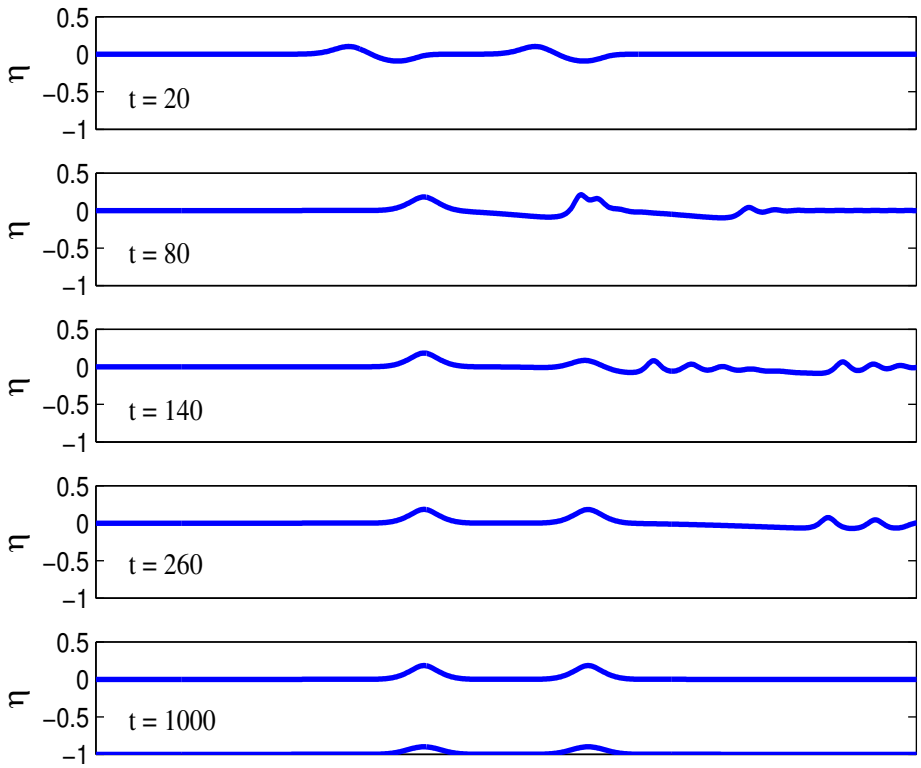

Figure 4.4: Simulations for $F = 1.4, \Delta = 0.4, \epsilon_1 = \epsilon_2 = 0.1$.

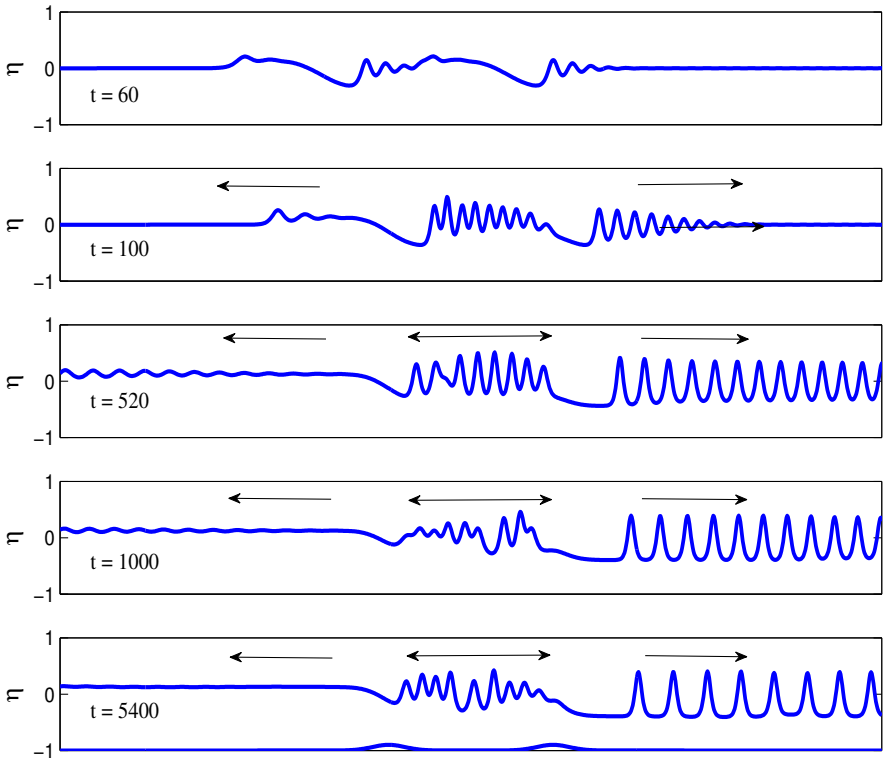

Figure 4.5: Simulations for $F = 0.8, \Delta = -0.2, \epsilon_1 = \epsilon_2 = 0.1$.

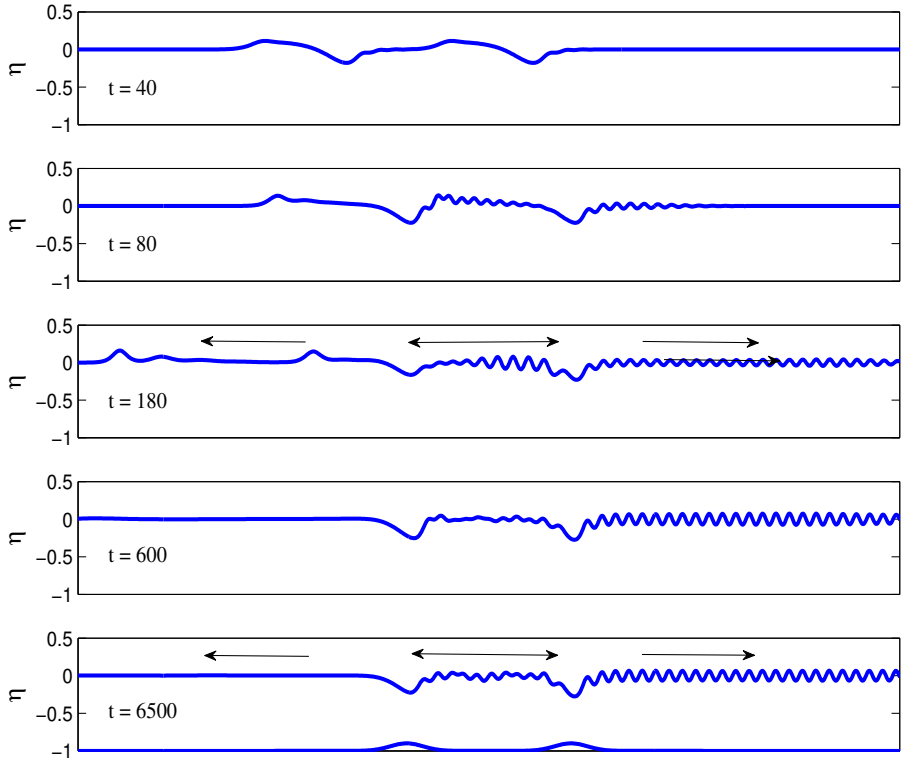

Figure 4.6: Simulations for $F = 0.6, \Delta = -0.4, \epsilon_1 = 0.1, \epsilon_2 = 0.1$.

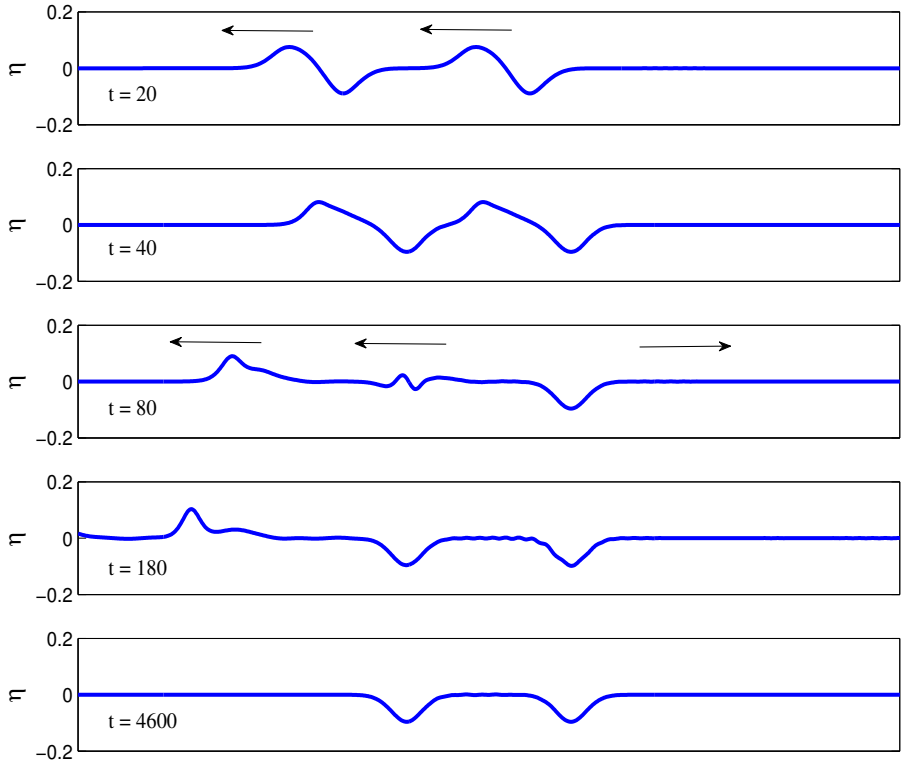

Figure 4.7: Simulations for $F = 0.4, \Delta = -0.6, \epsilon_1 = 0.1, \epsilon_2 = 0.1$.

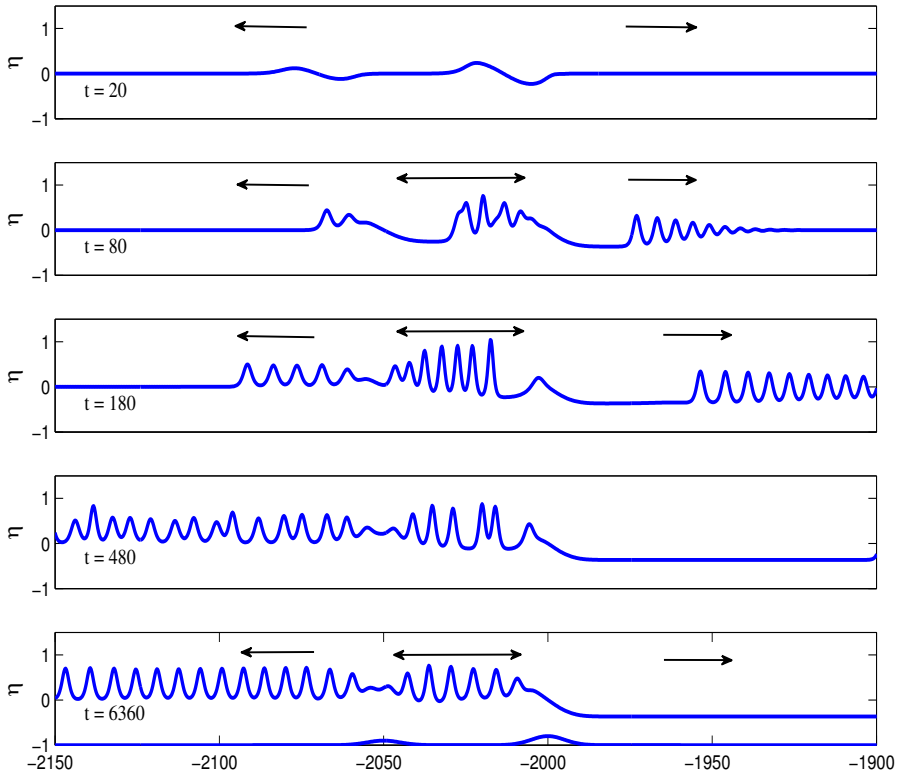

Figure 4.8: Simulations for $F = 1.0, \Delta = 0, \epsilon_1 = 0.1, \epsilon_2 = 0.2$.

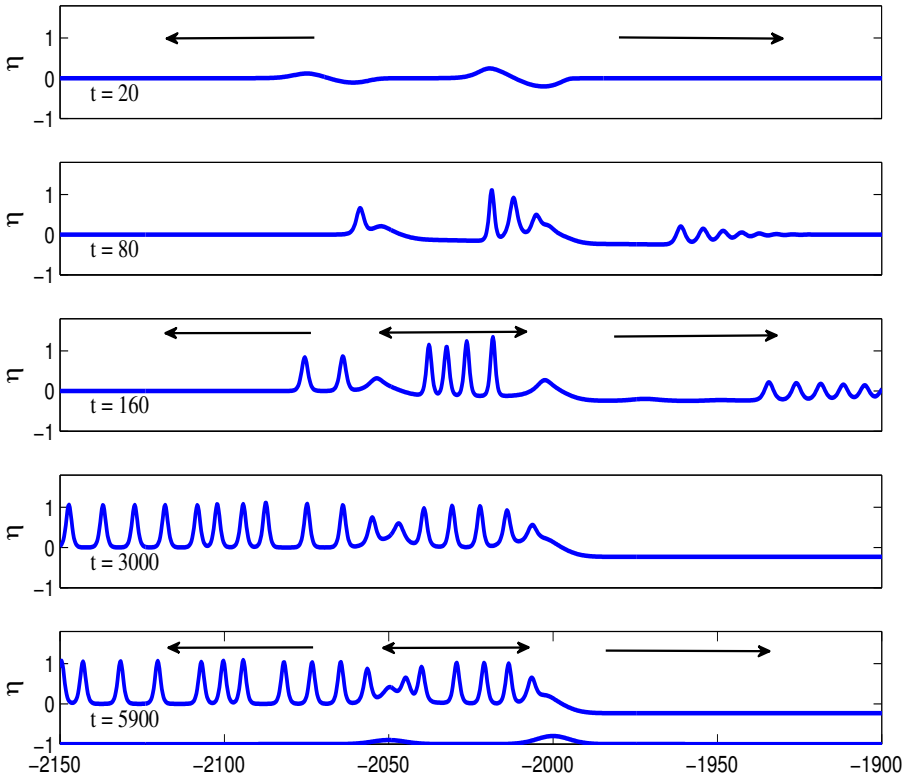

Figure 4.9: Simulations for $F = 1.2, \Delta = 0.2, \epsilon_1 = 0.1, \epsilon_2 = 0.2$.

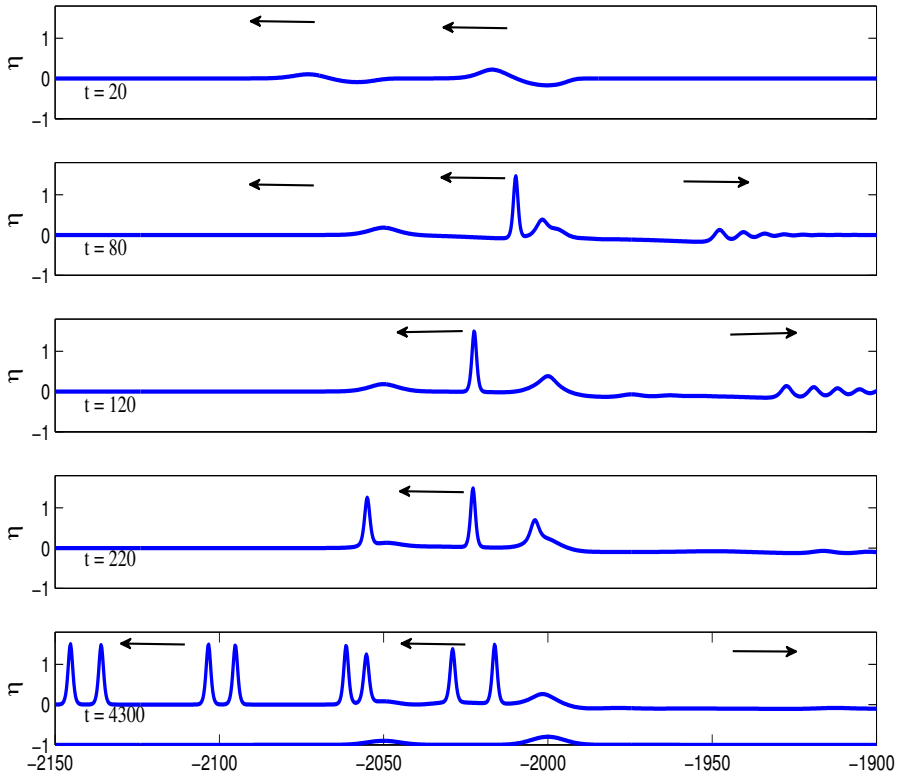

Figure 4.10: Simulations for $F = 1.4, \Delta = 0.4, \epsilon_1 = 0.1, \epsilon_2 = 0.2$.

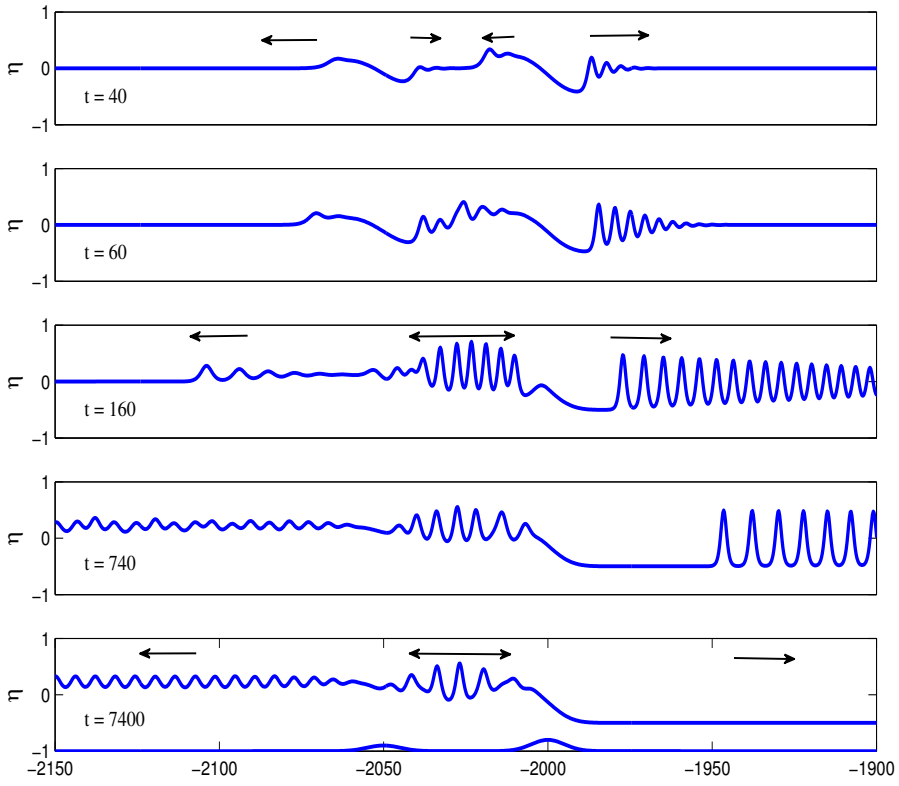

Figure 4.11: Simulations for $F = 0.8, \Delta = -0.2, \epsilon_1 = 0.1, \epsilon_2 = 0.2$.

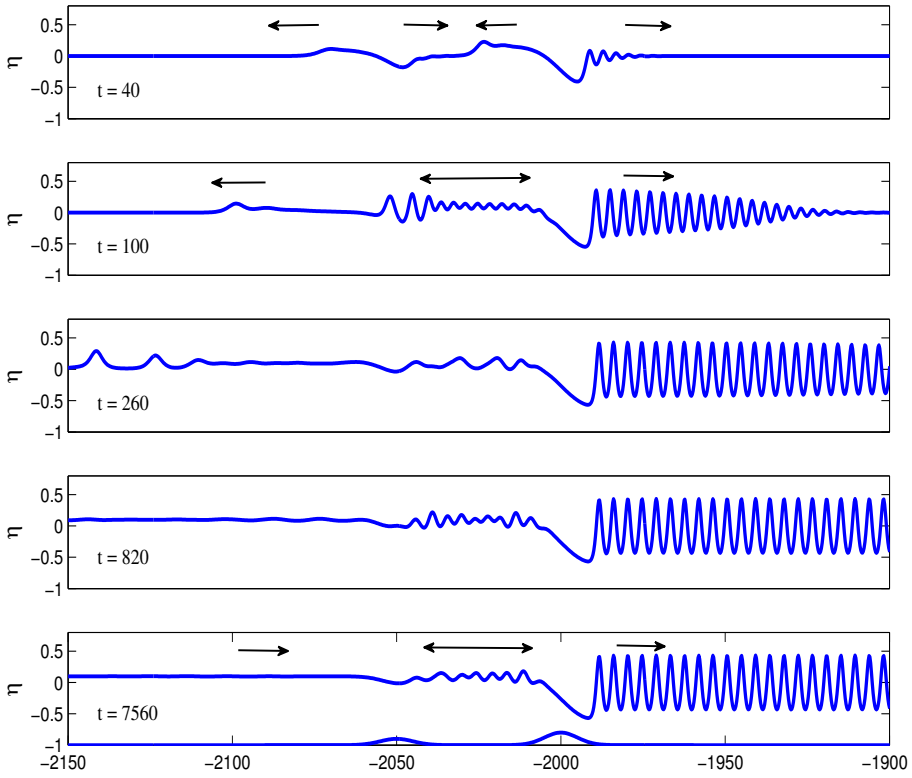

Figure 4.12: Simulations for $F = 0.6, \Delta = -0.4, \epsilon_1 = 0.1, \epsilon_2 = 0.2$.

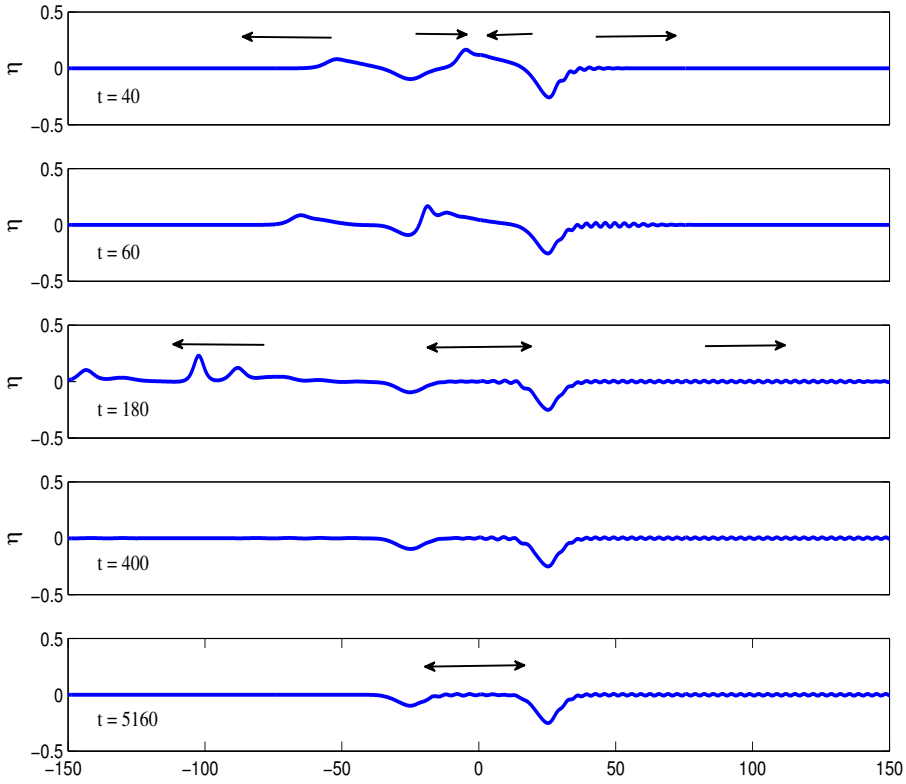

Figure 4.13: Simulations for $F = 0.4, \Delta = -0.6, \epsilon_1 = 0.1, \epsilon_2 = 0.2$.

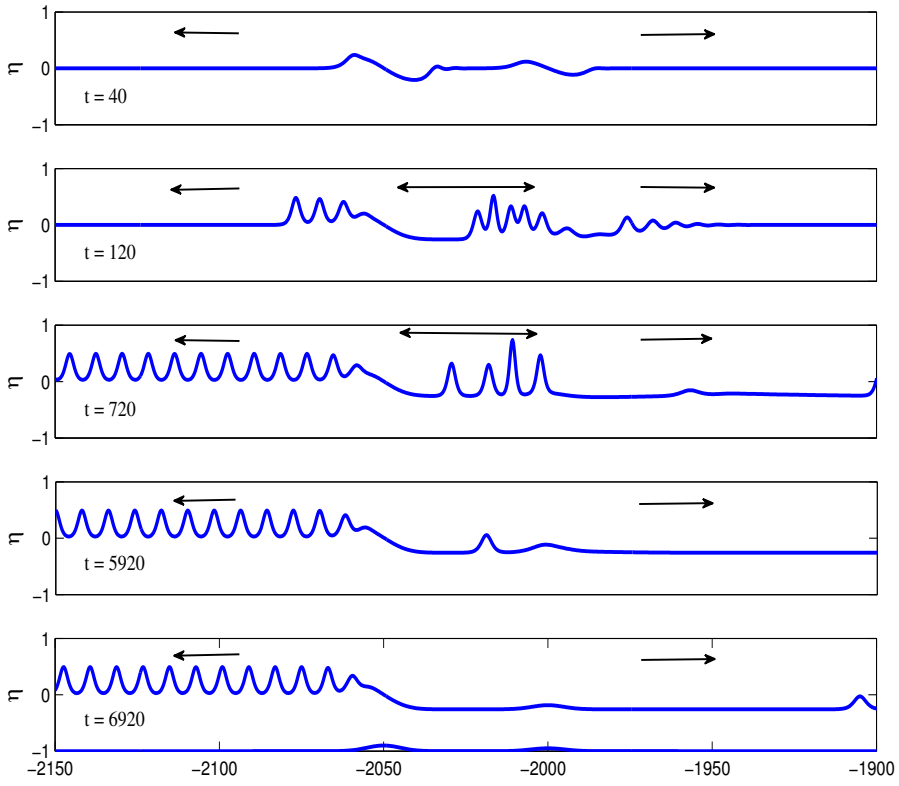

Figure 4.14: Simulations for $F = 1.0, \Delta = 0, \epsilon_1 = 0.1, \epsilon_2 = 0.05$.

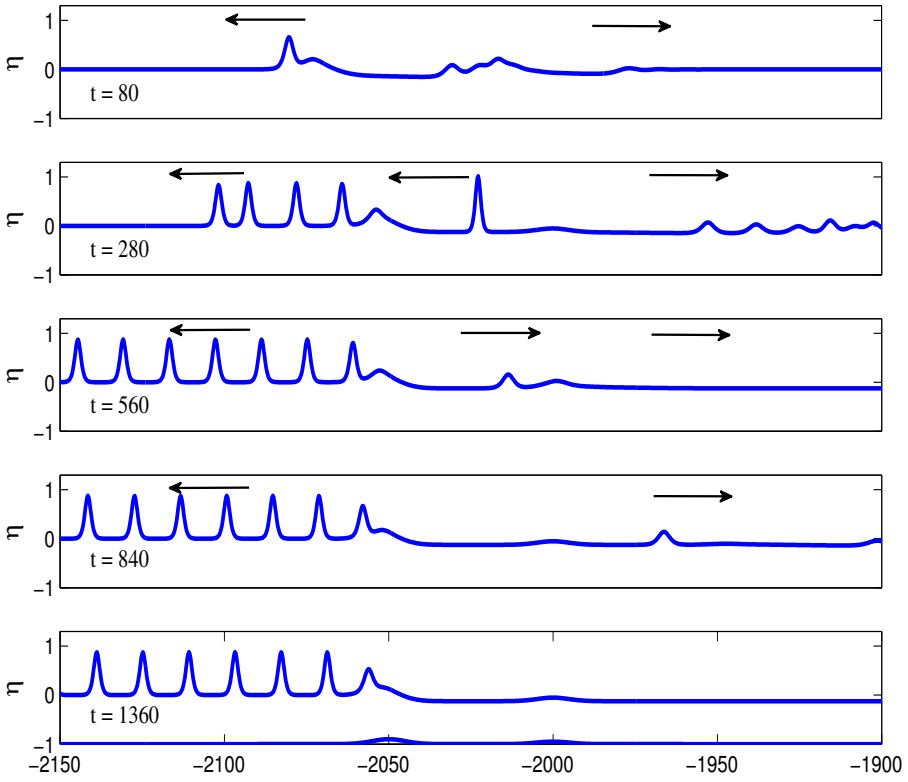

Figure 4.15: Simulations for $F = 1.2, \Delta = 0.2, \epsilon_1 = 0.1, \epsilon_2 = 0.05$.

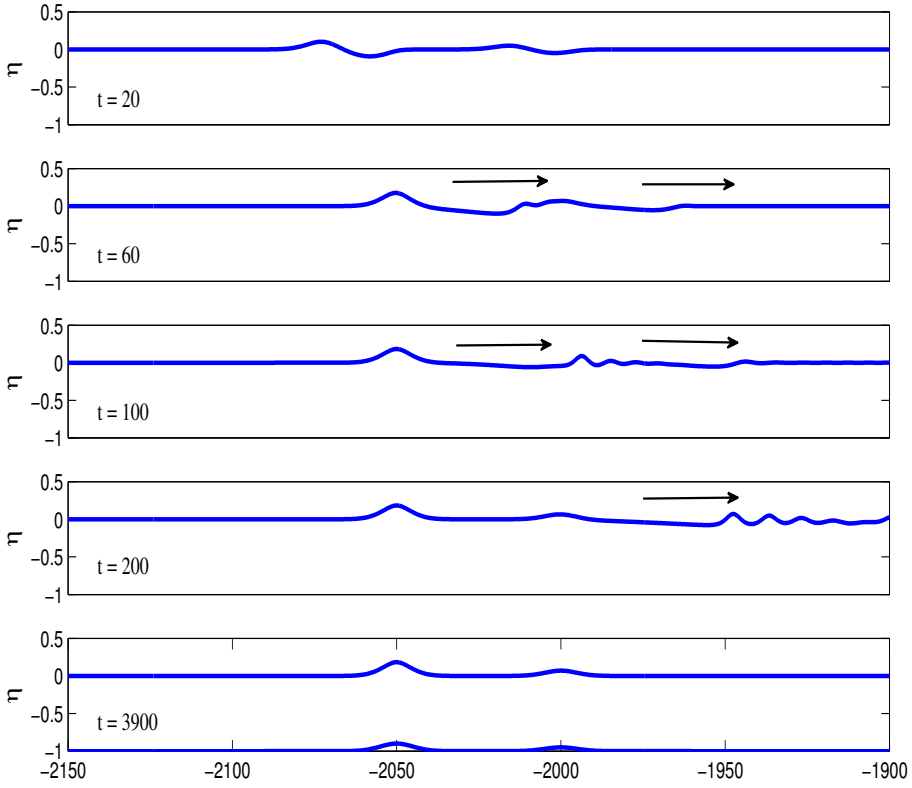

Figure 4.16: Simulations for $F = 1.4, \Delta = 0.4, \epsilon_1 = 0.1, \epsilon_2 = 0.05$.

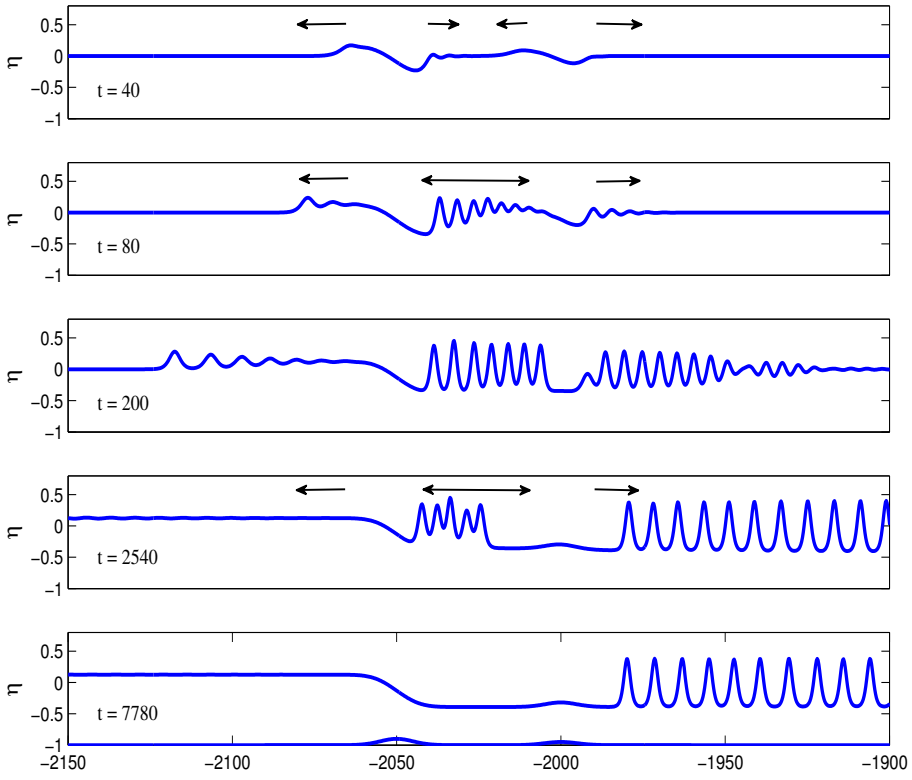

Figure 4.17: Simulations for $F = 0.8, \Delta = -0.2, \epsilon_1 = 0.1, \epsilon_2 = 0.05$.

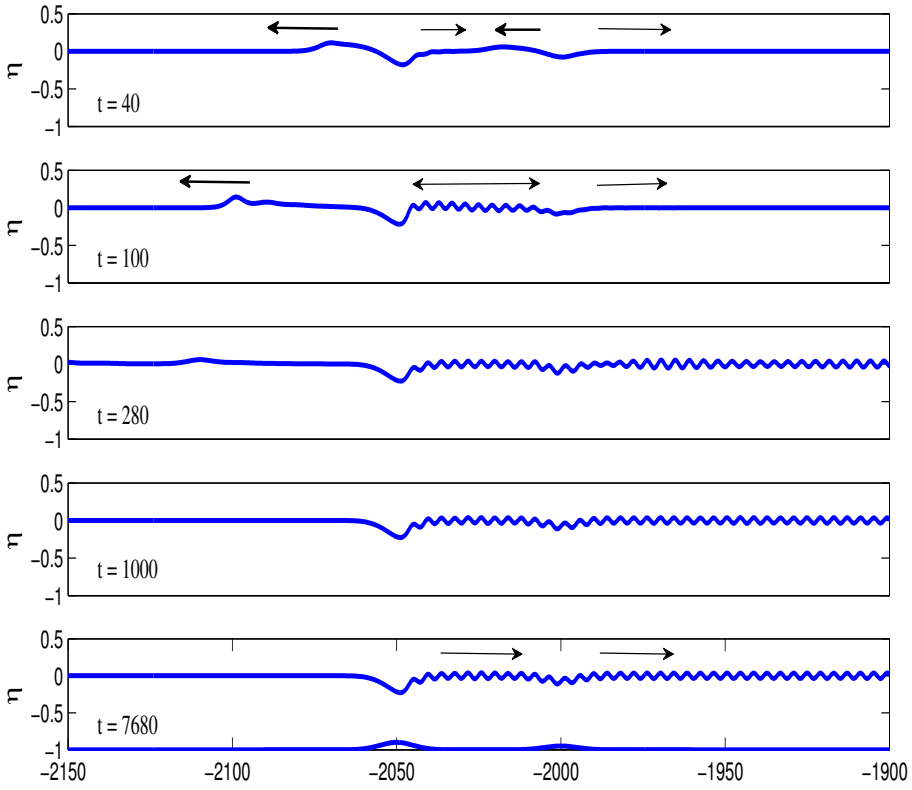

Figure 4.18: Simulations for $F = 0.6, \Delta = -0.4, \epsilon_1 = 0.1, \epsilon_2 = 0.05$.

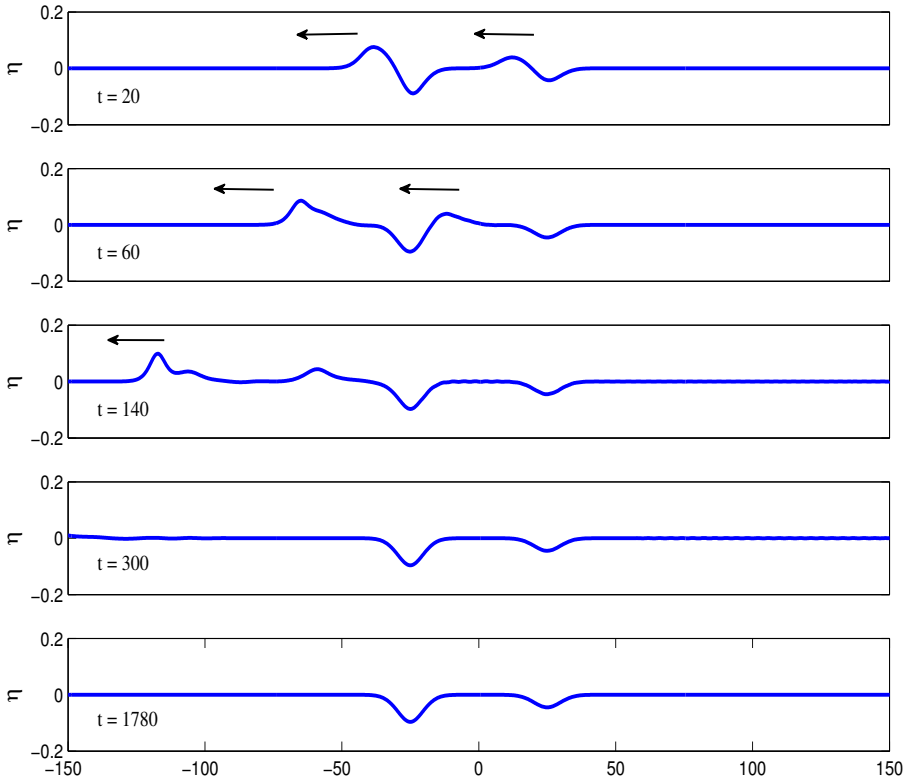

Figure 4.19: Simulations for $F = 0.4, \Delta = -0.6, \epsilon_1 = 0.1, \epsilon_2 = 0.05$.

Project Output

1. ผลงานวิจัยตีพิมพ์
   1.1 Thida Pongsanguansin, Montri Maleewong, and Khamron Mekchay, Consistent weighted average flux of well-balanced TVD-RK discontinuous Galerkin method for shallow water flows, Modelling and Simulation in Engineering, vol. 2015, Article ID 591282 (published)
   1.2 Roger H.J. Grimshaw, and Montri Maleewong, Critical control in transcritical shallow-water flow over two obstacles, Journal of Fluid Mechanics, vol.780, pp.480-502 (2015) (published)
   1.3 Thida Pongsanguansin, Montri Maleewong, and Khamron Mekchay, Shallow-water simulations by a well-balanced WAF finite volume method: a case study to the great flood in 2011, Thailand (submitted 2016)
   1.4 Roger H.J. Grimshaw, and Montri Maleewong, Transcritical flow over two obstacles: forced Korteweg-de Vrise framework (submitted 2016)

2. การนำผลงานวิจัยไปใช้ประโยชน์
   เชิงวิชาการ
   ได้โปรแกรมคอมพิวเตอร์สำหรับศึกษาและจำลองการไหลในช่องทางน้ำเปิดทั้งในหนึ่งและสองมิติ
   นำไปใช้ประกอบการเรียนการสอนวิชาระเบียบวิธีเชิงตัวเลข
   ระเบียบวิธีทางคณิตศาสตร์
   จำลองการไหลจริงรูปแบบอื่นๆ และสร้างนักวิจัยรุ่นใหม่ระดับปริญญาโทและเอก

Appendices

Hindawi Publishing Corporation
Modelling and Simulation in Engineering
Volume 2015, Article ID 591282, 11 pages
http://dx.doi.org/10.1155/2015/591282

Research Article

Consistent Weighted Average Flux of Well-Balanced TVD-RK Discontinuous Galerkin Method for Shallow Water Flows

Thida Pongsanguansin,[1] Montri Maleewong,[2] and Khamron Mekchay[1]

[1]*Department of Mathematics and Computer Science, Chulalongkorn University, Bangkok 10330, Thailand*
[2]*Department of Mathematics, Kasetsart University, Bangkok 10900, Thailand*

Correspondence should be addressed to Montri Maleewong; montri.m@ku.ac.th

Received 26 March 2015; Revised 2 June 2015; Accepted 14 June 2015

Academic Editor: Javier Murillo

A well-balanced scheme with total variation diminishing Runge-Kutta discontinuous Galerkin (TVD-RK DG) method for solving shallow water equations is presented. Generally, the flux function at cell interface in the TVD-RK DG scheme is approximated by using the Harten-Lax-van Leer (HLL) method. Here, we apply the weighted average flux (WAF) which is higher order approximation instead of using the HLL in the TVD-RK DG method. The consistency property is shown. The modified well-balanced technique for flux gradient and source terms under the WAF approximations is developed. The accuracy of numerical solutions is demonstrated by simulating dam-break flows with the flat bottom. The steady solutions with shock can be captured correctly without spurious oscillations near the shock front. This presents the other flux approximations in the TVD-RK DG method for shallow water simulations.

1. Introduction

Hyperbolic balanced law for one-dimensional problem is

$$U_t + F_x(U) = G(U), \tag{1}$$

where U, F, and G represent solution vector, flux function, and source terms, respectively.

In this work, the hyperbolic equation is the shallow water equations which can be expressed by

$$\begin{aligned} h_t + q_x &= 0, \\ q_t + \left(\frac{q^2}{h} + \frac{gh^2}{2}\right)_x &= -ghb_x, \end{aligned} \tag{2}$$

where h is the water depth, $q = uh$ is the discharge, u is the flow velocity in the x-direction, g is the acceleration due to gravity, and b is the bottom function. Equation (2) can be rewritten by setting

$$\begin{aligned} U &= \begin{pmatrix} h \\ q \end{pmatrix}, \\ F(U) &= \begin{pmatrix} q \\ \dfrac{q^2}{h} + \dfrac{gh^2}{2} \end{pmatrix}, \\ G(U) &= \begin{pmatrix} 0 \\ -ghb_x \end{pmatrix}. \end{aligned} \tag{3}$$

The total variation diminishing Runge-Kutta discontinuous Galerkin (TVD-RK DG) method can be applied to solve the shallow water equations; see [1–5]. This scheme has several advantages. For instance, it can be used to handle complex geometries, and in the same time, adaptive strategies are easily applied. The accuracy of numerical solutions can be improved by increasing the polynomial degree of

approximating polynomial and by the method for estimating the flux function at cell interface.

By the concept of discontinuous Galerkin method, numerical solutions need not to be continuous at cell interface. So, we require an efficient flux approximation. Generally, there are several types of approximations. The most famous one is the Harten-Lax-van Leer flux (HLL), while the higher order approximation is the weighted average flux (WAF); see [6–9]. This approach approximates the flux functions by averaging flux in each direction along the wave solutions at the half-time step. It originates from random flux scheme, which was shown to be second-order accuracy in space and time in statistical sense by Toro [6]. From previous work, the weighted average flux has been successfully applied to solve various types of problems, especially in the finite volume method [7, 10, 11]. It improves the accuracy of the finite volume method to be second-order without reconstruction process. But the weighted average flux is rarely applied in the discontinuous Galerkin method. So the main objective of this work is the application of the WAF method in the TVD-RK DG method. We have also shown that the present scheme has consistent property with the WAF approximation.

The steady solutions of (3) can be obtained by setting

$$\begin{aligned} hu &= \text{constant}, \\ \frac{1}{2}u^2 + g(h+b) &= \text{constant}. \end{aligned} \tag{4}$$

Flux gradients are nonzero, and it must be balanced with the bottom gradient. Usually, numerical schemes without balancing these two quantities produce oscillate steady solution. So a balancing numerical scheme is needed, and it is called the well-balanced scheme. This method is designed to preserve energy at steady state. Generally, a numerical scheme is said to be well-balanced if it satisfies the exact C-property which was first introduced by Bermudez and Vazquez [12]. The exact C-property means that the numerical solution must satisfy still water condition at steady state given by

$$\begin{aligned} u &= 0, \\ h+b &= \text{constant}. \end{aligned} \tag{5}$$

Thus, to obtain a well-balanced scheme, we must design the method that its steady solutions satisfy (5).

Recently, the second-order Runge-Kutta discontinuous Gelerkin method with well-balanced scheme is proposed by Kesserwani and Liang [13]. They presented the wetting and drying algorithms for solving one-dimensional problem. Xing and Shu [14] proposed a well-balanced finite volume method based on the weighted essentially nonoscillatory (WENO) scheme for solving one- and two-dimensional problems. They applied the decomposing source term technique into the sum of several terms to ensure the numerical balance between flux difference and source terms. Audusse et al. [15] presented a well-balanced finite volume with hydrostatic reconstruction to solve one-dimensional problem. Later, Noelle et al. [16] extended the well-balanced finite volume schemes proposed by [15] to any that desired the orders of accuracy.

In order to solve the shallow water equations with source terms, we modified the well-balanced discontinuous Galerkin scheme proposed by [15] and related work by Xing and Shu [14]. The weighted average flux (WAF) method [6, 7] has been applied in the modified DG scheme. We will show that the modified TVD-RK DG scheme with the WAF has consistent property. Various numerical experiments for both steady and unsteady flows are demonstrated to show the capability and accuracy of our numerical scheme.

Numerical scheme and its consistency property with WAF for the TVD-RK DG method have been shown in Section 2. The modified well-balanced TVD-RK DG scheme with source terms is presented in Section 3. Numerical examples are demonstrated in Section 4. Conclusions are finally made in Section 5.

2. Numerical Scheme for Shallow Water Equations without Source Term

The TVD-RK DG with weighted average flux method for the case of without source terms is presented in this section.

2.1. TVD-RK Discontinuous Galerkin Method. Consider the one-dimensional hyperbolic conservation law,

$$U_t + F_x(U) = 0. \tag{6}$$

The computational domain $(0, L)$ is divided into K cells. We denote the jth cell by $I_j = [x_{j-1/2}, x_{j+1/2}]$, for $j = 1, \ldots, K$, with uniform cell size $\Delta_j = x_{j+1/2} - x_{j-1/2}$. The cell center is that $x_j = (x_{j+1/2} + x_{j-1/2})/2$, where $x_{j+1/2}$ and $x_{j-1/2}$ are the left and the right of cell boundaries, respectively.

Approximate solution is denoted by $U_h = \binom{h_h}{q_h}$.

Multiplying (6) by a test function, $v_h(x) \in P^N(I_j)$, where $P^N(I_j)$ is the polynomial space degree N on the interval I_j, and replacing U by U_h and then taking the integration by parts over I_j, we obtain a weak form of numerical scheme as

$$\begin{aligned} &\int_{I_j} (\partial_t U_h) v_h dx - \int_{I_j} F(U_h) \partial_x v_h dx + \widehat{F}_{j+1/2} v_h\left(x^-_{j+1/2}\right) \\ &\quad - \widehat{F}_{j-1/2} v_h\left(x^+_{j-1/2}\right) = 0, \end{aligned} \tag{7}$$

where the flux function F at the cell interfaces is approximated by $\widehat{F}$, which is the function of U_h^+ and U_h^- at $x_{j\pm1/2}$ as

$$\widehat{F}_{j\pm1/2} = \widehat{F}\left((U_h)^-_{j\pm1/2}, (U_h)^+_{j\pm1/2}\right). \tag{8}$$

Here $U_h|^-_{j\pm1/2}$ and $U_h|^+_{j\pm1/2}$ denote the approximate solutions at the left and the right of cell boundaries, respectively. If we apply the Legendre polynomials to be a local basis function, the approximate solution U_h can be written by

$$U_h(x,t) = \sum_{m=0}^{N} U_j^m(t)\, \varphi_m(x), \tag{9}$$

where $U_j^m(t)$ is called the temporal coefficient. Now, the basis function $\varphi_m(x)$ is defined by the Legendre polynomial $P_m(x)$ of degree m over $[-1, 1]$.

The test function $v_h(x)$ is typically chosen to be the basis function; that is, $v_h(x) = \{\varphi_l(x)\}_{l=0}^{N}$. So after applying Legendre's properties, (7) is simplified to

$$\frac{dU_j^l(t)}{dt} = \frac{2l+1}{\Delta_j}\int_{I_j} F(U_h)\,\partial_x\varphi_l(x)\,dx + \frac{2l+1}{\Delta_j}\left\{(-1)^l\,\widehat{F}_{j-1/2} - \widehat{F}_{j+1/2}\right\}, \tag{10}$$

for $j = 1,\ldots,K$, and $l = 0,\ldots,N$.

The time derivative term in (10) can be approximated by applying the high-order TVD Runge Kutta (TVD-RK) method; see [1, 3, 17]. Note that, when the polynomial degree N is applied, the TVD-RK method at least the order of $N+1$ must be applied to obtain the accuracy of order $O(\Delta x^{N+1})$ for smooth flows.

The TVD-RK DG method can be used to simulate shallow water flows with moving shocks. Unphysically oscillate behaviours are usually produced near the shock fronts. The slope limiter techniques can be applied to remove the oscillations. In this work, we apply the Monotonic Upstream-Centered Scheme for Conservation Laws (MUSCL) limiter (see [1, 3, 6, 18]) in the TVD-RK DG method. This approach limits the present solution slope by comparing the slope with neighbor cells.

2.2. Weighted Average Flux (WAF). The HLL numerical flux (Harten-Lax-van Leer) is usually used in the TVD-RK DG method. Another choice but higher order is the weighted average flux (WAF). It was first introduced by Toro; see [6, 7]. The WAF approximation is second-order accurate in both space and time in statistical sense [6]. This approximation has been extensively applied in the finite volume method, but it is rarely used in the TVD-RK DG method. So the main objective of this work is to try to modify the WAF in the TVD-RK DG method.

The weighted average flux, $\widehat{F}^{\mathrm{WAF}}$ at the interface, $x_{j+1/2}$, is defined by the integral average of a flux function $F(U)$ at the half-time step,

$$\widehat{F}^{\mathrm{WAF}}_{j+1/2} = \frac{1}{\Delta x}\int_{-\Delta x/2}^{\Delta x/2} F\left(U_{j+1/2}\left(x, \frac{\Delta t}{2}\right)\right)dx. \tag{11}$$

It can be written in the wave structure form as

$$\widehat{F}^{\mathrm{WAF}}_{j+1/2} = \sum_{k=1}^{N_c+1}\omega_k F^{(k)}_{j+1/2}, \tag{12}$$

where N_c is the number of wave solutions in the Riemann problem and $F^{(k)}_{j+1/2}$ is the kth flux of the Riemann problem. For one-dimensional shallow water flows, we have $N_c = 2$, where $F^{(1)}_{j+1/2} = F(U^-_{j+1/2})$ and $F^{(3)}_{j+1/2} = F(U^+_{j+1/2})$. Flux component $F^{(2)}_{j+1/2}$ can be obtained from the HLL approach [6]. Weighted values, ω_k, are defined by $\omega_k = (1/2)(c_k - c_{k-1})$, where $c_k = S_k\Delta t/\Delta x$ is the Courant number of wave k, $c_0 = -1$, $c_{N_c+1} = 1$, and S_k is the speed of wave k.

To avoid spurious oscillations near a shock front, the WAF method will be modified by enforcing a total variation diminishing (TVD) scheme [6, 7, 9, 11, 19]. The TVD-WAF version is that

$$\widehat{F}^{\mathrm{WAF-TVD}}_{j+1/2} = \frac{1}{2}\left(F\left(U^-_{j+1/2}\right) + F\left(U^+_{j+1/2}\right)\right) - \frac{1}{2}\sum_{k=1}^{N_c}\mathrm{sgn}\left(c_k\right)\phi^{(k)}_{j+1/2}\Delta F^{(k)}_{j+1/2}, \tag{13}$$

where

$$\Delta F^{(k)}_{j+1/2} = F^{(k+1)}_{j+1/2} - F^{(k)}_{j+1/2}. \tag{14}$$

Here $\phi^{(k)}_{j+1/2}$ is a WAF limiter function. There are various choices; see more details in [6, 7, 9, 11, 19]. In this work, we choose the basic one of minmod type.

2.3. Consistency of WAF with TVD-RK DG Method. In this section, we show the consistency of the weighted average flux in the TVD-RK discontinuous Galerkin method.

Lemma 1. *The TVD Runge-Kutta discontinuous Galerkin method is consistent with the weighted average flux for smooth flows.*

Proof. Considering the weak form of RKDG method for the conservation law,

$$\int_{I_j}\left(\frac{\partial}{\partial t}U\right)v(x)\,dx - \int_{I_j}F(U)\,v'(x)\,dx - F\left(U_{j+1/2}\right)v\left(x^-_{j+1/2}\right) + F\left(U_{j-1/2}\right)v\left(x^+_{j-1/2}\right) = 0. \tag{15}$$

Solution U is approximated by U_h^*. The test function v is estimated by v_h. Flux function at cell interfaces is approximated in terms of numerical flux, $\widehat{F}_{j\pm1/2}$, so we obtain a numerical scheme of the following form:

$$\int_{I_j}\left(\frac{\partial}{\partial t}U_h^*\right)v_h(x)\,dx - \int_{I_j}F\left(U_h^*\right)v_h'(x)\,dx - \widehat{F}_{j+1/2}\left(\left(U_h^*\right)^-_{j+1/2},\left(U_h^*\right)^+_{j+1/2}\right)v_h\left(x^-_{j+1/2}\right) + \widehat{F}_{j-1/2}\left(\left(U_h^*\right)^-_{j-1/2},\left(U_h^*\right)^+_{j-1/2}\right)v_h\left(x^+_{j-1/2}\right) = 0. \tag{16}$$

Substituting U_h^* by U in (16) and subtracting with (15), we obtain a truncation error term T_1 as

$$T_1 = \left|\int_{I_j}\frac{\partial}{\partial t}\left[U - U\right]v_h(x)\,dx - \int_{I_j}\left[F(U) - F(U)\right]v_h'(x)\,dx\right.$$

$$- \left[F\left(U_{j+1/2}\right) - \widehat{F}_{j+1/2}\left(U^-_{j+1/2}, U^+_{j+1/2}\right)\right] v_h\left(x^-_{j+1/2}\right) + \left[F\left(U_{j-1/2}\right) - \widehat{F}_{j-1/2}\left(U^-_{j-1/2}, U^+_{j-1/2}\right)\right] \cdot v_h\left(x^+_{j-1/2}\right)\Bigg|. \tag{17}$$

When the solution is smooth, it must be continuous at $x_{j+1/2}$ or $U^+_{j+1/2} = U^-_{j+1/2} = U_{j+1/2}$. □

The TVD weighted average flux is defined by

$$\widehat{F}_{j+1/2}\left(U^-_{j+1/2}, U^+_{j+1/2}\right) = \frac{1}{2}\left(F\left(U^-_{j+1/2}\right) + F\left(U^+_{j+1/2}\right)\right) - \frac{1}{2}\sum_{k=1}^{2} \operatorname{sgn}\left(c_k\right)\phi^k \Delta F^{(k)}, \tag{18}$$

where $F^{(1)} = F(U^-_{j+1/2}) = F(U_{j+1/2})$, $F^{(3)} = F(U^+_{j+1/2}) = F(U_{j+1/2})$, and the component $F^{(2)} = F(U_{j+1/2})$ which can be obtained from the HLL method [4, 6, 7]. Thus,

$$\widehat{F}_{j+1/2}\left(U^-_{j+1/2}, U^+_{j+1/2}\right) = \frac{1}{2}\left(F\left(U_{j+1/2}\right) + F\left(U_{j+1/2}\right)\right) - \frac{1}{2}\sum_{k=1}^{2} \operatorname{sgn}\left(c_k\right)\phi^k \Delta F^{(k)} = F\left(U_{j+1/2}\right). \tag{19}$$

Similarly, we have $\widehat{F}_{j-1/2}(U^-_{j-1/2}, U^+_{j-1/2}) = F(U_{j-1/2})$. Then, the weighted average flux is consistent.

For the TVD-RK DG method, the approximate solution U^*_h in (16) is defined by

$$U^*_h(x,t) = \sum_{k=0}^{N} U_k(t)\,\varphi_k(x), \tag{20}$$

where $\varphi_k(x)$ is the Legendre polynomial degree k. Since the considering solution is smooth, we know from Theorem (3.1) in [1] that

$$\left\|U - U^*_h\right\|_{L^2(0,1)} \le O\left(\Delta x^{N+1/2}\right), \quad \text{for } N \ge 0. \tag{21}$$

This norm is defined as a truncation error term due to approximating polynomial, denoted by T_2.

After substituting the approximate solution into the numerical scheme (16), we obtain an ODE system,

$$\frac{d}{dt}U^*_h = L\left(U^*_h\right). \tag{22}$$

Next, we apply the TVD Runge-Kutta scheme for integrating in time. We approximate U^*_h at each time step by $\widehat{U}_h$. The order of accuracy for time integration depends on the TVD-RK order [1, 3, 17]. If the TVD-RK order $N + 1$ is applied, a truncation error term T_3 is given by

$$T_3 = \left|U^*_h - \widehat{U}_h\right| \le O\left(\Delta t^{N+1}\right). \tag{23}$$

Combining all of the truncation error terms together, the total truncation error term T is estimated by

$$T = T_1 + T_2 + T_3 \le O\left(\Delta x^{N+1/2}, \Delta t^{N+1}\right). \tag{24}$$

The total truncation error term is approaching zero as $\Delta x \to 0$ and $\Delta t \to 0$. Hence, the TVD-RK DG with the WAF method is consistent.

3. Well-Balanced TVD-RK DG with WAF Scheme

In this section, we develop a well-balanced scheme for the TVD-RK DG with the WAF method. The main purpose is to present a modified scheme for solving the shallow water equations with source term. Also, this scheme must preserve exactly stationary solution when bottom slope exists. Let us start by considering the standard TVD-RK DG method,

$$\int_{I_j}\left(\partial_t U_h\right) v_h dx - \int_{I_j} F\left(U_h\right)\partial_x v_h dx + \widehat{F}_{j+1/2} v_h\left(x^-_{j+1/2}\right) - \widehat{F}_{j-1/2} v_h\left(x^+_{j-1/2}\right) = \int_{I_j} G\left(U_h\right) v_h dx, \tag{25}$$

with initial condition

$$\int_{I_j} U_h(x,0)\, v_h(x)\, dx = \int_{I_j} U_0(x)\, v_h(x)\, dx, \tag{26}$$

where $\widehat{F}_{j\pm1/2}$ are the weighted average flux in (13). Source term is given by

$$G(U) = \begin{pmatrix} G_1(U,x) \\ G_2(U,x) \end{pmatrix} = \begin{pmatrix} 0 \\ -ghb_x \end{pmatrix}. \tag{27}$$

We will derive a well-balanced scheme based on [14], but the weighted average flux is applied in the TVD-RK DG instead of using the Lax-Friedrichs (LF) flux. The main modification is the source term treatments in the WAF method. Assume that the source terms can be written by the summation of some functions as

$$G_p(U,x) = \sum_i s_i\left(a(U,x)\right) t'_i(x), \quad p = 1, 2, \tag{28}$$

where s_i and t_i are some functions which will be determined later.

If the solution at steady state is stationary, then $a(U, x)$ in (28) can be decomposed by $a_1(U, x)$ and $a_2(U, x)$, such that

$$a_1 \equiv h + b = \text{constant},$$
$$a_2 \equiv u = 0. \tag{29}$$

Since G_1 is zero, we consider only G_2,

$$G_2(U, x) = -ghb_x = -g(h+b)b_x + \frac{1}{2}g\left(b^2\right)_x. \tag{30}$$

From (28), we have that

$$s_1 = s_1(a_1) = -g(h+b),$$
$$s_2 = \frac{1}{2}g,$$
$$t_1(x) = b,$$
$$t_2(x) = b^2. \tag{31}$$

To balance the flux gradient and the source term approximation at steady state, it is required that

$$\frac{d}{dx}\left(F(U(x)) - \sum_i s_i(a(U, x))\, t_i(x)\right) = 0, \tag{32}$$

or

$$F(U(x)) - \sum_i s_i(a(U, x))\, t_i(x) = \alpha, \tag{33}$$

where α is arbitrary constant.

The integration of source term in (25) can be approximated by

$$\int_{I_j} G_2(U_h, x)\, v_h dx = \int_{I_j} \sum_i s_i(a(U, x))\, t_i'(x)\, v_h(x)\, dx$$
$$= \sum_i \left[\frac{1}{2}\left(s_i\left(a(U_h, x)^+_{j-1/2}\right) + s_i\left(a(U_h, x)^-_{j+1/2}\right)\right)\right]\left[t_i(x_{i+1/2})\, v_h\left(x^-_{i+1/2}\right) - t_i(x_{i-1/2})\, v_h\left(x^+_{i-1/2}\right) - \int_{I_j} t_i(x)\, v_h'(x)\, dx\right] \tag{34}$$
$$+ \sum_i \left[\int_{I_j}\left\{s_i(a(U_h, x)) - \frac{1}{2}\left(s_i\left(a(U_h, x)^+_{j-1/2}\right) + s_i\left(a(U_h, x)^-_{j+1/2}\right)\right)\right\} t_i'(x)\, v_h(x)\, dx\right].$$

Functions $a(u_h, x)$ and t_i on the RHS of (34) can be approximated by $a_h(U_h, x)$ and $(t_i)_h$, where $a_h(U_h, x)$ and $(t_i)_h$ are the L^2 projection of $a(U_h, x)$ and t_i into the space of V_h. Then, we obtain $(t_1)_h = b_h$ and $(t_2)_h = b_h^2$. Thus,

$$F(U_h(x)) - \sum_i s_i(a(U_h, x))\left(t_i(x)_h\right) = \alpha. \tag{35}$$

Then,

$$\int_{I_j} G_2(U_h, x)\, v_h dx = \sum_i \left[\frac{1}{2}\left(s_i\left(a_h(U_h, x)^+_{j-1/2}\right) + s_i\left(a_h(U_h, x)^-_{j+1/2}\right)\right)\right]$$
$$\cdot \left[\left(\widehat{t}_i\right)_{h,j+1/2} v_h\left(x^-_{i+1/2}\right) - \left(\widehat{t}_i\right)_{h,j-1/2}(x_{i-1/2})\, v_h\left(x^+_{i-1/2}\right) - \int_{I_j}(t_i)_h(x)\, v_h'(x)\, dx\right] \tag{36}$$
$$+ \sum_i \left[\int_{I_j}\left\{s_i(a_h(U_h, x)) - \frac{1}{2}\left(s_i\left(a_h(U_h, x)^+_{j-1/2}\right) + s_i\left(a_h(U_h, x)^-_{j+1/2}\right)\right)\right\}(t_i)_h'(x)\, v_h dx\right].$$

To satisfy the weighted average flux in (12), $\left(\widehat{t}_i\right)_{h,j+1/2}$ must be modified. Here, we assume that

$$\left(\widehat{t}_i\right)_{h,j+1/2} = \sum_{k=1}^{N_c+1} \omega_k t^{(k)}_{h,j+1/2}, \tag{37}$$

or if the TVD version in (13) is applied, this term can be written by

$$\left(\widehat{t}_i\right)_{h,j+1/2} = \sum_{k=1}^{N_c+1} \operatorname{sgn}(c_k)\, \phi^{(k)} t^{(k)}_{h,j+1/2}. \tag{38}$$

Note that ω_k are weighted values in the WAF approximations and $\phi^{(k)}$ is the WAF limiter function. So $t^{(k)}_{h,j+1/2}$ can be defined similar to $F^{(k)}_{j+1/2}$.

For one-dimensional shallow water equations, we have $N_c = 2$, where $t^{(1)}_{h,j+1/2} = t_h(x^-_{j+1/2})$ and $t^{(3)}_{h,j+1/2} = t_h(x^+_{j+1/2})$. The approximation of $t^{(2)}_{h,j+1/2}$ in the intermediate region can be obtained by the HLL approach,

$$t^{(2)}_{h,j+1/2} = \begin{cases} t_h\left(x^-_{j+1/2}\right), & \text{if } S_L \geq 0, \\ \dfrac{S_R t_h\left(x^-_{j+1/2}\right) - S_L t_h\left(x^+_{j+1/2}\right) + S_R S_L\left(t_h\left(x^+_{j+1/2}\right) - t_h\left(x^-_{j+1/2}\right)\right)}{S_R - S_L}, & \text{if } S_L < 0 < S_R, \\ t_h\left(x^+_{j+1/2}\right), & \text{if } S_R \leq 0. \end{cases} \tag{39}$$

Here S_L and S_R are signal velocities in the Riemann problem.

At steady state, the solution is assumed to be stationary. It implies that $h + b = c$, where c is constant and $u = 0$. From (35), we have that

$$\begin{aligned} &F\left(U_h\right) - \sum_i s_i\left(a_h\left(U, x\right)\right) t_i\left(x\right) \\ &= \frac{1}{2} g\left(h_h\right)^2 - \left[\frac{1}{2} g b_h^2 - g\left(h_h + b_h\right) b_h\right] \\ &= \frac{1}{2} g\left(h_h + b_h\right)^2 = \frac{1}{2} g c^2 = \alpha. \end{aligned} \tag{40}$$

This shows the suitable choices of $a(U_h, x)$ and t_i in the TVD-RK DG with the WAF approximation.

Next, we will show that the TVD-RK DG with the WAF method preserves the well-balanced property.

Proposition 2. *The TVD-RK DG with the WAF scheme has preserved exactly stationary solutions at steady state.*

Proof. Since $a_h(U_h, x)$ and $a_h(U_h, x)^{\pm}_{i\mp1/2}$ are equal to the same constant c at each Gauss-Lobatto point over cell I_j, thus

$$\sum_i \left[\int_{I_j} \left\{s_i\left(a_h\left(U_h, x\right)\right) - \frac{1}{2}\left(s_i\left(a_h\left(U_h, x\right)^+_{j-1/2}\right) + s_i\left(a_h\left(U_h, x\right)^-_{j+1/2}\right)\right)\right\} \left(t_i\right)'_h\left(x\right) v_h dx\right] = 0. \tag{41}$$

Hence, we obtain a truncation error term T as

$$\begin{aligned} T = &\int_{I_j} F\left(U_h\left(x,t\right)\right) v'_h\left(x\right) dx - \widehat{F}_{j+1/2} v_h\left(x^-_{j+1/2}\right) \\ &+ \widehat{F}_{j-1/2} v_h\left(x^+_{j-1/2}\right) + \sum_i \left[\frac{1}{2}\left(s_i\left(a_h\left(U_h, x\right)^+_{j-1/2}\right)\right.\right. \\ &\left.\left. + s_i\left(a_h\left(U_h, x\right)^-_{j+1/2}\right)\right)\right] \left[\left(\widehat{t}_i\right)_{h,j+1/2} v_h\left(x^-_{i+1/2}\right)\right. \\ &- \left(\widehat{t}_i\right)_{h,j-1/2}\left(x_{i-1/2}\right) v_h\left(x^+_{i-1/2}\right) \\ &\left. - \int_{I_j} \left(t_i\right)_h\left(x\right) v'_h\left(x\right) dx\right]. \end{aligned} \tag{42}$$

Using $\widehat{F}$ in (12), $(\widehat{t}_i)$ in (37), and $a_h(U_h, x)^{\pm}_{j\mp1/2} = c$, we have that

$$\begin{aligned} T = &\int_{I_j} \left[F\left(U_h\left(x,t\right)\right) - \sum_i s_i\left(c\right)\left(t_i\right)_h\right] v'_h\left(x\right) dx \\ &- \left[\sum_{k=1}^{3} \omega_k F^{(k)}_{j+1/2} - \sum_i s_i\left(c\right)\left(\sum_{k=1}^{3} \omega_k t^{(k)}_{h,j+1/2}\right)\right] \\ &\cdot v_h\left(x^-_{j+1/2}\right) \\ &+ \left[\sum_{k=1}^{3} \omega_k F^{(k)}_{j-1/2} - \sum_i s_i\left(c\right)\left(\sum_{k=1}^{3} \omega_k t^{(k)}_{h,j-1/2}\right)\right] \\ &\cdot v_h\left(x^+_{j-1/2}\right) \\ = &\int_{I_j} \left[F\left(U_h\left(x,t\right)\right) - \sum_i s_i\left(c\right)\left(t_i\right)_h\right] v'_h\left(x\right) dx \\ &- \left[\sum_{k=1}^{3} \omega_k \left(F^{(k)}_{j+1/2} - \sum_i s_i\left(c\right) t^{(k)}_{h,j+1/2}\right)\right] v_h\left(x^-_{j+1/2}\right) \\ &+ \left[\sum_{k=1}^{3} \omega_k \left(F^{(k)}_{j-1/2} - \sum_i s_i\left(c\right) t^{(k)}_{h,j-1/2}\right)\right] v_h\left(x^+_{j-1/2}\right). \end{aligned} \tag{43}$$

After applying condition (35) and rearranging terms, yields

$$\begin{aligned} T = &\alpha\left[v_h\left(x^-_{j+1/2}\right) - v_h\left(x^+_{j-1/2}\right)\right] - \alpha v_h\left(x^-_{j+1/2}\right) \\ &+ \alpha v_h\left(x^+_{j-1/2}\right) = 0, \end{aligned} \tag{44}$$

where α is arbitrary constant. Hence, the TVD-RK DG with the WAF scheme preserves exactly the stationary solution at steady state. □

Table 1: RMS errors when $N = 0$, $N = 1$, and $N = 2$.

N	Numerical flux	$K = 50$	$K = 100$	$K = 200$
$N = 0$	HLL	0.0280	0.0215	0.0165
	WAF	0.0182	0.0127	0.0094
$N = 1$	HLL	0.0130	0.0102	0.0072
	WAF	0.0107	0.0093	0.0067
$N = 2$	HLL	0.0103	0.0079	0.0053
	WAF	0.0100	0.0076	0.0052

Remark 3. One can show that the developed well-balanced TVD-RK DG with WAF scheme in the case of existing source term is consistent, by showing that the approximation of the source term is also consistent.

4. Numerical Results

In this section, various test cases have been investigated to demonstrate the accuracy of the present scheme, not only steady, but also unsteady flows.

4.1. Dam Break Flow. It has been shown in the previous section that the weighted average flux is consistent with the TVD-RK DG method. We apply this modified scheme to solve the shallow water equations without source terms in this subsection. The accuracy of numerical solutions is shown and compared with the standard TVD-RK DG when using the HLL method.

The computational domain is that $-5 \le x \le 5$. The initial water depth is given by

$$h(x,t) = \begin{cases} 1, & \text{if } x \le 0, \\ 0.6, & \text{if } x > 0. \end{cases} \tag{45}$$

The initial velocity is assumed to be zero. The boundary conditions are transmissive boundaries. We perform 50, 100, and 200 cells in the numerical experiments. Polynomial degree zero, one, and two are applied as a local basis in the TVD-RK DG method. Simulation time is $t = 2$, with $\Delta t = 0.005$. The root mean squared errors (RMS) are shown in Table 1.

When N and K are fixed, the accuracy of numerical solution obtained from the WAF is higher than those obtained from the HLL method. The RMS errors decrease as K increases.

If we fix K and vary N, the RMS error decreases as the polynomial degree increases.

The water depth profiles using the HLL and the WAF methods at $t = 2$ when $N = 1$ and $K = 100$ are shown in Figures 1 and 2, respectively. The front of moving shock can be captured correctly by the HLL and the WAF methods. But the scheme using the WAF can capture shock and rarefaction wave more precisely than those using the HLL method. This investigation shows the accuracy of the TVD-RK DG with the WAF method. It has been generalized from the finite volume method.

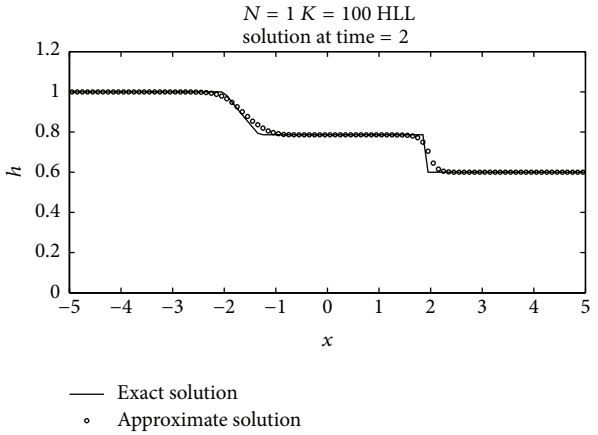

Figure 1: Exact solution and water depth profile obtained by the TVD-RK DG HLL method.

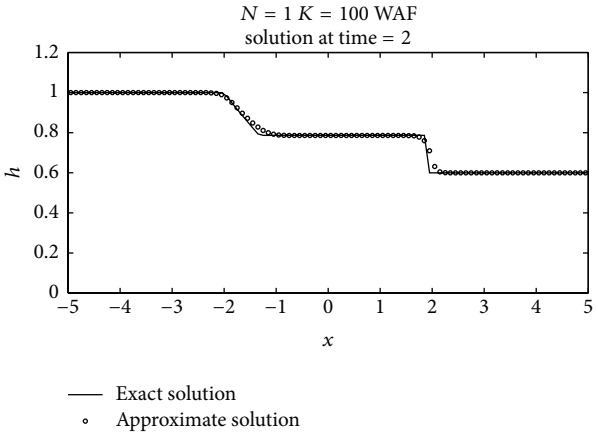

Figure 2: Exact solution and water depth profile obtained by the TVD-RK DG WAF method.

4.2. Flow over Irregular Bed. The uniform channel is length of 1500 m. The bottom elevation is irregular that is shown in Figure 3. This problem is proposed by [5] for testing the accuracy of numerical scheme at stationary state. The boundary conditions are transmissive. The initial water depth is that $h + b = 16$, with zero initial velocity. We set $\Delta t = 0.01$ and run simulation until $t = 100$.

It can be seen from Figure 3 that the well-balanced scheme (dot) gives exactly the stationary solution while the non-well-balanced scheme (dash line) gives solution error especially in the high gradient area of bottom elevation.

4.3. Steady Flow over a Bump. We consider the shallow water flows over a bump in a rectangular channel with length of 25 m. The bump elevation is given by

$$b(x) = \begin{cases} 0.2 - 0.05(x-10)^2, & \text{if } 8 < x < 12, \\ 0, & \text{otherwise.} \end{cases} \tag{46}$$

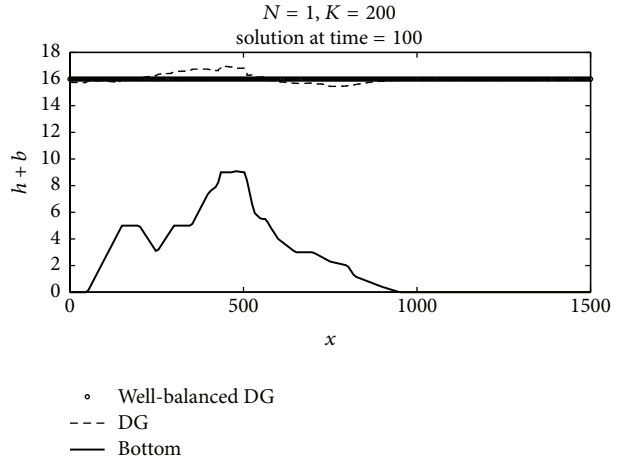

Figure 3: Stationary flow over irregular bed by well-balanced and non well-balanced TVD-RK DG with WAF method.

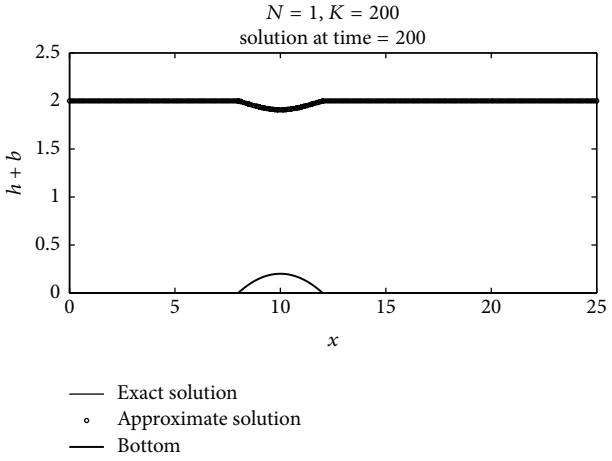

Figure 4: Water depth and bump profiles for subcritical flow.

Table 2: RMS errors when $N = 1$ for subcritical flow over a bump.

	$K = 50$	$K = 100$	$K = 200$	$K = 400$
HLL	$1.6954e-03$	$4.5563e-04$	$1.2546e-04$	$3.5900e-05$
WAF	$1.5816e-03$	$4.1648e-04$	$1.1474e-04$	$3.3019e-05$

At steady state, classical flows can be characterised by subcritical flow, transcritical flow with shock, and transcritical flow without shock. The TVD-RK DG with the WAF method is performed to solve these problems. The accuracy of numerical solutions can be checked by comparing with the existing analytical solutions; see [20].

Subcritical Flow over a Bump. The upstream boundary is imposed by $q = 4.42\,\mathrm{m}^2/\mathrm{s}$, while the downstream boundary is set by $h = 2$ m. The initial water depth is $h + b = 2$ with zero initial velocity. Time step is that $\Delta t = 0.01$. The RMS errors obtained from the HLL and the WAF methods are shown in Table 2. This shows that the RMS errors obtained by the TVD-RK DG WAF are less than those obtained by the HLL for all K.

The water depth and the bump profiles are shown in Figure 4. The numerical solution is very close to the analytical solution. We also found in this test case that the well-balanced scheme converges to the steady solution faster than the scheme that is not well-balanced.

Transcritical Flow with Shock over a Bump. The upstream boundary is given by $q = 0.18\,\mathrm{m}^2/\mathrm{s}$, while the downstream boundary is set by $h = 0.33$ m. The initial condition is that $h + b = 0.33$ m. The comparison of water surfaces is shown in Figure 5. The numerical result is in good agreement with the analytical result. This shows the accuracy of the well-balanced scheme that can capture the shock front without any oscillations. It is also found that the well-balanced scheme converges to the steady solution faster than the non-well-balanced scheme.

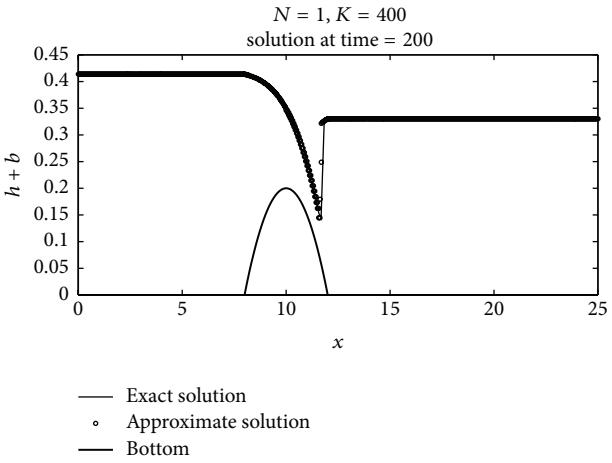

Figure 5: Transcritical flow with shock over a bump.

Transcritical Flow without Shock over a Bump. The upstream boundary is prescribed by $q = 1.53\,\mathrm{m}^2/\mathrm{s}$, while the downstream boundary is not specified. The initial conditions is that $h + b = 0.4$ m with zero initial velocity.

The water depth profiles are shown in Figure 6. The numerical result agrees well with the analytical solution. These results show the accuracy of the well-balanced scheme for solving transcritical flow problem.

4.4. Small Perturbation of Steady State Water. This problem is first proposed by [18, 21, 22]. It can be used to study the capability of numerical scheme for solving small perturbation in shallow water flow. The bottom topography is defined by

$$b(x) = \begin{cases} 0.25\left(\cos\left(10\pi\left(x - 1.5\right)\right) + 1\right), & \text{if } 1.4 < x < 1.6, \\ 0. & \text{otherwise.} \end{cases} \quad (47)$$

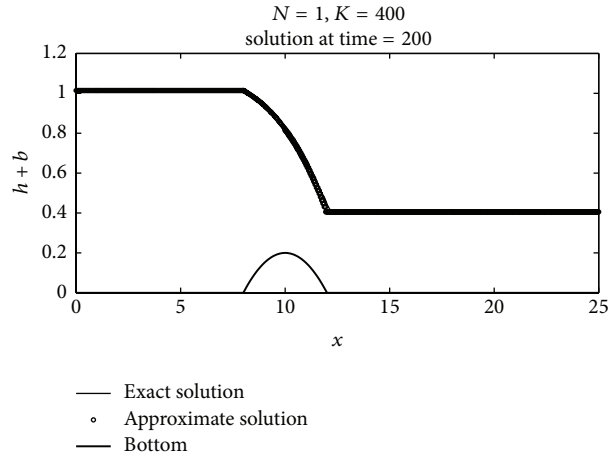

Figure 6: Transcritical flow without shock over a bump.

The initial conditions are specified by

$$q(x,0) = 0,$$
$$h(x,0) = \begin{cases} 1 - b(x) + \epsilon, & \text{if } 1.1 < x < 1.2, \\ 1 - b(x), & \text{otherwise,} \end{cases} \quad (48)$$

where ϵ is a nonzero perturbation constant. The boundary conditions are transmissive boundaries. In this work, we consider the cases of $\epsilon = 0.2$ and 0.01. The disturbance of initial water depth from small ϵ should split the initial wave into two waves. They propagate to the left and the right with characteristic speed $\pm\sqrt{gh}$ at the early stage. A standard scheme which is not well-balanced usually faces with some difficulties to capture correctly the wave speed.

In our simulation, we use 400 uniform grid cells and polynomial degree one in the TVD-RK DG with the WAF method. The simulation time is that $t = 0.7$.

The comparison of water depths between our results and the Leveque's solutions is shown in Figures 7 and 8 for $\epsilon = 0.01$ and 0.2, respectively. They are in good agreement for both amplitude and wave speed. These test cases show the ability of our numerical scheme for solving the quasi-stationary flow with initial disturbance.

4.5. Flow over Nonhorizontal Bed. This test case is presented by [8]. The main propose is to study the ability of numerical scheme for solving unsteady flow over topography. The uniform channel is length of 30 m. The bed elevation is defined by

$$b(x) = \begin{cases} 0, & \text{if } 0 \le x \le 10, \\ 0.1(x - 10), & \text{if } 10 \le x \le 20, \\ 1, & \text{if } 20 \le x \le 30. \end{cases} \quad (49)$$

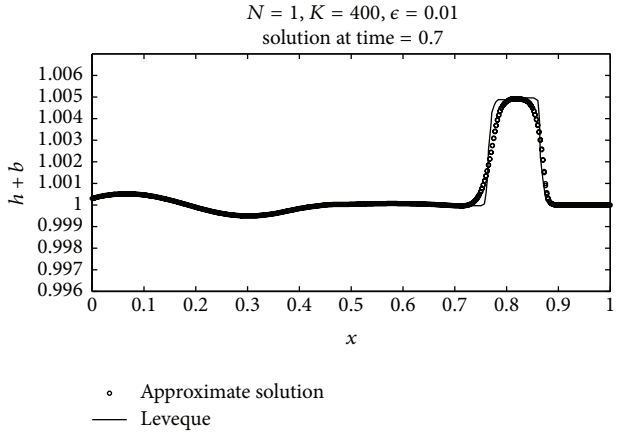

Figure 7: Quasi-stationary flow when $\epsilon = 0.01$.

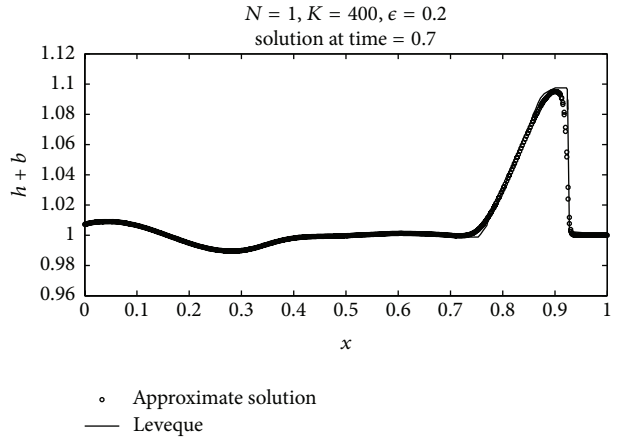

Figure 8: Quasi-stationary flow when $\epsilon = 0.2$.

The initial conditions are given by

$$h(x) + b(x) = \begin{cases} 4, & \text{if } 0 \le x < 5, \\ 2, & \text{if } 5 \le x \le 30. \end{cases} \quad (50)$$

Here, we set $\Delta t = 0.01$ and use 200 uniform grid cells with polynomial degree one to simulate the unsteady flow. The boundary conditions are transmissive boundaries.

Our numerical results when comparing with Toro's solutions [8] at $t = 1$ s and 4 s are shown in Figure 9. Wave speed and shock profiles are very close. These results show the accuracy of the present scheme for solving unsteady flow with source term.

5. Conclusions

In this work, we present the TVD-RK discontinuous Galerkin method (TVD-RK DG) for solving nonlinear shallow water equations. Most of the TVD-RK DG methods in the literatures usually approximate intercell flux by applying the

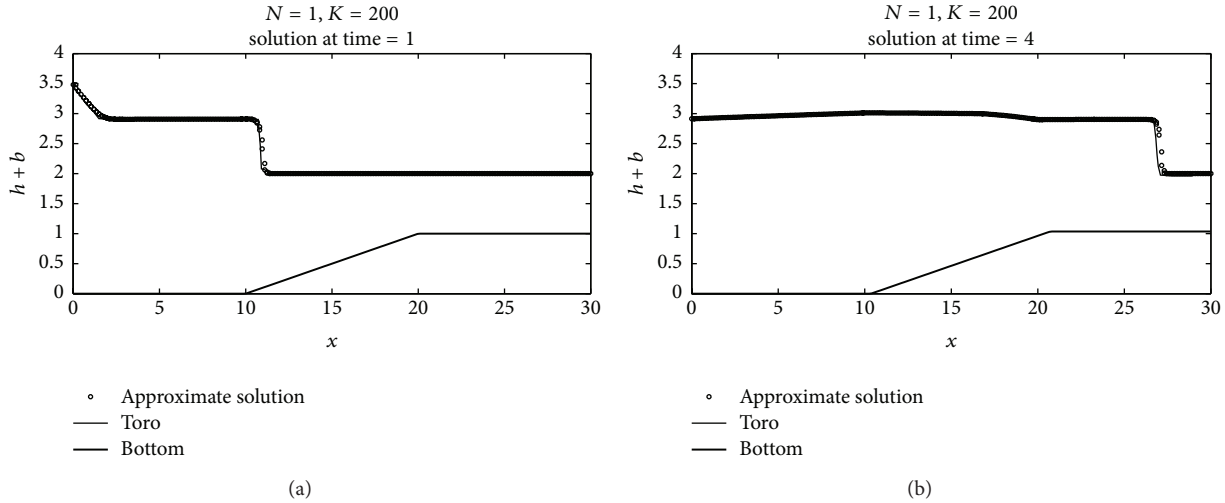

Figure 9: Flow over non-horizontal bed at time 1 s (a) and 4 s (b).

HLL method. But here we apply another approach called the weighted average flux (WAF) in the TVD-RK DG. We have also shown the consistent property of the TVD-RK DG with the WAF approximation. Then the well-balanced TVD-RK DG scheme with the WAF approximation is developed. The present method can be used to simulate not only steady flows, but also unsteady flows. The accuracy of modified numerical scheme is demonstrated by various test cases, flow over irregular bed, steady flow over a bump, quasi-stationary, and flow over nonhorizontal bed. The well-balanced TVD-RK DG with the WAF method can be used to solve all the kinds of these problems. Moreover, if we restrict at steady state, the scheme using the WAF method converges to the steady solution faster than the scheme using the HLL method. In addition, the well-balanced scheme converges to the steady solution faster than the scheme that is not well-balanced. Due to its advantages of numerical accuracy, simplicity, and well-balanced property, the present scheme can be modified and extended to simulate two-dimensional problems. However, depending on the types of elements, for example, triangles or rectangles, it is not trivial to extend for two-dimensional problems due to the polynomial basis functions and the WAF fluxes at element interfaces and is not considered in this paper.

Conflict of Interests

The authors declare that there is no conflict of interests regarding the publication of this paper.

Acknowledgments

This research is partially supported by the Science Achivement Scholarship Thailand (SAST) to the first author and financially supported by the Thailand Research Fund (TRF) under the Grant no. RSA5680038.

References

[1] B. Cockburn, C. W. Shu, C. Johnson, and E. Tadmor, *Advanced Numerical Approximation of Nonlinear Hyperbolic Equations: Lectures Given at the 2nd Session of the Centro Internazionale Matematico Estivo (C.I.M.E.) held in Cetraro, Italy, June 23–28, 1997*, Springer, 1998.

[2] D. Schwanenberg, R. Kiem, and J. Kongeter, "A discontinuous Galerkin method for the shallow-water equations with source terms," in *Discontinuous Galerkin Methods: Theory, Computations and Applications*, B. Cockburn, G. E. Karniadaki, and C.-W. Chu, Eds., Lecture Notes in Computational Science and Engineering, pp. 1419–1424, Springer, 2000.

[3] J. S. Hesthaven and T. Warburton, *Nodal Discontinuous Galerkin Methods: Algorithms, Analysis, and Applications*, Springer, 2008.

[4] P. A. Tassi and C.-A. Vionnet, "Discontinuous Galerkin method for the one dimensional simulation of shallow water flows," *Mecànica Computational*, vol. 22, pp. 2403–2428, 2003.

[5] W. Lai and A. A. Bouchut, "Discontinuous Galerkin method for 1D shallow water flow with water surface slope limiter," *International Journal on Civil and Environmental Engineering*, vol. 3, pp. 167–176, 2011.

[6] E. F. Toro, *Riemann Solvers and Numerical Methods for Fluid Dynamics: A Practical Introduction*, Springer, Berlin, Germany, 1999.

[7] E. F. Toro, *Shock-Capturing Methods for Free-Surface Shallow Flows*, John Wiley & Sons, New York, NY, USA, 2001.

[8] E. F. Toro, "Riemann problems and the WAF method for solving the two-dimensional shallow water equations," *Philosophical Transactions of the Royal Society of London A: Mathematical, Physical and Engineering*, vol. 338, no. 1649, pp. 43–68, 1992.

[9] M. Maleewong, "Modified predictor-corrector WAF method for the shallow water equations with source terms," *Mathematical Problems in Engineering*, vol. 2011, Article ID 178491, 17 pages, 2011.

[10] E. F. Toro and P. L. Roe, "A hybridised high-order random choice method for quasi-linear hyperbolic systems," in *Proceedings of the 16th International Symposium on Shock Tubes and Waves*, p. 701, Gronig, Aachen, Germany, July 1987.

[11] S. J. Billett and E. F. Toro, "On WAF-type schemes for multidimensional hyperbolic conservation laws," *Journal of Computational Physics*, vol. 130, no. 1, pp. 1–24, 1997.

[12] A. Bermudez and M. E. Vazquez, "Upwind methods for hyperbolic conservation laws with source terms," *Computers & Fluids*, vol. 23, no. 8, pp. 1049–1071, 1994.

[13] G. Kesserwani and Q. Liang, "Well-balanced RKDG2 solutions to the shallow water equations over irregular domains with wetting and drying," *Computers & Fluids*, vol. 39, no. 10, pp. 2040–2050, 2010.

[14] Y. Xing and C.-W. Shu, "High order well-balanced finite volume WENO schemes and discontinuous Galerkin methods for a class of hyperbolic systems with source terms," *Journal of Computational Physics*, vol. 214, no. 2, pp. 567–598, 2006.

[15] E. Audusse, F. Bouchut, M.-O. Bristeau, R. Klein, and B. Perthame, "A fast and stable well-balanced scheme with hydrostatic reconstruction for shallow water flows," *SIAM Journal on Scientific Computing*, vol. 25, no. 6, pp. 2050–2065, 2004.

[16] S. Noelle, N. Pankratz, G. Puppo, and J. R. Natvig, "Well-balanced finite volume schemes of arbitrary order of accuracy for shallow water flows," *Journal of Computational Physics*, vol. 213, no. 2, pp. 474–499, 2006.

[17] C.-W. Shu, "Total-variation-diminishing time discretizations," *SIAM Journal on Scientific and Statistical Computing*, vol. 9, no. 6, pp. 1073–1084, 1988.

[18] R. J. Leveque, *Finite Volume Method for Hyperbolic Problem*, Cambridge University Press, 2005.

[19] E. D. Fernández-Nieto and G. Narbona-Reina, "Extension of WAF type methods to non-homogeneous shallow water equations with pollutant," *Journal of Scientific Computing*, vol. 36, no. 2, pp. 193–217, 2008.

[20] O. Delestre, C. Lucas, P.-A. Ksinant et al., "SWASHES: a compilation of shallow water analytic solutions for hydraulic and environmental studies," *International Journal for Numerical Methods in Fluids*, pp. 346–365, 2012.

[21] R. J. Leveque, *Numerical Methods for Conservation Laws*, Birkhäuser Press, 1992.

[22] R. J. LeVeque, "Balancing source terms and flux gradients in high-resolution Godunov methods: the quasi-steady wave-propagation algorithm," *Journal of Computational Physics*, vol. 146, no. 1, pp. 346–365, 1998.

J. Fluid Mech. (2015), *vol.* 780, *pp.* 480–502. © Cambridge University Press 2015
doi:10.1017/jfm.2015.485

Critical control in transcritical shallow-water flow over two obstacles

Roger H. J. Grimshaw[1] **and Montri Maleewong**[2,†]

[1]Department of Mathematical Sciences, Loughborough University, Loughborough LE11 3TU, UK

[2]Department of Mathematics, Faculty of Science, Kasetsart University, Bangkok 10900, Thailand

(Received 2 June 2015; revised 10 August 2015; accepted 13 August 2015)

The nonlinear shallow-water equations are often used to model flow over topography. In this paper we use these equations both analytically and numerically to study flow over two widely separated localised obstacles, and compare the outcome with the corresponding flow over a single localised obstacle. Initially we assume uniform flow with constant water depth, which is then perturbed by the obstacles. The upstream flow can be characterised as subcritical, supercritical and transcritical, respectively. We review the well-known theory for flow over a single localised obstacle, where in the transcritical regime the flow is characterised by a local hydraulic flow over the obstacle, contained between an elevation shock propagating upstream and a depression shock propagating downstream. Classical shock closure conditions are used to determine these shocks. Then we show that the same approach can be used to describe the flow over two widely spaced localised obstacles. The flow development can be characterised by two stages. The first stage is the generation of upstream elevation shock and downstream depression shock from each obstacle alone, isolated from the other obstacle. The second stage is the interaction of two shocks between the two obstacles, followed by an adjustment to a hydraulic flow over both obstacles, with criticality being controlled by the higher of the two obstacles, and by the second obstacle when they have equal heights. This hydraulic flow is terminated by an elevation shock propagating upstream of the first obstacle and a depression shock propagating downstream of the second obstacle. A weakly nonlinear model for sufficiently small obstacles is developed to describe this second stage. The theoretical results are compared with fully nonlinear simulations obtained using a well-balanced finite-volume method. The analytical results agree quite well with the nonlinear simulations for sufficiently small obstacles.

Key words: hydraulic control, shallow water flows, topographic effects

1. Introduction

1.1. *Background*

Shallow-water flow of a homogeneous fluid over bottom topography is a fundamental problem in fluid mechanics and has been heavily studied from various points of view. A widely used approach when the topography is a single localised obstacle

† Email address for correspondence: Montri.M@ku.ac.th

is the application of hydraulic concepts which lead to the classification of the flow in terms of the value of the upstream Froude number, defined as the ratio of the uniform upstream flow to the linear long-wave speed. The flow is then described as supercritical, subcritical or transcritical depending on whether the upstream Froude number is greater than unity, less than unity, or close to unity, respectively; see for instance the monograph by Baines (1995) for a comprehensive account of hydraulic theory and the issues involved. In the supercritical case, waves generated by the flow interaction with the obstacle propagate downstream away from the obstacle, and the flow at the obstacle location is a locally steady elevation. In the subcritical case, waves propagate upstream and downstream away from the obstacle, and the flow at the obstacle location is a locally steady depression. When wave dispersion is considered, steady lee waves are also formed downstream of the obstacle. Both these cases can be well understood, at least qualitatively, using linearised theory.

However, linearised theory fails in the transcritical regime, which is the main interest here, and then a nonlinear theory is needed to describe the locally steady hydraulic flow over the obstacle, which has an upstream elevation and a downstream depression, each terminated by upstream- and downstream-propagating undular bores. A popular model here in the weakly nonlinear regime when the obstacle has a small amplitude is the forced Korteweg–de Vries (KdV) equation; see Akylas (1984), Cole (1985), Grimshaw & Smyth (1986), Lee, Yates & Wu (1989), Binder, Dias & Vanden-Broeck (2006), Grimshaw, Zhang & Chow (2007) and the recent review by Grimshaw (2010). Various aspects of the extension to finite amplitudes in the long-wave regime can be found in El, Grimshaw & Smyth (2006, 2008, 2009).

Thus transcritical shallow-water flow is quite well understood for a single localised obstacle, but there have been comparatively very few studies of the analogous case when there are two widely separated localised obstacles. In the context of this paper, the most relevant is the article by Pratt (1984), where a combination of steady hydraulic theory, numerical simulations using the nonlinear shallow-water equations and laboratory experiments are used to infer that the formation of dispersive waves between the obstacles is needed to obtain a stable solution. More recently Dias & Vanden-Broeck (2004) and Ee *et al.* (2010, 2011) have examined the possible presence of such waves for steady flows, while Grimshaw, Zhang & Chow (2009) considered the related problem of unsteady flow over a wide hole. Thus a new feature of interest when considering two obstacles is that the waves generated by each obstacle may interact in the region between them, and then the question is how this interaction might affect the long-time outcome. In this paper we examine this scenario using the nonlinear shallow-water equations, so that, although finite-amplitude effects are included, wave dispersion is neglected and the generated waves are represented as shock waves. Our emphasis is on the transcritical regime for two widely spaced localised obstacles. The nonlinear shallow-water equations are solved numerically using a well-balanced finite-volume method, and the results are shown in § 3. The simulations are supplemented by a combination of fully nonlinear hydraulic theory with classical shock closure conditions, and a reduced model used in the weakly nonlinear regime, presented in § 2. We conclude in § 4.

1.2. *Formulation*

The basic model is one-dimensional shallow-water flow past topography, in which the flow is described by the total local depth H and the depth-averaged horizontal velocity U. The upstream flow is a constant horizontal velocity $V > 0$, and the forcing

is due to a localised topographic obstacle $f(x)$ so that the bottom is at $z = -h + f(x)$, where h is the undisturbed depth at infinity. Henceforth, we use non-dimensional coordinates, based on a length scale h, a velocity scale $\sqrt{gh}$ and a time scale of $\sqrt{h/g}$, in terms of which the equation system is

$$\zeta_t + (HU)_x = 0, \quad H = 1 + \zeta - f, \tag{1.1a,b}$$

$$U_t + UU_x + \zeta_x = 0. \tag{1.2}$$

In these non-dimensional coordinates, the constant upstream flow is $Fr = V/\sqrt{gh}$, the Froude number. Here the topography $f(x)$ consists of two obstacles, each symmetrical, and placed a distance L apart, with respective maximum heights (or depths) of $\epsilon_{1,2}$. Our interest here is when $\epsilon_{1,2} > 0$, and the situation when either or both $\epsilon_{1,2} < 0$ will be considered elsewhere. We assume that the separation distance L is much greater than the width of the obstacles. Then the main parameters are the Froude number Fr, and the maximum heights $\epsilon_{1,2}$. This system is to be solved with the initial conditions

$$H = 1, \quad U = Fr, \quad \text{at } t = 0. \tag{1.3a,b}$$

This is equivalent to introducing the obstacles instantaneously at $t = 0$ into a constant flow. The solution will initially develop smoothly, but, being a nonlinear hyperbolic system, we can expect the development of discontinuities in the derivatives of ζ and U. The classical procedure is then to introduce shocks, given by

$$-S[\zeta] + [HU] = 0, \quad -S[HU] + [HU^2 + \tfrac{1}{2}H^2] = 0. \tag{1.4a,b}$$

Here S is the shock speed, and $[\cdots]$ denotes the jump across the shock. In the absence of the bumps ($f(x) = 0$), these classical shocks conserve mass and momentum.

In the transcritical regime when $Fr \approx 1$, it will be useful also to consider a weakly nonlinear model for small-amplitude topography, given by

$$-\zeta_t - \Delta\zeta_x + \tfrac{3}{2}\zeta\zeta_x + \tfrac{1}{2}f_x = 0, \quad \Delta = Fr - 1. \tag{1.5}$$

Here $U = Fr + u$ and $u \approx -\zeta$. The reduced model (1.5) can be seen as a dispersionless forced KdV equation; see the aforementioned references. For convenience, we present an alternative derivation in appendix A. The initial condition (1.3) is replaced by

$$\zeta = 0, \quad \text{at } t = 0. \tag{1.6}$$

In this weakly nonlinear limit, the shock conditions (1.4) reduce to

$$(S - \Delta)[\zeta] + \tfrac{3}{4}[\zeta^2] = 0. \tag{1.7}$$

This can also of course be directly deduced from (1.5).

2. Hydraulic flow

2.1. *Steady solutions*

Here we consider the hydraulic theory, and to begin with we review the well-known theory (see e.g. Baines 1995) for flow over a single obstacle. Then we will show how this can be extended to obtain analogous solutions for flow over two obstacles. Thus

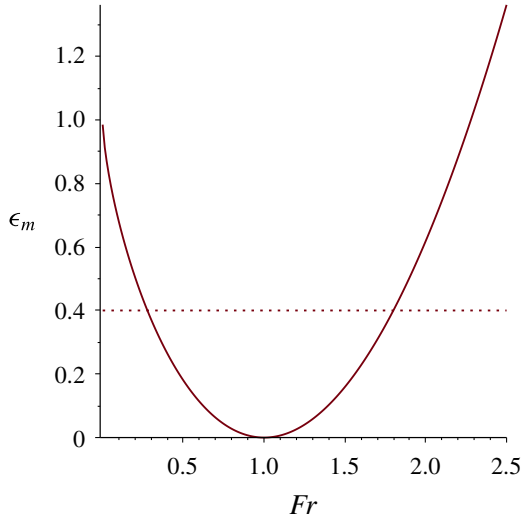

FIGURE 1. (Colour online) Plot of (2.3) at equality. The intersections of the line $\epsilon_m =$ const. with the curve (2.3) define $Fr_{b,p}$, respectively. The region below the curve defines the subcritical and supercritical regimes, and the region above the curve is the transcritical regime.

we seek steady solutions, so that, on omitting the time derivatives, (1.1) and (1.2) integrate to

$$HU = (1 + \zeta - f)U = Q, \quad \zeta + \tfrac{1}{2}U^2 = B. \tag{2.1a,b}$$

Here Q and B are positive integration constants, representing mass flux and energy flux, respectively (strictly, Q is volume flux, but we are assuming that the fluid density has been scaled to unity; and B is the Bernoulli constant, while BQ is the energy flux). Eliminating H or U gives

$$\frac{G^{4/3}}{2} + \frac{1}{G^{2/3}} = \frac{B + 1 - f}{Q^{2/3}}, \quad G = \frac{U}{H^{1/2}} = \frac{U^{3/2}}{Q^{1/2}} = \frac{Q}{H^{3/2}}, \tag{2.2a,b}$$

which determines the local Froude number G as a function of the obstacle height f.

For non-critical flow, this solution must connect smoothly to $U = Fr$, $\zeta = 0$, that is, $G = Fr$, at infinity, and so $Q = Fr$, $B = Fr^2/2$. Noting that then the right-hand side of the first expression in (2.2) has a minimum value of $3/2 - \epsilon_m$ when $Fr = 1$, it can be established that

$$0 < \epsilon_m < 1 + \frac{Fr^2}{2} - \frac{3Fr^{2/3}}{2}. \tag{2.3}$$

Here ϵ_m is the maximum obstacle height. This expression is plotted in figure 1 at equality (note that this is the curve BAE in figure 2.11 of Baines (1995)). It defines the subcritical regime $Fr < Fr_b < 1$ where $Fr < G < 1$, and the supercritical regime $1 < Fr_p < Fr$ where $1 < G < Fr$ and a smooth steady hydraulic solution exists. In the subcritical regime a localised depression forms over the obstacle, and in the supercritical regime a localised elevation forms over the obstacle. For small $(\epsilon_m)^{1/2} \ll 1$, recalling that $\Delta = Fr - 1$, we find that

$$\Delta_{p,b} = \pm\frac{(6\epsilon_m)^{1/2}}{2} + \frac{\epsilon_m}{4} + O\left(\epsilon_m^{3/2}\right). \tag{2.4}$$

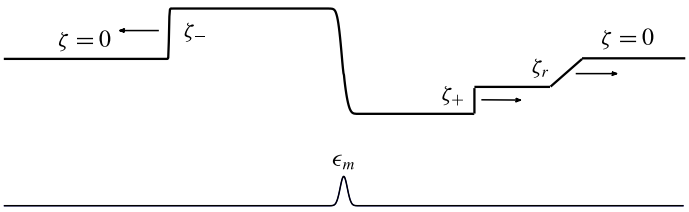

FIGURE 2. Schematic for closure using classical shocks.

In the transcritical regime $Fr_b < Fr < Fr_p$, (2.3) does not hold and is replaced by

$$\epsilon_m > 1 + \frac{Fr^2}{2} - \frac{3Fr^{2/3}}{2}. \tag{2.5}$$

Instead, we seek a solution which has upstream and downstream shocks propagating away from the obstacle, and which satisfies the critical flow condition at the top of the obstacle, that is, when $f = \epsilon_m$, $G_x \neq 0$. This condition implies that

$$G = 1, \quad \frac{3Q^{2/3}}{2} = B + 1 - \epsilon_m \quad \text{at } f = \epsilon_m. \tag{2.6a,b}$$

For a given ϵ_m, this relation defines B in terms of Q. At this critical location, $U = U_m = Q^{1/3}$ and $1 + \zeta_m - \epsilon_m = Q^{2/3}$. The local Froude number varies over the range $G_- < G < G_+$, where $+$ and $-$ denote the downstream and upstream values, respectively. It transpires that, in order for the shocks to propagate away from the obstacle, the flow is subcritical upstream where $G_- < G < 1$, $\zeta_- > \zeta > \zeta_m$, $U_- < U < U_m$, and supercritical downstream where $1 < G < G_+$, $\zeta_+ < \zeta < \zeta_m$, $U_+ > U > U_m$.

Before proceeding, we note that the expressions (2.2) hold both upstream and downstream, yielding the relationships

$$U_\pm (1 + \zeta_\pm)^{1/2} = Q, \quad \frac{U_\pm^2}{2} + \zeta_\pm = B, \tag{2.7a,b}$$

and so

$$\frac{U_\pm^2}{2} + \frac{Q}{U_\pm} = \frac{Q^2}{2(1+\zeta_\pm)^2} + \zeta_\pm + 1 = B + 1, \tag{2.8}$$

$$\frac{G_\pm^{4/3}}{2} + \frac{1}{G_\pm^{2/3}} = \frac{B+1}{Q^{2/3}}. \tag{2.9}$$

For given Q and B, these relations fix $U_\pm$ and $\zeta_\pm$ completely. But we have one relationship (2.6) connecting B and Q, and so there is just a single constant to determine. This is found using the classical shock closure described in the next section.

2.2. *Classical shock closure*

Outside the obstacle, $U = U_\pm$ and $\zeta = \zeta_\pm$ are constants, downstream and upstream, respectively, and are connected to the undisturbed values $U = Fr$ and $\zeta = 0$ far downstream and upstream, using classical shock closure based on the shock conditions (1.4); see figure 2. Since the steady hydraulic flow over the obstacle conserves mass and energy, rather than mass and momentum, these are non-trivial conditions to apply. Further, it transpires that we cannot simultaneously impose upstream and downstream jumps which connect directly to the uniform flow. Instead, we first

impose an upstream jump as specified by Baines (1995); see also El *et al.* (2009). There is then a downstream jump which connects to a rarefaction wave; see figure 2.

First we consider the upstream jump, which connects $\zeta_-,\ U_-$ to 0, Fr with $S_-<0$. The first relation in (1.4) gives

$$\zeta_-(S_- - U_-) = U_- - Fr \quad \text{or} \quad S_-\zeta_- = Q - Fr, \tag{2.10a,b}$$

and the second relation in (1.4) gives

$$(1+\zeta_-)(U_- - Fr)(S_- - U_-) = \zeta_-\left(1+\frac{\zeta_-}{2}\right). \tag{2.11}$$

Eliminating S_-, or $U_- - Fr$, yields the following expressions:

$$(1+\zeta_-)(U_- - Fr)^2 = \zeta_-^2\left(1+\frac{\zeta_-}{2}\right), \tag{2.12}$$

$$S_- = Fr - \left[(1+\zeta_-)\left(1+\frac{\zeta_-}{2}\right)\right]^{1/2}, \tag{2.13}$$

$$(1+\zeta_-)Fr - \zeta_-\left[(1+\zeta_-)\left(1+\frac{\zeta_-}{2}\right)\right]^{1/2} = Q. \tag{2.14}$$

Since we need $S_-<0$, it follows that we must have $\zeta_->0$ and $U_-<Q<Fr$. The system of equations is now closed, as the combination of (2.8) and (2.14) determines ζ_- in terms of B, so that finally all unknowns are obtained in terms of ϵ_m from (2.6). Further, the condition $\zeta_->0$ serves to define the transcritical regime (2.5) in terms of the Froude number Fr and ϵ_m.

Downstream, this procedure also determines $U_+>Fr,\ \zeta_+<0$, but, in general, this cannot be resolved by a jump directly to the state Fr, 0. Instead we must insert a right-propagating rarefaction wave; see figure 2. The rarefaction wave propagates downstream into the undisturbed state 0, Fr, and so is defined by the values U_r and ζ_r where

$$U_r - 2(1+\zeta_r)^{1/2} = Fr - 2. \tag{2.15}$$

It is then connected to the hydraulic downstream state $U_+,\ \zeta_+$ by a shock, using the jump conditions (1.4) to connect the two states through a shock with speed $S_+>0$. There are then three equations for the three unknowns $\zeta_r,\ U_r,\ S_+$ and the system is closed.

In the weakly nonlinear regime, when the forcing is sufficiently small (the appropriate small parameter is $\alpha\sim\sqrt{\epsilon_m}$), the rarefaction wave contribution can be neglected, as it has an amplitude of order α^3 while the shock intensity is $O(\alpha)$. In this limit we can solve the system of equations by an expansion in α and find that

$$3\zeta_\pm = 2\Delta \mp (6\epsilon_m+\beta_\pm)^{1/2} + O(\alpha^3), \quad \beta_\pm = 3\zeta_\pm^3 - 2\zeta_\pm\Delta^2 + \frac{4\Delta^3}{9}, \tag{2.16a,b}$$

$$\left.\begin{gathered} S_\pm = \Delta - \frac{3\zeta_\pm}{4} + \frac{\zeta_\pm^2}{32} + O(\alpha^3), \quad G_\pm = 1+\Delta-\frac{3\zeta_\pm}{2}+\gamma_\pm + O(\alpha^3), \\ \gamma_\pm = \frac{9\zeta_\pm^2}{8} - \frac{\zeta_\pm\Delta}{2}, \end{gathered}\right\} \tag{2.17}$$

$$Q = 1+\Delta+\zeta_\pm\Delta - \frac{3\zeta_\pm^2}{4} + O(\alpha^3). \tag{2.18}$$

Here $\beta_\pm = O(\alpha^3)$ and $\gamma_\pm = O(\alpha^2)$ are small correction terms, which if needed explicitly can be evaluated to leading order using the leading-order solution for $\zeta_\pm$. It is useful to note here that using (2.16) and (2.4), the local Froude numbers

$$G_\pm = 1 \pm \frac{(6\epsilon_m)^{1/2}}{2} + O(\alpha^2) = 1 + \Delta_{p,b} + O(\alpha^2) \tag{2.19}$$

and are independent of Δ at the leading order in α. Also, since the transcritical regime is defined by $\Delta_s < \Delta < \Delta_p$, it follows that, at the leading order in α, the local downstream and upstream Froude numbers $G_\pm$ are outside this transcritical regime, and hence the downstream and upstream flows are indeed fully supercritical and subcritical, respectively.

2.3. *Two obstacles*

The same procedure can now be followed when there are two widely separated obstacles. Based on our numerical simulations reported in § 3, the solution evolves in two stages. In the first stage, the theory described above can be applied to each obstacle separately. Then in the second stage, when the downstream-propagating waves emitted by the first obstacle interact with the upstream-propagating waves emitted by the first obstacle, an interaction takes place and there is an adjustment to a new configuration. There are several scenarios depending on the obstacle heights $\epsilon_{1,2}$ and the Froude number Fr. For instance, if both obstacles satisfy the condition (2.3) for subcritical or supercritical flow, then the solutions obtained for each obstacle separately will again be obtained. On the other hand, if both obstacles satisfy the condition (2.5) for transcritical flow, then at the end of the first stage a downstream depression shock preceded by a rarefaction wave emitted by the first obstacle will meet an upstream elevation shock emitted by the second obstacle. Our numerical simulations show that these generate a new shock between the obstacles. The speed S_{int} of this shock can be found from (1.4) where the conservation of mass law implies that

$$S_{int}(\zeta_{2-} - \zeta_{1+}) = (1 + \zeta_{2-})U_{2-} - (1 + \zeta_{1+})U_{1+} + O(\alpha^3) = Q_2 - Q_1 + O(\alpha^3). \tag{2.20}$$

Here the $O(\alpha^3)$ error is due to the presence of the rarefaction wave. Since $\zeta_{2-} > 0 > \zeta_{1+}$, the shock moves in the positive or negative direction depending on whether $Q_2 > (<)\, Q_1$. Indeed, using the expressions (2.17) and (2.14),

$$S_{int} = \Delta - \tfrac{3}{4}(\zeta_{1+} + \zeta_{2-}) + O(\alpha^2) = \tfrac{1}{4}[(6\epsilon_1)^{1/2} - (6\epsilon_2)^{1/2}] + O(\alpha^2) \tag{2.21}$$

and is independent of Δ to this order. Thus, this shock will move towards the higher of the two obstacles, that is, S_{int} is positive or negative according to whether $\epsilon_1 > \epsilon_2$ or $\epsilon_1 < \epsilon_2$, respectively. This is followed by the interaction of this shock with either the second or first obstacle, followed eventually by an adjustment to a final localised steady state encompassing both obstacles; this is the second stage.

The final localised steady hydraulic state can now be determined as before, with the criterion that criticality occurs at the higher obstacle so that the formulae in §§ 2.1 and 2.2 apply with $\epsilon_m = \max[\epsilon_1, \epsilon_2]$, the same as if the combination of the two obstacles was a single obstacle. Indeed, the criticality determined at the first stage at the higher obstacle persists into the second stage, while the flow at the lower

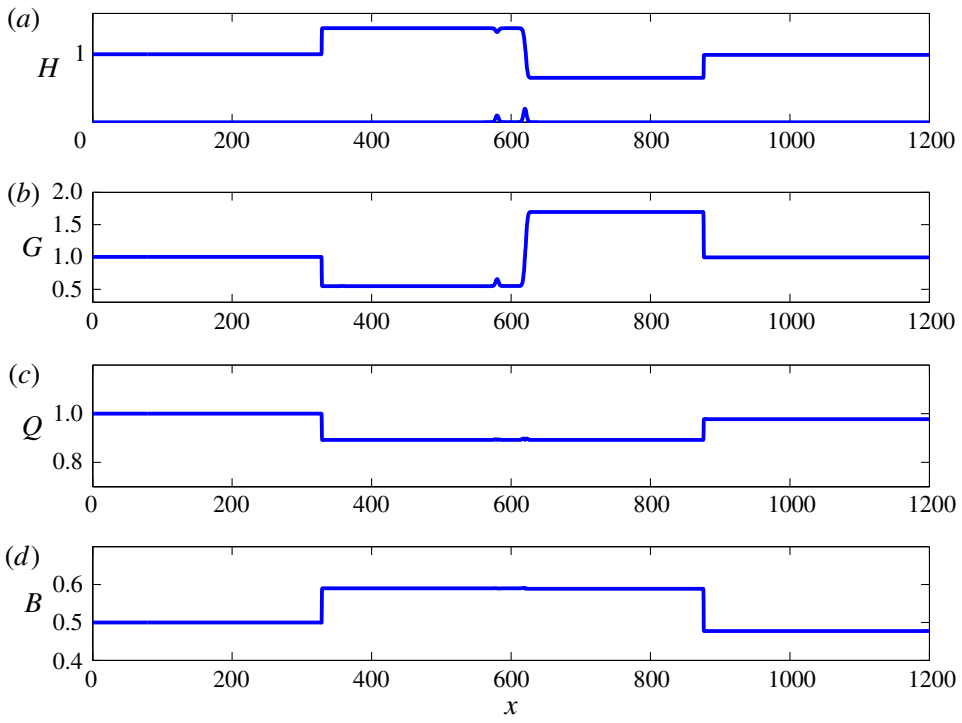

FIGURE 3. (Colour online) Hydraulic solution for the case $Fr = 1$ and unequal obstacle heights $\epsilon_1 = 0.1$, $\epsilon_2 = 0.2$. In the steady region over both obstacles, $Q = 0.8923$ and $B = 0.5900$, and $G = 0.6584$ at the crest of the first obstacle where the flow is locally subcritical.

obstacle adjusts in the second stage to be locally subcritical if the lower obstacle is the first obstacle, or is locally supercritical if the lower obstacle is the second obstacle. Illustrative examples taken from the numerical simulations are shown in figures 3 and 4, respectively. Note that criticality is controlled by the higher obstacle which has the same height in the two cases, and hence the same constant values of Q and B are generated in the region containing both obstacles.

When the obstacles have equal heights, $\epsilon_1 = \epsilon_2$, then also $Q_1 = Q_2$ and the shock speed $S_{int} = 0(\alpha^3)$, so that the error term in (2.20) is needed to determine the shock speed. This error term is due to the neglected rarefaction wave, and when this has a negative mass flux, as sketched in the scenario shown in figure 2, $S_{int} < 0$. The numerical solutions show that this is indeed the case. Hence it is then the second obstacle that controls criticality. An example taken from our numerical simulations is shown in figure 5. In the region over both obstacles combined, there is a steady state with constant values of Q and B satisfying the relation (2.6). The local Froude number $G = 1$ at the crest of the second obstacle, where G passes smoothly from subcritical $G < 1$ to supercritical $G > 1$. The flow is subcritical over the first obstacle, but $G = 1$ at the crest of the first obstacle. At this location there is a discontinuity in the slope of G, and hence also in the slopes of U and H, but all quantities are continuous. This can be deduced from (2.2) and (2.6) where near the crest of either obstacle

$$(G-1)^2 \approx \frac{3(\epsilon_m - f)}{2Q^{2/3}}. \tag{2.22}$$

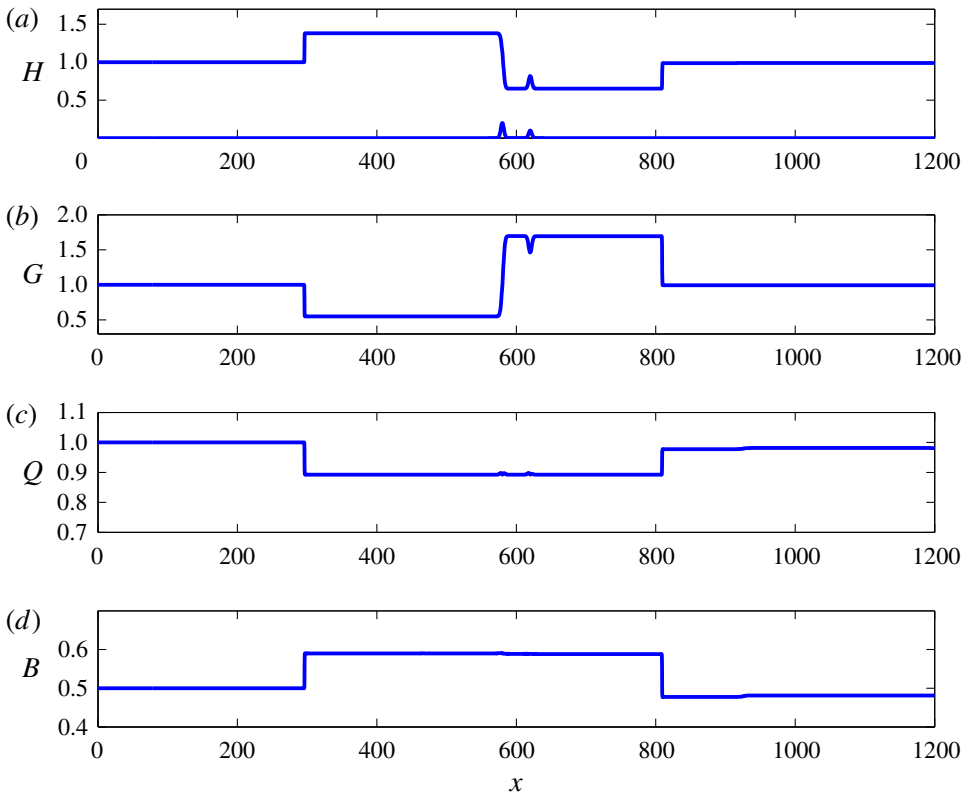

FIGURE 4. (Colour online) Hydraulic solution for the case $Fr = 1$ and unequal obstacle heights $\epsilon_1 = 0.2$, $\epsilon_2 = 0.1$. In the steady region over both obstacles, $Q = 0.8923$ and $B = 0.5900$, and $G = 1.463$ at the crest of the second obstacle where the flow is locally supercritical.

There are two possible solutions. We consider for simplicity the generic case when $\epsilon_m - f \approx \delta(x \pm L)^2$, $\delta > 0$. Then at the second obstacle there is a smooth solution for which $G - 1 \approx C(x - L)$, $C = \sqrt{3\delta/2Q^{2/3}}$, but at the first obstacle the solution is $1 - G \approx C|x + L|$, which is continuous but has a discontinuous slope. This can be regarded as a stationary contact discontinuity. This scenario is asymmetrical and so differs from those considered by Pratt (1984), who examined only symmetrical configurations and showed that these could not be stable. Further, he pointed out that it is not possible to construct a steady stable solution using a stationary shock, as this would then dissipate energy (see the last paragraph of his § 1 and footnote on p. 1216).

2.4. *Reduced model*

Before presenting the numerical results, it is useful to examine the same scenario as presented above in §§ 2.1–2.3 using the reduced model, especially as then the initial value problem can be solved (see e.g. Grimshaw & Smyth 1986; Grimshaw 2010). With the initial condition that $\zeta = 0$ at $t = 0$, (1.5) can be solved using characteristics,

$$\left.\begin{aligned} &\frac{\mathrm{d}x}{\mathrm{d}t} = \Delta - \frac{3\zeta}{2}, \quad \frac{\mathrm{d}\zeta}{\mathrm{d}t} = \frac{f_x}{2}, \\ &x = x_0, \quad \zeta = 0, \quad \text{at } t = 0. \end{aligned}\right\} \tag{2.23}$$

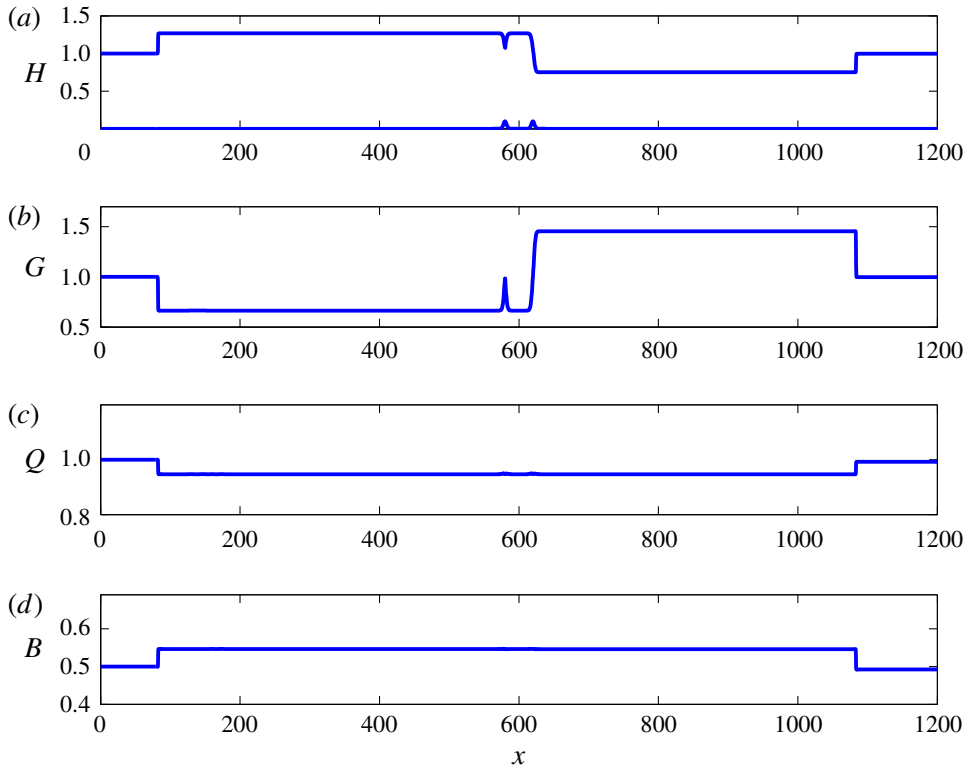

FIGURE 5. (Colour online) Hydraulic solution for the case $Fr = 1$ and equal obstacle heights $\epsilon_1 = \epsilon_2 = 0.1$. In the steady region over both obstacles, $Q = 0.9469$ and $B = 0.5464$, and $G = 1$ at the crest of the first obstacle, but $G < 1$ in the vicinity of the first obstacle where the flow is locally subcritical.

The system (2.23) can be integrated to yield

$$\Delta\zeta - \frac{3\zeta^2}{4} = \frac{1}{2}(f(x) - f(x_0)), \tag{2.24a}$$

$$3\zeta = 2\Delta \mp \Delta\{4\Delta^2 + 6[f(x_0) - f(x)]\}^{1/2}. \tag{2.24b}$$

Here the upper sign is chosen until the characteristic reaches a turning point where $2\Delta = 3\zeta$ and then the lower sign is chosen. When $\Delta = 0$ the upper (lower) sign is chosen on the left-hand (right-hand) side of the maximum point where $f = \epsilon_m$. Where characteristics intersect, a shock forms with speed S, given by (1.7) Then when

$$2\Delta^2 < 3\epsilon_{1,2} \tag{2.25}$$

there is a critical x_{0c} for each obstacle such that all characteristics with $x_0 < x_{0c}$ have a turning point, propagate upstream and form an upstream shock. Otherwise all characteristics with $x_0 > x_{0c}$ have no turning points, propagate downstream and form a downstream shock. The critical point is defined by $3f(x_{0c}) = 3\epsilon_{1,2} - 2\Delta^2$. Then, in the first stage, a steady solution will emerge over each obstacle, terminated by upstream and downstream shocks, determined by that characteristic emanating from x_{0c} and the corresponding steady solution is found using (2.24*a*),

$$4\Delta^2 - 12\Delta\zeta + 9\zeta^2 = 6(\epsilon_m - f(x)), \tag{2.26a}$$

$$3\zeta = 2\Delta \mp \text{sign}[x \mp L]\{6[\epsilon_m - f(x)]\}^{1/2}. \tag{2.26b}$$

The upstream (downstream) shock has a magnitude $\zeta_{\mp}$, where

$$3\zeta_{\mp} = 2\Delta \pm \{6\epsilon_m\}^{1/2}, \tag{2.27}$$

respectively. Note that $\zeta_+ > 0$ and $\zeta_- < 0$ so that the upstream shock is elevation and the downstream shock is depression. The speeds of these shocks are found from (1.7), that is,

$$4S_{\mp} = 2\Delta \mp \{6\epsilon_m\}^{1/2} \tag{2.28}$$

and $S_- < 0$, $S_+ > 0$, while the local Froude number is

$$G = 1 + \Delta - 3\zeta/2 \quad \text{and so} \quad G_{\mp} = 1 \mp \frac{\{6\epsilon_m\}^{1/2}}{2}. \tag{2.29a,b}$$

In the first stage, this local steady solution holds only for each obstacle separately. When there are two obstacles, the upstream elevation shock from the obstacle will meet the downstream depression shock from the obstacle. This generates a new shock, with speed

$$S_{int} = \Delta - \tfrac{3}{4}(\zeta_{1+} + \zeta_{2-}) = \tfrac{1}{4}[(6\epsilon_1)^{1/2} - (6\epsilon_2)^{1/2}], \tag{2.30}$$

which is independent of Δ, and is positive or negative according to whether $\epsilon_1 > \epsilon_2$ or $\epsilon_1 < \epsilon_2$, respectively. These results all agree with the small-amplitude limits of the corresponding expressions in the preceding subsections.

3. Numerical results

3.1. *Numerical method*

The nonlinear shallow-water equations (1.1) and (1.2) can be written as

$$\mathscr{U}_t + \mathscr{F}_x = \mathscr{G}, \tag{3.1}$$

where $\mathscr{U}$, $\mathscr{F}$ and $\mathscr{G}$ represent the density vector, flux vector and source term, respectively,

$$\mathscr{U} = \begin{bmatrix} H \\ UH \end{bmatrix}, \quad \mathscr{F} = \begin{bmatrix} UH \\ HU^2 + H^2/2 \end{bmatrix}, \quad \mathscr{G} = \begin{bmatrix} 0 \\ -Hf_x \end{bmatrix}. \tag{3.2a–c}$$

The computational domain, $0 < x < x_L$, is discretised by uniform cell size Δx. The cell centre is denoted by x_i, where $x_{i-1/2}$ and $x_{i+1/2}$ refer the left and the right cell interface, respectively.

In discretisation form, (3.1) can be written as

$$\frac{\mathscr{U}_i^{n+1} - \mathscr{U}_i^n}{\Delta t} + \frac{\mathscr{F}_{i+1/2}^n - \mathscr{F}_{i-1/2}^n}{\Delta x} = \mathscr{G}_i^n. \tag{3.3}$$

Superscript n refers to the time-step level. The gradient of the flux function is approximated by the difference of numerical fluxes at the left, $\mathscr{F}_{i-1/2}^n$, and the right, $\mathscr{F}_{i+1/2}^n$, of cell interfaces, respectively. At the cell interface $i + 1/2$,

$$\mathscr{F}_{i+1/2}^n = \mathscr{F}(\mathscr{U}_{i+1/2-}^n, \mathscr{U}_{i+1/2+}^n). \tag{3.4}$$

Numerical flux at the cell interface is a function of an unknown variable on the left and the right limits, and

$$\mathscr{U}^n_{i+1/2-} = \begin{bmatrix} H^n_{i+1/2-} \\ H^n_{i+1/2-} U_i^{n^2} \end{bmatrix}, \quad \mathscr{U}^n_{i+1/2+} = \begin{bmatrix} H^n_{i+1/2+} \\ H^n_{i+1/2+} U_{i+1}^{n^2} \end{bmatrix}. \tag{3.5a,b}$$

Applying the hydrostatic reconstruction from Audusse *et al.* (2004),

$$H^n_{i+1/2-} = \max(0, H_i + f_i - f_{i+1/2}) \quad \text{and} \quad H^n_{i+1/2+} = \max(0, H_{i+1} + f_{i+1} - f_{i+1/2}). \tag{3.6a,b}$$

Bottom slope is now included in the reconstruction of water depth. The value of bottom height at the corresponding interface is approximated by upwind evaluation,

$$f_{i+1/2} = \max(f_i, f_{i+1}). \tag{3.7}$$

To obtain a well-balanced scheme, the gradient of source term and flux difference must be balanced at steady state (Audusse *et al.* 2004), so (3.3) can be rewritten as

$$\frac{\mathscr{U}_i^{n+1} - \mathscr{U}_i^n}{\Delta t} + \frac{\mathscr{F}_l^n(\mathscr{U}_i^n, \mathscr{U}_{i+1}^n, f_i, f_{i+1}) - \mathscr{F}_r^n(\mathscr{U}_{i-1}^n, \mathscr{U}_i^n, f_{i-1}, f_i)}{\Delta x} = 0, \tag{3.8}$$

with modified numerical fluxes

$$\mathscr{F}_l^n(\mathscr{U}_i^n, \mathscr{U}_{i+1}^n, f_i, f_{i+1}) = \mathscr{F}(\mathscr{U}^n_{i+1/2-}, \mathscr{U}^n_{i+1/2+}) + [0, H_i^{n^2} - H^{n^2}_{i+1/2-}]/2, \tag{3.9a}$$

$$\mathscr{F}_r^n(\mathscr{U}_i^n, \mathscr{U}_{i+1}^n, f_i, f_{i+1}) = \mathscr{F}(\mathscr{U}^n_{i+1/2-}, \mathscr{U}^n_{i+1/2+}) + [0, H_{i+1}^{n^2} - H^{n^2}_{i+1/2+}]/2. \tag{3.9b}$$

In this work, we apply the weighted average flux (WAF) proposed by Toro (1992), Toro, Spruce & Speares (1994) and Siviglia & Toro (2009) to obtain the approximation of $\mathscr{F}(\mathscr{U}^n_{i+1/2-}, \mathscr{U}^n_{i+1/2+})$. We also apply the minmod flux limiter based on the total variation diminishing (TVD) proposed by Toro (1992) in our numerical scheme to remove spurious oscillations when simulating the moving shock problem.

In our simulations, we apply transmissive boundaries to allow waves to propagate outwards on both boundaries. The bottom elevation is assumed to be two Gaussian obstacles given by

$$f(x) = \epsilon_1 \exp(-(x - x_a)^2/w) + \epsilon_2 \exp(-(x - x_b)^2/w), \tag{3.10}$$

where ϵ_1 and ϵ_2 are the obstacle heights, x_a and $x_b = x_a + L$ are the centre locations of the first and the second obstacle, respectively, and the width of each obstacle is $w = 10$.

3.2. *Equal obstacle heights*

3.2.1. *The case* $\epsilon_1 = 0.1, \epsilon_2 = 0.1$

Simulations for a subcritical case $Fr = 0.5$ are shown in figure 6. Initially, in the first stage ($t = 50$), steady depression waves are produced over each obstacle, and small transient elevation waves travel upstream from each obstacle. In the second stage ($t = 70$), the transient wave from the second obstacle has passed over the first obstacle and proceeded upstream. In the final stage ($t = 300$), only the steady depression waves over each obstacle are left. In this case, the Froude number is outside the transcritical regime for both obstacles; see (2.3) and figure 1.

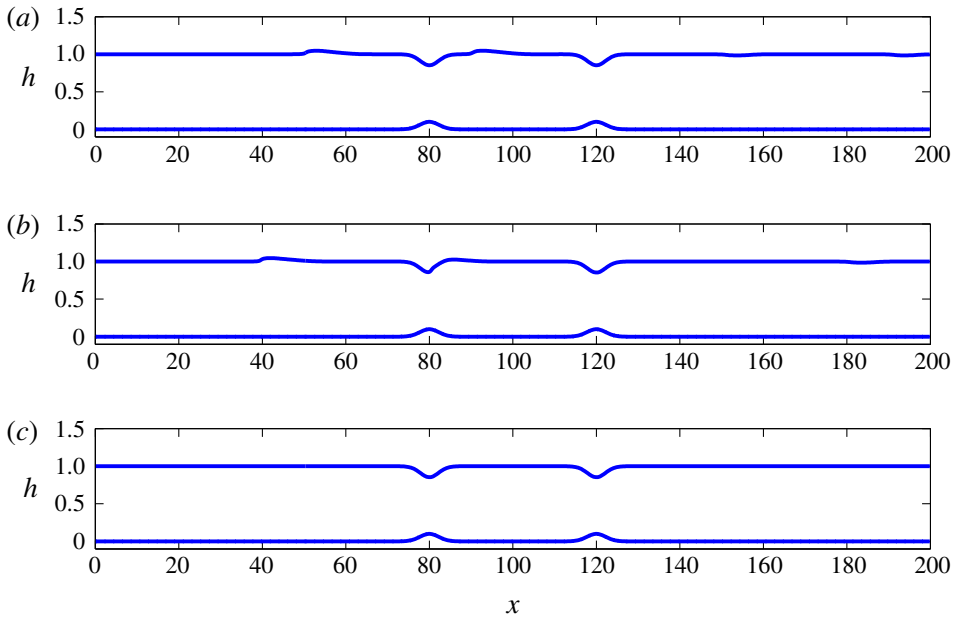

FIGURE 6. (Colour online) Simulations for $Fr = 0.5$, $\epsilon_1 = 0.1$, $\epsilon_2 = 0.1$: (*a*) $t = 50$; (*b*) $t = 70$; and (*c*) $t = 300$.

Simulations for a transcritical flow case $Fr = 1$ are shown in figure 7. In the first stage ($t = 50$), a transcritical flow is generated over each obstacle separately, consisting of an elevation shock propagating upstream connected by a steady solution to a depression shock propagating downstream. The depression shock from the first obstacle meets the elevation shock from the second obstacle at around $t = 130$ forming a single shock, which then propagates upstream. In the second stage ($t = 400$), there is an adjustment in which a locally steady subcritical depression wave forms over the first obstacle, while a locally steady transcritical flow forms over the second obstacle. At the same time, the elevation shock and depression shock outside both obstacles continue to propagate in their separate ways. As time increases ($t = 1000$), the flow over both obstacles reaches a locally steady state with criticality controlled by the second obstacle.

Next, we examine a quantitative comparison between the nonlinear shallow-water simulations and the theoretical results from the reduced model presented in § 3.2. From the numerical simulations shown in figure 7 over the time range $t = 400$–1000, we find that the respective shock magnitudes and speeds are $\zeta_+ = -0.2574$, $\zeta_- = 0.2670$, $S_+ = 0.1880$, $S_- = -0.1980$. With $\epsilon_m = 0.1$ the local Froude numbers in (2.29) are $G_+ = 1.3873$, $G_- = 0.6127$, while the shock magnitudes from (2.27) are $\zeta_+ = -0.2582$, $\zeta_- = 0.2582$, and the shock speeds from (2.28) are $S_+ = 0.1937$, $S_- = -0.1937$. These values are in reasonable agreement with the numerically determined values. Using the more exact formulae (2.16) and (2.17) up to the $O(\alpha^2)$ terms leads to $\zeta_+ = -0.2468$, $\zeta_- = 0.2691$ and $S_+ = 0.1871$, $S_- = -0.1996$, which is an improvement. Note that the effective small parameter here is $(6\epsilon_m)^{1/2} = 0.7746$ and so is not small enough for the reduced model to be completely accurate.

Simulations for a supercritical flow case $Fr = 1.5$ are shown in figure 8. Initially, in the first stage ($t = 30$), steady elevation waves are produced over each obstacle, and small transient depression waves travel downstream from each obstacle. At the beginning of the second stage ($t = 70$), the transient wave from the first obstacle passes

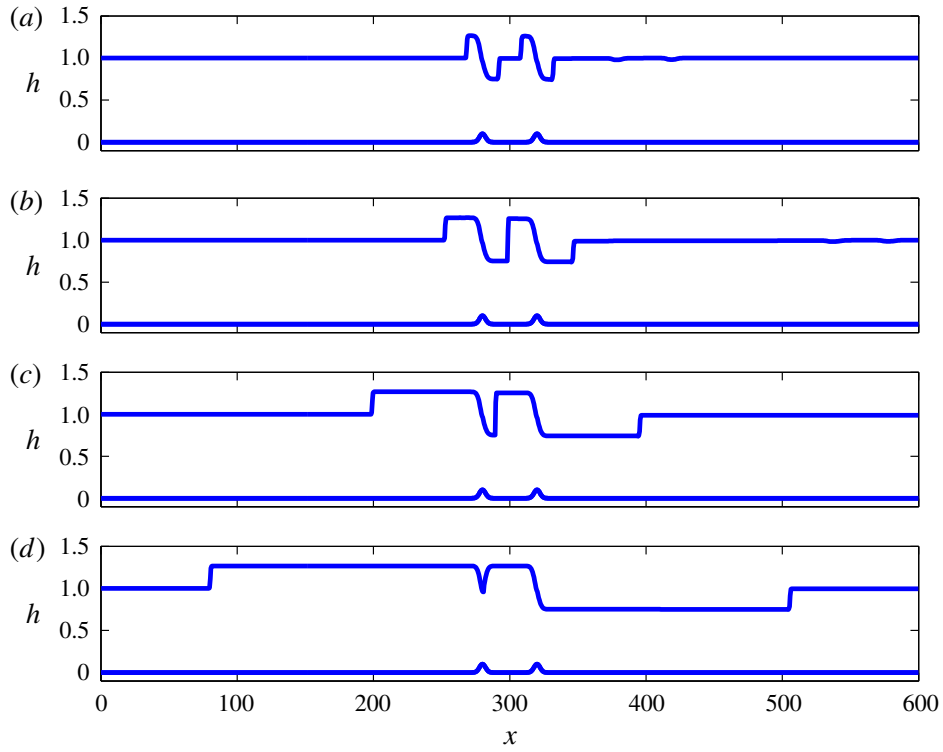

FIGURE 7. (Colour online) Simulations for $Fr = 1.0$, $\epsilon_1 = 0.1$, $\epsilon_2 = 0.1$: (*a*) $t = 50$; (*b*) $t = 130$; (*c*) $t = 400$; and (*d*) $t = 1000$.

over the second obstacle and proceeds upstream. In the final stage ($t = 400$), only the steady elevation waves over each obstacle are left. In this case, the Froude number is outside the transcritical regime for both obstacles; see (2.3) and figure 1.

It should be noted that, in the reduced model, the local Froude number (2.29) satisfies $0.6127 < G < 1.3873$ for $\epsilon_m = 0.1$. This prediction is consistent with the nonlinear simulations shown in figure 6 for subcritical flow, in figure 7 for transcritical flow and in figure 8 for supercritical flow.

3.2.2. *The case* $\epsilon_1 = 0.2$, $\epsilon_2 = 0.2$

Four simulations for $Fr = 0.5,\ 1.0,\ 1.5,\ 2.0$ are shown in figures 9–12. When $\epsilon_m = 0.2$, transcritical flow occurs in the range of $0.48 < Fr < 1.56$; see (2.3) and figure 1. The reduced model predicts transcritical flow when $0.45 < Fr < 1.55$; see (2.4). Thus the flow is slightly transcritical for $Fr = 0.5$ and 1.5, respectively nearly subcritical or supercritical, while it is transcritical for $Fr = 1.0$, and supercritical for $Fr = 2.0$. In all cases we expect the reduced model to provide quite good interpretation.

The nearly subcritical case shown in figure 9 can be compared with the subcritical case shown in figure 6 for $\epsilon_1 = \epsilon_2 = 0.1$. Although the first stage ($t = 30, 60$) is similar, there are now visible two small rarefaction waves propagating to the left, and in the second stage ($t = 130, 800$) a pronounced asymmetry develops with a larger depression wave over the second obstacle. This is due to this case being in the transcritical regime, and hence the second obstacle controls criticality.

The transcritical case shown in figure 10 is qualitatively similar to that in figure 7 for $\epsilon_1 = 0.1$, $\epsilon_2 = 0.1$. From the numerical simulations shown in figure 7 over the time range $t = 40$–800, we find that the respective shock magnitudes and speeds are $\zeta_+ =$

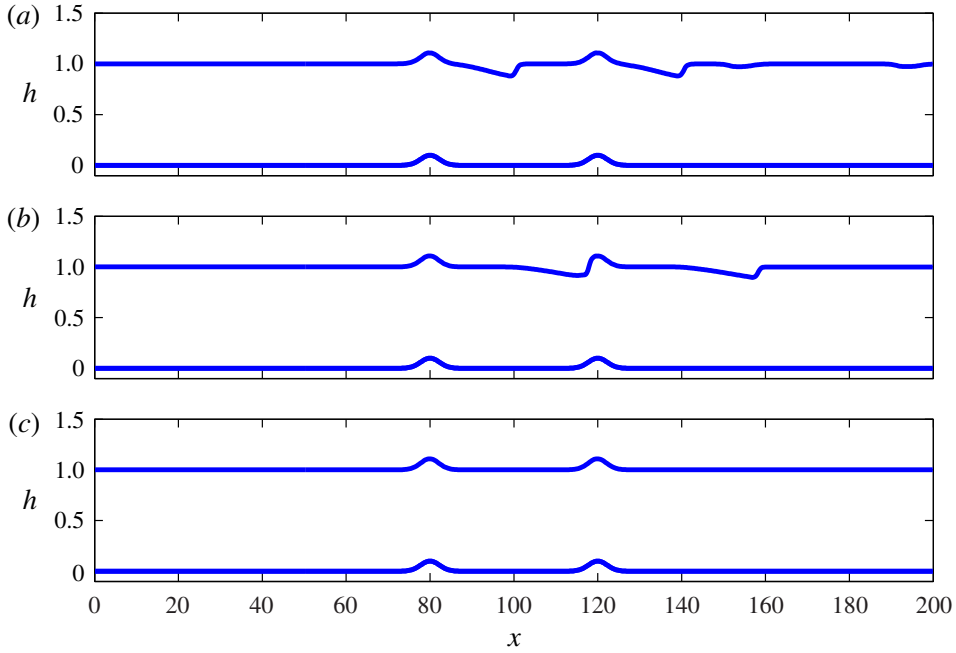

FIGURE 8. (Colour online) Simulations for $Fr = 1.5$, $\epsilon_1 = 0.1$, $\epsilon_2 = 0.1$: (*a*) $t = 30$; (*b*) $t = 60$; and (*c*) $t = 400$.

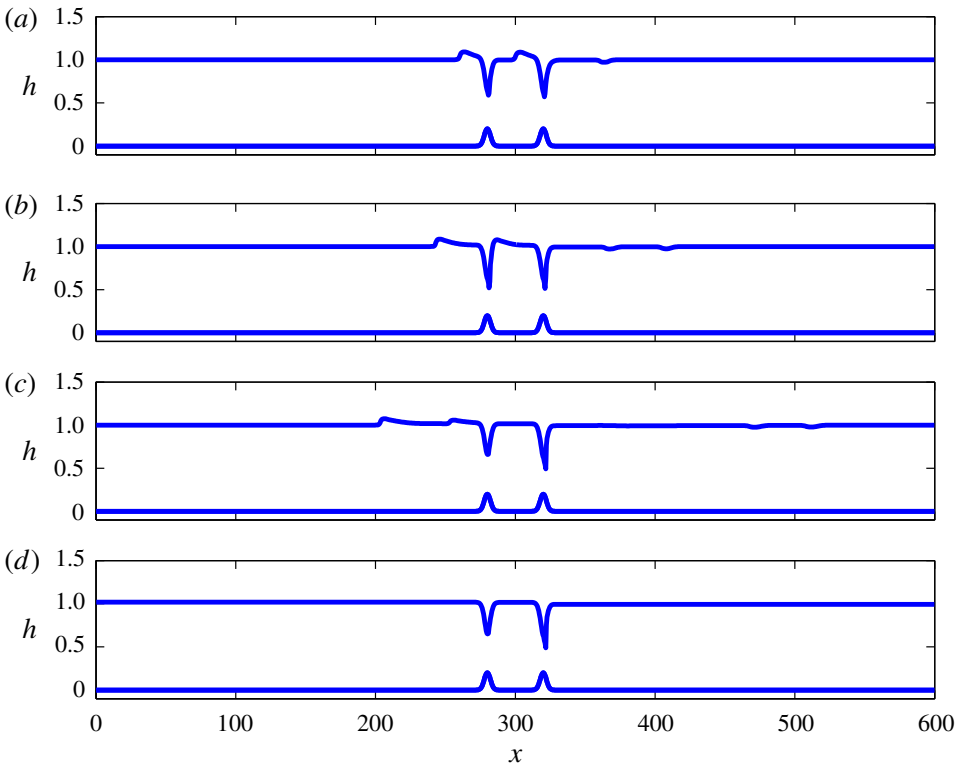

FIGURE 9. (Colour online) Simulations for $Fr = 0.5$, $\epsilon_1 = 0.2$, $\epsilon_2 = 0.2$: (*a*) $t = 30$; (*b*) $t = 60$; (*c*) $t = 130$; and (*d*) $t = 800$.

-0.3600, $\zeta_- = 0.3810$, $S_+ = 0.2535$, $S_- = -0.2814$. With $\epsilon_m = 0.2$ the local Froude numbers in (2.29) are $G_+ = 1.5477$ and $G_- = 0.4523$, while the shock magnitudes from (2.27) are $\zeta_+ = -0.3651$ and $\zeta_- = 0.3651$, and the shock speeds from (2.28) are

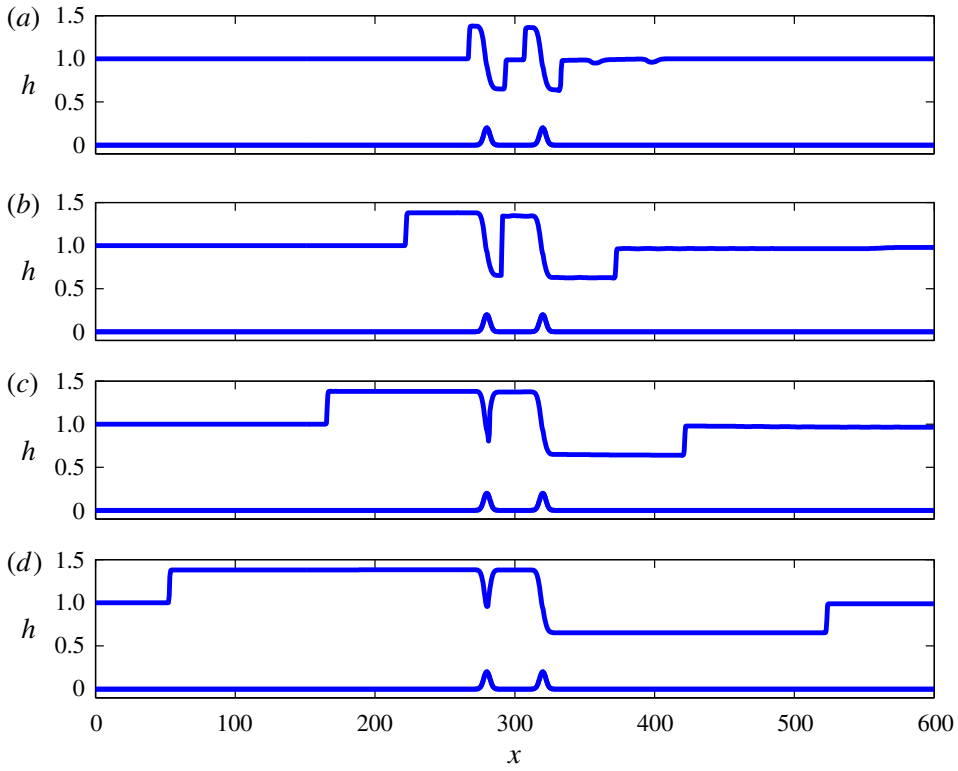

FIGURE 10. (Colour online) Simulations for $Fr = 1.0$, $\epsilon_1 = 0.2$, $\epsilon_2 = 0.2$: (*a*) $t = 40$; (*b*) $t = 200$; (*c*) $t = 400$; and (*d*) $t = 800$.

$S_+ = 0.2739$ and $S_- = -0.2739$. These values are in reasonable agreement with the numerically determined values. Using the more exact formulae (2.16) and (2.17) up to the $O(\alpha^2)$ terms leads to $\zeta_+ = -0.3422$, $\zeta_- = 0.3867$ and $S_+ = 0.2603$, $S_- = -0.2853$, which is overall some improvement. But note here that the effective small parameter is $(6\epsilon_m)^{1/2} = 1.0954$ and can hardly be considered small.

The nearly supercritical case shown in figure 11 can be compared with the supercritical case shown in figure 8 for $\epsilon_1 = \epsilon_2 = 0.1$. Although the first stage ($t = 300$) is rather similar, there is already an asymmetry in that the elevation wave over the second obstacle is already slightly smaller than that over the first obstacle, indicating that the adjustment process to the second obstacle is beginning. This adjustment continues at $t = 300$ and the final locally steady state is achieved at $t = 660$, 1200, in which there is criticality controlled by the second obstacle, and a locally subcritical flow over the first obstacle.

The fully supercritical case is shown in figure 12 and can also be compared with the supercritical case shown in figure 8 for $\epsilon_1 = \epsilon_2 = 0.1$. It is quite similar, although the time then to reach the second stage is much shorter.

3.3. *Unequal obstacle heights*

3.3.1. *The cases* $\epsilon_1 = 0.01$, $\epsilon_2 = 0.02$ *and* $\epsilon_1 = 0.1$, $\epsilon_2 = 0.2$

A transcritical case ($Fr = 1$) when the second obstacle is larger is shown in figure 13 for quite small amplitudes. At the first stage ($t = 50$), each obstacle generates elevation and depression shocks that can be described by the single-obstacle theory. As time increases ($t = 460$), the depression shock from the first obstacle interacts with the

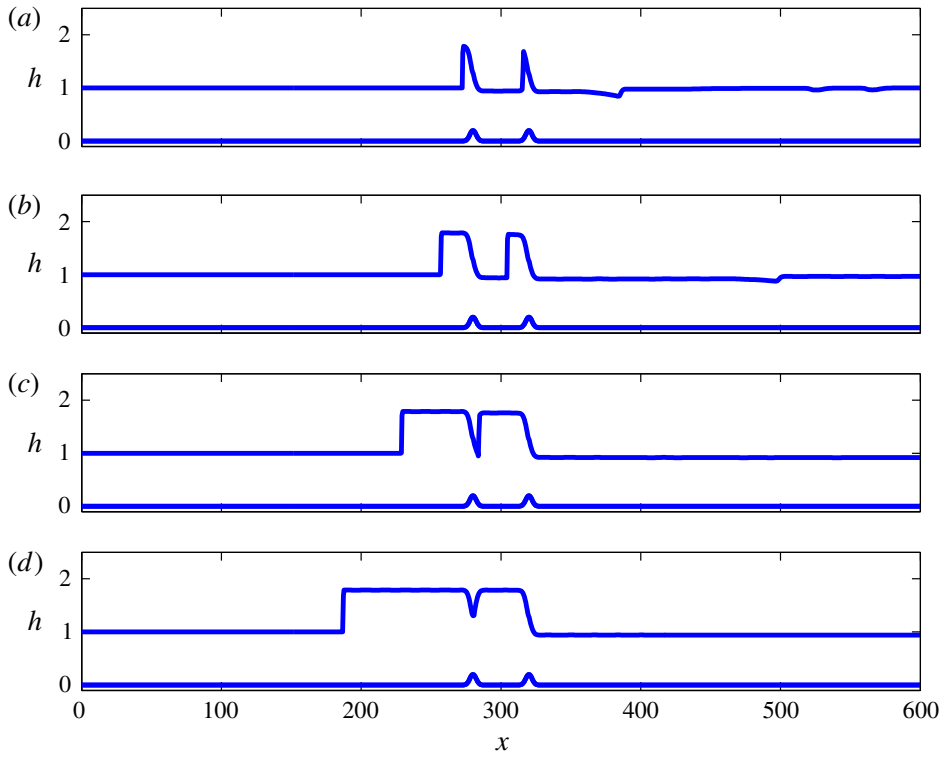

FIGURE 11. (Colour online) Simulations for $Fr = 1.5$, $\epsilon_1 = 0.2$, $\epsilon_2 = 0.2$: (*a*) $t = 100$; (*b*) $t = 300$; (*c*) $t = 660$; and (*d*) $t = 1200$.

upstream elevation shock generated by the second obstacle. A new shock is formed, called an intermediate shock as described in the analysis of § 2. Since the second obstacle is larger, the intermediate shock travels upstream and passes over the first obstacle, leaving a locally steady depression wave in a locally subcritical flow ($t = 1000$). The speed of the intermediate shock is greater than the speed of the travelling elevation shock from the first obstacle. These two shocks merge and finally form a new shock moving further upstream ($t = 1800$).

Next, we compare these nonlinear simulations quantitatively with theoretical results from § 2. For $\epsilon_1 = 0.01$, we find from the nonlinear simulations that the upstream shock magnitude and speed are $\zeta_- = 0.0822$ and $S_- = -0.0615$, while the reduced model predicts that $\zeta_- = 0.0816$ and $S_- = -0.0612$, and using the more exact formulae (2.16) and (2.17) leads to $\zeta_- = 0.0828$ and $S_- = -0.0619$. Similarly, for the second obstacle with $\epsilon_2 = 0.02$, the downstream shock magnitude and speed from the simulations are $\zeta_+ = 0.1134$ and $S_+ = 0.0847$ while the reduced model predicts that $\zeta_+ = -0.1155$ and $S_+ = 0.0866$, and using the more exact formulae (2.16) and (2.17) leads to $\zeta_+ = 0.1132$ and $S_+ = 0.0853$. These comparisons show very good agreement for these small-amplitude obstacles. Further, the intermediate shock speed from the simulation is $S_{int} = -0.0262$, while the theoretical expression (2.30) yields $S_{int} = -0.0254$. Also, note that for the nonlinear simulations when $t = 1000$–1800, the two upstream elevation shocks merge to form a new one with the new speed $S_- = -0.0867$, which is nearly the addition of S_{int} and S_- (for $\epsilon_1 = 0.01$).

A case with higher obstacle amplitudes, $\epsilon_1 = 0.1$, $\epsilon_2 = 0.2$, is shown in figure 14. The flow behaviour is quite similar to the smaller-amplitude case. Here the intermediate shock speed from the simulation is $S_{int} = -0.1286$, but from (2.30), $S_{int} = -0.0802$. The quite large difference is due to higher-order nonlinear effects.

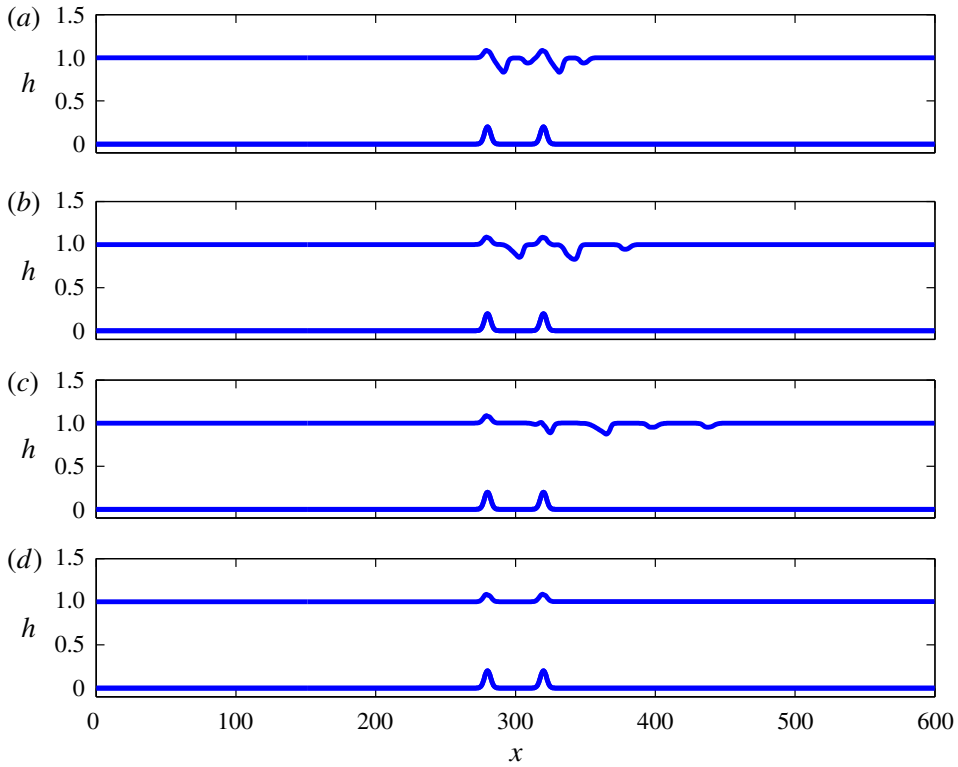

FIGURE 12. (Colour online) Simulations for $Fr = 2.0$, $\epsilon_1 = 0.2$, $\epsilon_2 = 0.2$: (*a*) $t = 10$; (*b*) $t = 20$; (*c*) $t = 40$; and (*d*) $t = 200$.

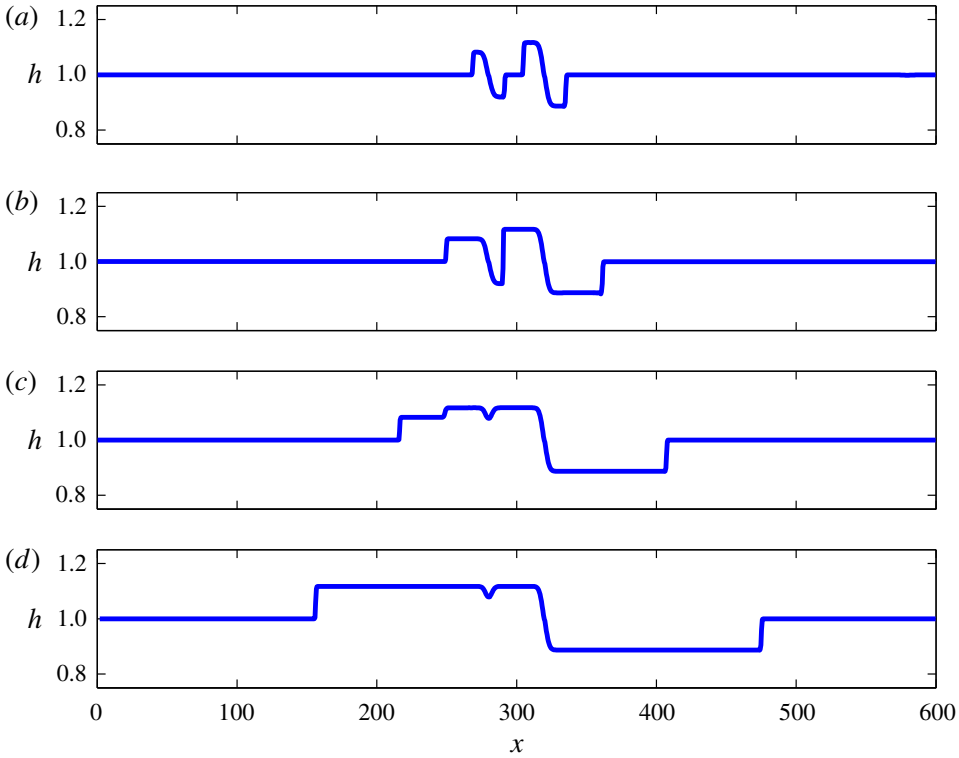

FIGURE 13. (Colour online) Simulations for $Fr = 1.0$, $\epsilon_1 = 0.01$, $\epsilon_2 = 0.02$: (*a*) $t = 150$; (*b*) $t = 460$; (*c*) $t = 1000$; and (*d*) $t = 1800$.

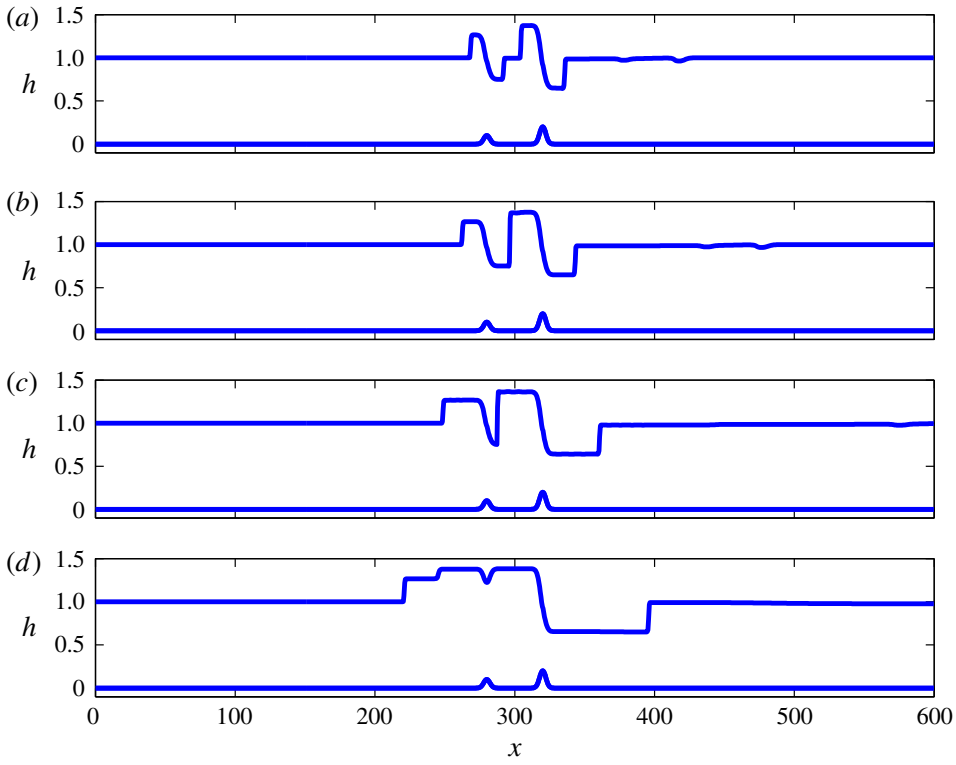

FIGURE 14. (Colour online) Simulations for $Fr = 1.0$, $\epsilon_1 = 0.1$, $\epsilon_2 = 0.2$: (*a*) $t = 50$; (*b*) $t = 80$; (*c*) $t = 150$; and (*d*) $t = 290$.

3.3.2. *The cases* $\epsilon_1 = 0.02$, $\epsilon_2 = 0.01$ *and* $\epsilon_1 = 0.2$, $\epsilon_2 = 0.1$

A transcritical case ($Fr = 1$) when the first obstacle is larger is shown in figure 15 for quite small amplitudes. At the first stage ($t = 150$), each obstacle generates elevation and depression shocks that can be described by the single-obstacle theory. As time increases ($t = 460$), the downstream depression shock from the first obstacle interacts with the upstream elevation shock generated by the second obstacle, and an intermediate shock is formed. Because the first obstacle is larger, it now controls criticality. The intermediate shock travels downstream and passes over the second obstacle, leaving a locally steady elevation wave ($t = 1400$) in a locally supercritical flow. The speed of the intermediate shock is greater than the speed of the downstream-travelling depression shock from the second obstacle. These two shocks merge and form a new shock moving further downstream ($t = 1800$).

Next, we compare these nonlinear simulations quantitatively with the theoretical results. For $\epsilon_1 = 0.02$, we find from the nonlinear simulations that the upstream shock magnitude and speed are $\zeta_- = 0.1170$ and $S_- = -0.0880$, while the reduced model predicts that $\zeta_- = 0.1155$ and $S_- = -0.0866$, and using the more exact formulae (2.16) and (2.17) leads to $\zeta_- = 0.1165$ and $S_- = -0.0870$. Similarly, for the second obstacle with $\epsilon_2 = 0.01$, the downstream shock magnitude and speed from the simulations are $\zeta_+ = -0.0811$ and $S_+ = 0.0607$, while the reduced model predicts that $\zeta_+ = -0.0816$ and $S_+ = 0.0612$, and using the more exact formulae (2.16) and (2.17) leads to $\zeta_- = 0.0802$ and $S_- = -0.0604$. These comparisons show very good agreement for small-amplitude obstacles. Further, the intermediate shock speed from the simulation is $S_{int} = 0.0260$, while the theoretical expression (2.30) yields $S_{int} = 0.0254$. Also, note that for the nonlinear simulations when $t = 1400$–1800, the two downstream depression shocks

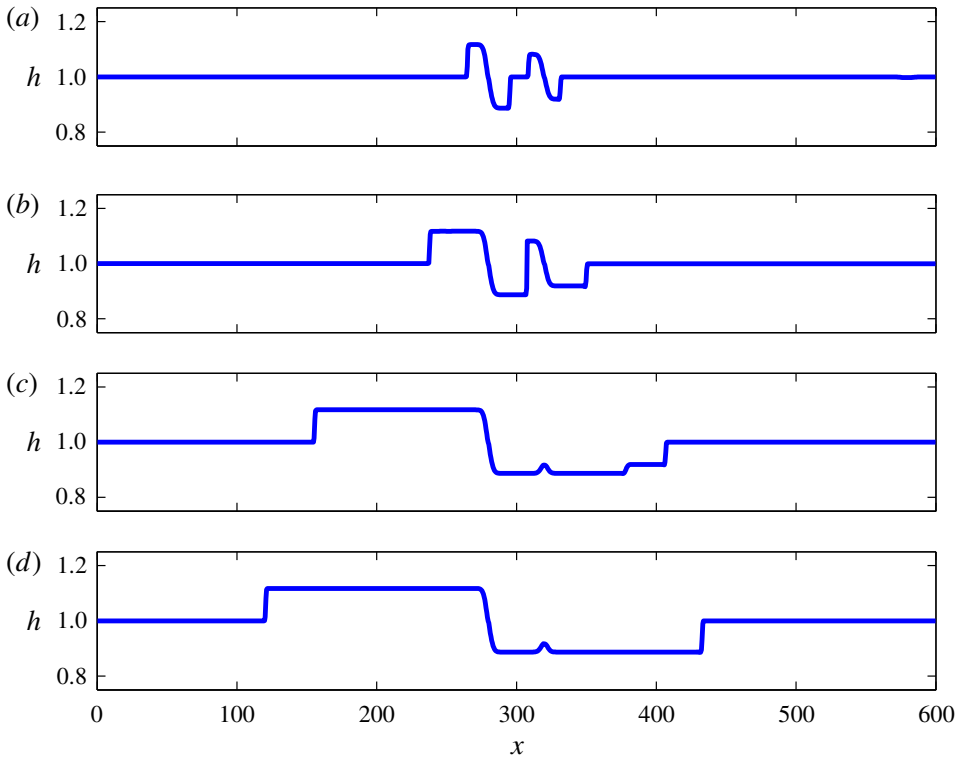

FIGURE 15. (Colour online) Simulations for $Fr = 1.0$, $\epsilon_1 = 0.02$, $\epsilon_2 = 0.01$: (*a*) $t = 150$; (*b*) $t = 460$; (*c*) $t = 1400$; and (*d*) $t = 1800$.

merge to form a new shock with the new speed $S_+ = 0.0812$, which is nearly the addition of S_{int} and S_+ (for $\epsilon = 0.01$).

A case with higher obstacle amplitudes, $\epsilon = 0.2$, $\epsilon_2 = 0.1$, is shown in figure 16. The flow behaviour is similar to the smaller-amplitude case. Here the intermediate shock speed from the simulation is $S_{int} = 0.0281$, but from (2.30), $S_{int} = 0.0802$. Again, the quite large difference is due to higher-order nonlinear effects.

4. Summary

Transcritical shallow-water flow over two localised and widely spaced obstacles has been examined using the fully nonlinear shallow-water equations (1.1) and (1.2) and with a combination of numerical simulations and theoretical analysis based on hydraulic flow concepts. For a single obstacle, the solution is typically a locally steady hydraulic flow over the obstacle contained between an upstream elevation shock and a downstream depression shock. For the case of two obstacles, there are two stages. At the first stage, each obstacle generates an upstream-propagating elevation shock and a downstream-propagating depression shock, each well described by the single-obstacle theory. Then, in the second stage, the downstream-propagating depression shock from the first obstacle interacts with the upstream-propagating elevation shock from the second obstacle to produce an intermediate shock, which propagates towards the larger obstacle, or, if the obstacles have equal heights, towards the second obstacle. There is an adjustment to a locally steady flow over both obstacles, where the higher obstacle controls criticality, or if the obstacles have equal heights, the second obstacle controls criticality. This outcome agrees with the analytical theory based on hydraulic flow concepts extended here from a single obstacle to two obstacles.

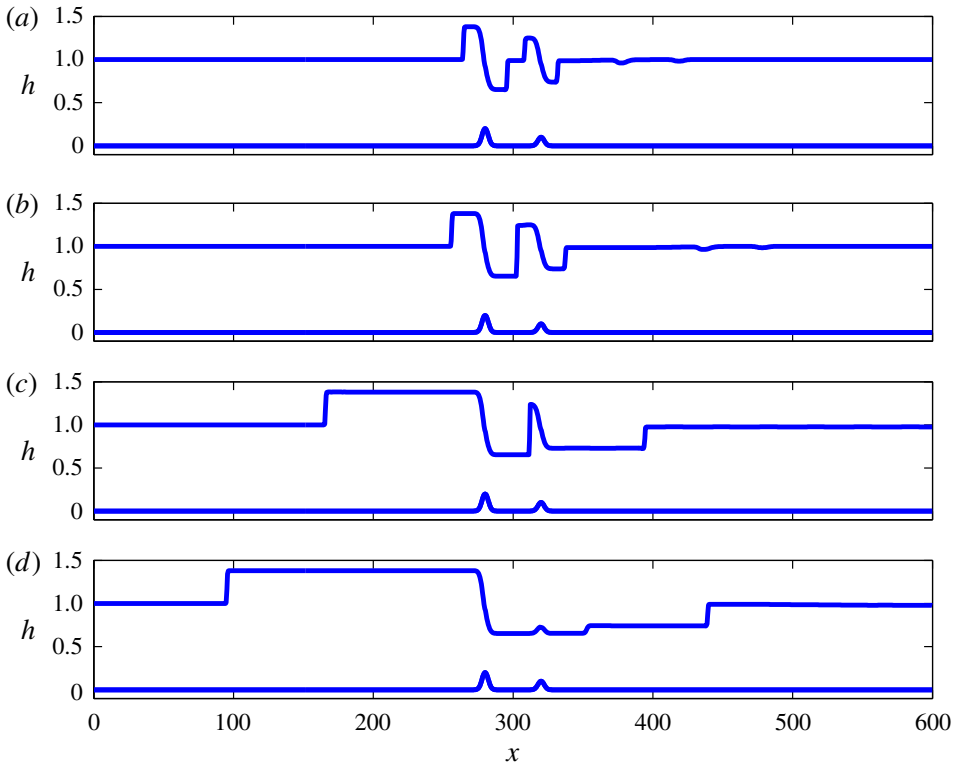

FIGURE 16. (Colour online) Simulations for $Fr = 1.0$, $\epsilon_1 = 0.2$, $\epsilon_2 = 0.1$: (*a*) $t = 50$; (*b*) $t = 80$; (*c*) $t = 400$; and (*d*) $t = 650$.

As is known, the case of flow over a single negative obstacle, or hole, is more complicated, as the shock waves are generated at the obstacle location; see Grimshaw & Smyth (1986) and Grimshaw *et al.* (2007, 2009). Hence we expect that the case when either or both of the obstacles are holes could lead to different and more complicated scenarios, which will be the subject of a future study. Further, the present study is restricted to non-dispersive waves. Extensions to include even just weak dispersion using the forced KdV equation, or the fully nonlinear Su–Gardner equations, as done by El *et al.* (2009) for a single obstacle, will certainly lead to rather different behaviour. In that case, the shocks are replaced by undular bores and the shock interactions described here are replaced by the interactions of these nonlinear wave trains. For instance, some of the numerical simulations reported by Grimshaw *et al.* (2009) using just the forced KdV equation indicate that the interaction of these nonlinear wave trains can produce very complicated behaviour. This is also a topic needing much further study.

Acknowledgements

This work was supported by the Thailand Research Fund (TRF) and the Kasetsart University Research and Development Institute (KURDI) under grant no. RSA5680038 to the second author.

Appendix A

The weakly nonlinear model (1.5) for small-amplitude topographic forcing in the transcritical regime can be derived as follows. First, we introduce the Riemann

variables

$$R = U + 2C, \quad L = U - 2C, \quad C = \sqrt{H}, \tag{A 1a,b}$$

so that (1.1) and (1.2) become

$$R_t + (U + C)R_x + f_x = 0, \quad L_t + (U - C)L_x + f_x = 0. \tag{A 2a,b}$$

Then we assume that $f \sim \alpha^2$ where $\alpha \ll 1$, and that $\zeta \sim \alpha$, $\zeta_t \sim \alpha^2$, $u = U - Fr \sim \alpha$ and $\Delta = Fr - 1 \sim \alpha$. Next, noting that $U + C = Fr + 1 + O(\alpha)$, we can find an approximation to the right-going Riemann invariant in the vicinity of the topography,

$$R = Fr + 2 - \frac{f}{2} + O(\alpha^3) \quad \text{so that} \quad u + \zeta = \frac{\zeta^2}{4} + \frac{f}{2} + O(\alpha^3). \tag{A 3a,b}$$

Here a transient propagating rapidly with a speed $Fr + 1 + O(\alpha)$ to the right is ignored. Then we find that, for the left-going Riemann invariant,

$$L = 2U - (Fr + 2) + \frac{f}{2} + O(\alpha^3) = Fr - 2 - 2\zeta + \frac{\zeta^2}{2} + \frac{3f}{2} + O(\alpha^3), \tag{A 4a}$$

$$U - C = \frac{3U}{2} - \frac{Fr + 2}{2} + \frac{f}{4} + O(\alpha^3) = \Delta - \frac{3\zeta}{2} + O(\alpha^2). \tag{A 4b}$$

Thus, finally, the equation for L in (A 2) reduces to (1.5), with an error of $O(\alpha^3)$. Similarly, the mass shock condition in (1.4) reduces to (1.7) with an error of $O(\alpha^3)$, while the momentum shock condition has all terms of $O(\alpha^3)$.

REFERENCES

AKYLAS, T. R. 1984 On the excitation of long nonlinear water waves by moving pressure distribution. *J. Fluid Mech.* **141**, 455–466.

AUDUSSE, E., BOUCHUT, F., BRISTEAU, M.-O., KLEIN, R. & PERTHAME, B. 2004 A fast and stable well-balanced scheme with hydrostatic reconstruction for shallow water flows. *SIAM J. Sci. Comput.* **25**, 2050–2065.

BAINES, P. 1995 *Topographic Effects in Stratified Flows*. Cambridge University Press.

BINDER, B., DIAS, F. & VANDEN-BROECK, J.-M. 2006 Steady free-surface flow past an uneven channel bottom. *Theor. Comput. Fluid Dyn.* **20**, 125–144.

COLE, S. L. 1985 Transient waves produced by flow past a bump. *Wave Motion* **7**, 579–587.

DIAS, F. & VANDEN-BROECK, J. M. 2004 Trapped waves between submerged obstacles. *J. Fluid Mech.* **509**, 93–102.

EE, B. K., GRIMSHAW, R. H. J., CHOW, K. W. & ZHANG, D.-H. 2011 Steady transcritical flow over a hole: parametric map of solutions of the forced extended Korteweg–de Vries equation. *Phys. Fluids* **23**, 04662.

EE, B. K., GRIMSHAW, R. H. J., ZHANG, D.-H. & CHOW, K. W. 2010 Steady transcritical flow over an obstacle: parametric map of solutions of the forced Korteweg–de Vries equation. *Phys. Fluids* **22**, 056602.

EL, G., GRIMSHAW, R. & SMYTH, N. 2006 Unsteady undular bores in fully nonlinear shallow-water theory. *Phys. Fluids* **18**, 027214.

EL, G., GRIMSHAW, R. & SMYTH, N. 2008 Asymptotic description of solitary wave trains in fully nonlinear shallow-water theory. *Physica* D **237**, 2423–2435.

EL, G., GRIMSHAW, R. & SMYTH, N. 2009 Transcritical shallow-water flow past topography: finite-amplitude theory. *J. Fluid Mech.* **640**, 187–214.

GRIMSHAW, R. 2010 Transcritical flow past an obstacle. *ANZIAM J.* **52**, 1–25.

GRIMSHAW, R. & SMYTH, N. 1986 Resonant flow of a stratified fluid over topography. *J. Fluid Mech.* **169**, 429–464.

GRIMSHAW, R., ZHANG, D. & CHOW, K. 2007 Generation of solitary waves by transcritical flow over a step. *J. Fluid Mech.* **587**, 235–354.

GRIMSHAW, R., ZHANG, D.-H. & CHOW, K. W. 2009 Transcritical flow over a hole. *Stud. Appl. Math.* **122**, 235–248.

LEE, S.-J., YATES, G. & WU, T.-Y. 1989 Experiments and analyses of upstream-advancing solitary waves generated by moving disturbances. *J. Fluid Mech.* **199**, 569–593.

PRATT, L. J. 1984 On nonlinear flow with multiple obstructions. *J. Atmos. Sci.* **41**, 1214–1225.

SIVIGLIA, A. & TORO, E. 2009 WAF method and splitting procedure for simulating hydro- and thermal-peaking waves in open-channel flows. *J. Hydraul. Engng* **135**, 651–662.

TORO, E. 1992 Riemann problems and the WAF method for solving two-dimensional shallow water equations. *Phil. Trans. R. Soc. Lond.* A **338**, 43–68.

TORO, E., SPRUCE, M. & SPEARES, W. 1994 Restoration of the contact surface in the HLL-Riemann solver. *Shock Waves* **4**, 25–34.